Layer-by-Layer Assembly of Perovskite Nanosheets and Its Applications to Electronic Materials

ペロブスカイトナノシートのレイヤーバイレイヤー集積とその電子材料への応用

December 2017

Muhammad Shuaib KHAN
ハーン　ムハンマド シュエイブ

Layer-by-Layer Assembly of Perovskite Nanosheets and Its Applications to Electronic Materials

ペロブスカイトナノシートのレイヤーバイレイヤー集積とその電子材料への応用

December 2017

Waseda Univeristy
Graduate School of Advance Science and Engineering
Department of Nanoscience and Nanoengineering
Research on Nano-Functional Molecules Chemistry

Muhammad Shuaib KHAN
ハーン　ムハンマド シュエイブ

Abstract

Complex perovskite oxides offer tremendous potential for controlling their rich variety of electronic properties including high-T_C superconductivity, high-k ferroelectricity and magnetism. Atomic-scale control of these intriguing properties in ultrathin perovskites is an important challenge for exploring new functionalities and devices at atomic dimensions. Recently, tremendous studies have suggested that perovskite superlattices provide a powerful route to manipulate the electronic states, offering new possibilities for new electronic materials and devices. So far, such superlattices have been made with state-of-the-art thin-film technologies involving molecular-beam epitaxy and pulsed laser deposition. However, the design of such artificial systems relies on good lattice matching between the layers; hence, particular attention must be devoted to the chemical stability of the interface to prevent intermixing. Because of these constraints of current thin-film technologies, engineered functionalities or nanodevices are still limited by the choice of materials.

Two-dimensional (2D) oxide nanosheets are interesting material, which allow the design of ultrathin multilayer/superlattice films at room temperature. The exfoliated oxide nanosheets from their parent-layered materials possess molecular thickness (~ 1nm) and lateral dimension in range of few hundred of nanometers to several tens of micrometers. Due to molecular thickness, oxide nanosheets are considered as thinnest self-standing structures and acquire the characteristics of their parent layered compounds. In 2D materials, an emerging research area is a layer-by-layer (LbL) assembly method that enables to combine 2D materials into various heterostructure. New materials with sophisticated functionalities may be designed through controlled LbL assembly of 2D nanosheets. Such protocols relying on 2D building blocks provide a versatile platform for exploring new artificial materials with kinetically controlled, hierarchical architectures and tailored properties.

In this thesis, I present a new strategy in which 2D perovskite nanosheets are used as building blocks for the unit-cell-level engineering of perovskite heterostructures for tailored electronic materials. A particular focus is put on Dion

Jacobson (DJ)-type homologous series of layered perovskites ($KCa_2Na_{m-3}Nb_mO_{3m+1}$; m = 3–6), which has been investigated as an important target for ion-exchange reactions and exfoliated nanosheets. In this homologous series, the perovskites slabs are virtually infinite in the 2D planes and have a variable thickness along the slab normal; the integer m corresponds to the number of NbO_6 octahedron units (perovskite layers). The exfoliated nanosheets from homologous perovskites ($Ca_2Na_{m-3}Nb_mO_{3m+1}^-$; m = 3–6) would provide an ideal base for atomic-scale control engineering dielectric/ferroelectric responses. However, such a possibility has not been explored. Here, I demonstrated LbL engineering of dielectric/ferroelectric responses using 2D homologous perovskite nanosheets ($Ca_2Na_{m-3}Nb_mO_{3m+1}^-$; m = 3–6).

LbL assembly of $Ca_2Nb_3O_{10}^-$ nanosheets is utilized for tailoring dielectric responses and breakdown voltages in miniaturized capacitors. I used $Ca_2Nb_3O_{10}^-$ nanosheet as a model system for high-k dielectrics as this material possesses a highly crystal nature with large lateral size (> 10 μm) and highly insulting characteristic. Multilayer stacked nanosheets films showed a stable dielectric response (ε_r = ~210) up to 10 GHz. Furthermore, the multilayer films exhibited stable capacitance density of > 20 $\mu F/cm^2$ at high temperatures up to 250 ^oC, suitable for high-performance microwave devices.

I extended the LbL assembly technique to hetero-assembly of all-nanosheet capacitors. The ultrathin dielectric layers of $Ca_2Nb_3O_{10}^-$ were assembled via Langmuir-Blodgett (LB) technique. The dielectric layers were sandwiched by the ultrathin electrode layers of $Ru_{0.95}O_2^{0.2-}$ nanosheets to form the metal-insulator-metal structure. Nanosheets-based capacitors demonstrated high-k dielectric (>155) and insulating properties (< 1 x 10^{-5} A/cm^2) at high temperatures up to 250 ^oC. Newly developed high-k nanosheets ($Ca_2NaNb_4O_{13}^-$; ε_r = 300) were also exploited for the development of LbL assembled multilayer nanosheet capacitors. In particular, mm-size multilayer nanosheet capacitors with a total thickness of ~20 nm were assembled on glass substrates with high capacitance of 52 $\mu F/cm^2$ and low leakage current down to 10^{-6} A/cm^2, which are stable at high temperatures up to 250 ^oC. Such a high-k response with thermal stability is promising for the application in high temperature nanoelectronics.

As a new direction of the LbL engineering, I utilize the superlattice engineering of perovskite nanosheets ($Ca_2Na_{m-3}Nb_mO_{3m+1}^-$; m = 3–6) for designing artificial ferroelectrics. Hetero-assembly of $Ca_2Na_{m-3}Nb_mO_{3m+1}$ nanosheets produced a new form of superlattices with an atomically precise interface and polar discontinuity, which are inaccessible in state-of-the-art thin-film technologies. LbL engineering of $Ca_2Na_{m-3}Nb_mO_{3m+1}^-$ nanosheets enabled tailoring dielectric/ferroelectric responses to realize atomically thin ferroelectrics. These results provide a strategy for achieving new 2D ferroelectrics for use in ultra-scaled electronics.

Contents

Chapter 1

General Introduction

1.1. Perovskite oxides

The oxides with general formula of ABO_3 (*A*: alkali, alkaline earth or rare earth elements, *B*: transition metal or group IV elements) are known as perovskite oxides. The perovskites structure is one of the most studied compounds by solid-state scientists. In 1839, Gustav Rose discovered the first perovskite, $CaTiO_3$.[1] 'Perovskite' was initially reserved for $CaTiO_3$ and later applied to compounds with similar crystal structure and stoichiometry. Pioneering structural work on perovskites was conducted by Goldschmidt, who schemed many principles about the structures that remained applicable even today.[2] The perovskite oxides are focus of intense research by solid-state chemists, physicist and materials scientists because they realize fascinating physical properties[3] such as high-*k* dielectric, ferroelectricity, piezoelectricity, colossal magnetoresistance and superconductivity. The origins of these properties are often complex; the property of interest can be related to structure and composition of perovskite materials. Since perovskite structures can afford a large number of cations and anions; hence it is possible to modulate their structures and properties.

Layered perovskite oxides have fascinated scientists because of myriad range of physical properties such as high-*k* dielectricity, ferroelectricity, high-T_C superconductivity and colossal magnetoresistance. Important examples include Dion-Jacobson (DJ) phase, Aurivillius phase (AU) and Ruddlesden-Popper (RP) phase with general formulas as $A'[A_{m-1}B_mO_{3m+1}]$, $[Bi_2O_2][A_{m-1}B_mO_{3m+1}]$ and $A''A_{m-1}B_mO_{3m+1}$ respectively, where, *A*' represents univalent alkali cations, *A*" denotes alkali or alkaline earth metals, *A* demonstrates mono-, di- or trivalent cations, *B* indicates tetra-, penta-, or hexavalent ions and *m* is number of perovskite blocks (Figure 1.1). Layer perovskites are comprised of 2D blocks of ABO_3 that are separated by interlayer ions. The structure and physical properties of layered perovskites are controlled via appropriate selection of *A* and *B* cations and number perovskite units (*m*).[4]

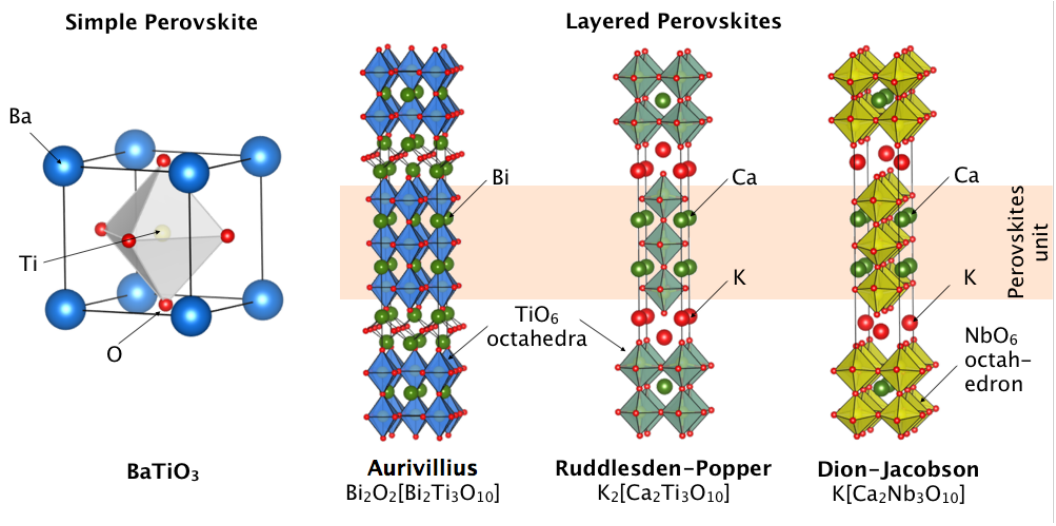

Figure. 1.1. Structure of simple perovskite and layered perovskite.

The family of layered perovskites has been extensively investigated for their applications as high-*k* dielectric and ferroelectric materials. Previous studies have mainly focused on RP and AU phases. For the scientific viewpoint, doping polarizable ions and modulating structural distortions have observed to be interesting strategies for designing new dielectric and ferroelectric materials. Moreover, number of perovskite units (*m*) also has significant effect to control polarizability. For example, homologous series of RP phase, $Sr_{m+1}Ti_mO_{3m+1}$ exhibited *m* dependent high-*k* dielectric response and considered as important high-*k* dielectrics.[5]AU family includes number of ferroelectrics ($SrBi_2Ta_2O_9$ and $Bi_4Ti_3O_{12}$) in which *B*-site is occupied by so-called ferroelectricity active d^0 cations such as Ti^{4+} and Nb^{5+} and Ta^{5+}. Such materials have been studied for their fatigue-free ferroelectric properties in nonvolatile memory applications.

In contrast to RP and AU phases, dielectric and ferroelectric properties of DJ phase have not been studied extensively. However, DJ compounds have exhibited excellent chemical affinity towards ion-exchange processes leading to formation of exfoliated nanosheets. In addition, the presence of d^0 cations (Ti^{4+}, Nb^{5+}, Ta^{5+}) at *B*-sites in DJ compounds is responsible for asymmetric second-order Jahn-Teller distortion and predicted to demonstrate high-*k* dielectric/ferroelectric properties. However, there are only few studies exploring the dielectric/ferroelectric properties in DJ compounds. Therefore, an increasing motivation is to systematically explore the dielectric and ferroelectric properties in

DJ compounds for their far-reaching applications. However, the presence of high-*k* properties in DJ phases can be found in literature. For example, $HPb_2Nb_3O_{10}$ has exhibited high-*k* dielectric response ($\varepsilon_r \sim 150$).[6] In another report, homologous series of $KCa_2Na_{m-3}Nb_mO_{3m+1}$ (m = 3-6) and $KLaNb_2O_7$ (m = 2) demonstrated m dependent high-*k* dielectric response, a similar characteristic to RP and AU phases. The observed values of dielectric constant can be summarized as ε_r = 30, 300, 390, 490, 500 for m = 2-6, respectively. These results confirmed a superior dielectric behavior of DJ compounds such as m = 6 exhibited highest dielectric constant of 500, far superior than m = 6 compounds for RP and AU phases.[7] The interesting characteristics of DJ compounds such as high-*k* properties and exfoliation reaction possess considerable importance, as exfoliated perovskite nanosheets are potential candidate for the rational design of high-*k* dielectric/ferroelectric materials.

1.2. Dielectric/ferroelectric properties at nanoscale

The study of dielectric and ferroelectric properties at nanoscale is quite important because of several reasons. Firstly, electronic industry demands for ultra-thin devices with enhanced functionality. Secondly, the observation of novel properties during the fabrication of thin films of complex oxides via various fabrication techniques (top-down or bottom-up). Finally, the presence of notably different dielectric and ferroelectric behavior at nanoscale as compared to bulk materials.

Perovskite oxides with high-*k* dielectric and ferroelectric properties have been exploited from various applications. Among these, $BaTiO_3$, $Ba_{1-x}Sr_xTiO_3$, and $Pb(Zr_{1-x}Ti_x)O_3$ are important perovskite materials that demonstrate excellent properties such as high dielectric constant, ferroelectricity and piezoelectricity.[8-10] However, when the size of these perovskite materials is reduced down below ~100 nm, they suffer from significant lost in dielectric response (Figure 1.2) and transition to paraelectric phase at room temperature.[11] For example, as the size of nanoparticles of $BaTiO_3$ and $PbTiO_3$ is decrease, a reduction in Curie temperature (T_C) results in room temperature stabilization of the paraelectric phase. A similar phenomenon is observed in thin-film forms of simple and layered perovskites.

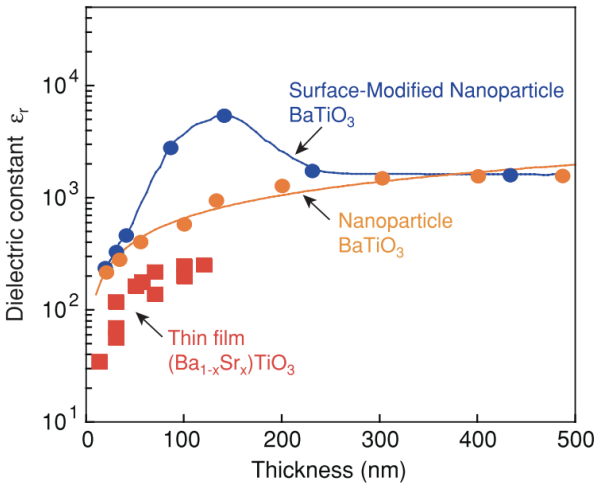

Figure 1.2. Size-dependent properties of $BaTiO_3$ nanostructures. Adopted with permission.[11] Copyright 2011, John Wiley and Sons.

The combination of experimental and theoretical studies revealed that the size effects in ferroelectric thin films become important when at least one critical dimension is in the range of 10 nm. Although size effect controls the limit of thermodynamics stability of ferroelectric phase, the changes in properties typically begin over much larger length scales. There can be several origins for size effects including, finite electrode screening, interface mixing, external strain, impurities and point defects and crystallographic defects.[12-15]

The origin of degradation of ferroelectric response is not clear, however, the possible presence of low-*k* dead layer at the interface is reason for decreased response. The reason for presence of dead layer is creation of depolarization field, which occurs when spontaneous polarization in thin ferroelectrics is terminated by the introduction of surface or interface. For example, in an ultrathin single crystal, surface charges result in the generation of electric field that deteriorates the normal component of polarization. This electric field will oppose the polarization and destabilize the ferroelectric phase and works as dead layer.[16] There present four factors such as electrode screening, electrical conduction, polarization gradients and domain formation, which sustain the polar characteristics of lattice in response to depolarization field.[17,18] However, electrode screening has major effect on the stability of ferroelectric phase. In case of ferroelectric capacitor, due to

polarization, surface charge is developed that should be neutralized with the counter charge by electrode. In actual practice, charge occupies a defined physical length and is responsible for incomplete screening of ferroelectric polarization and depolarization field. However, this electrode screening effect can be modulated by appropriate selection of electrode material and ferroelectric films. Moreover, there exist extrinsic effects, which deteriorate the ferroelectric properties of the films such as thermal strain and inter-diffusion.

The intrinsic properties of perovskite thin films can be exploited through fabrication of multilayer and/or superlattice films. A key issue for this is to realize high-quality multilayer and/or superlattice films with clean interfaces. This idea also provides an additional benefit of reduced sizes in integrated circuits and hence responsible for advancement of electronic devices.

1.3. 2D Perovskite Nanosheets

A common feature of the layered perovskites is their ion-exchange property involving interlayer ions. Due to large possibilities of ion-exchange reactivity and intercalation chemistry at interlayer space, it is possible to fabricate various hybrid materials. These features are also responsible for large swelling behavior and complete delamination of layered perovskites into elemental layers (nanosheets). The delamination of layered perovskites has been reported for DJ phase into nanosheets such as $LaNb_2O_7^-$, $La_2Ti_2NbO_{10}^-$, $Sr_2Nb_3O_{10}^-$, $Ca_2Nb_{m-3}Nb_mO_{3m+1}^-$ (m = 3-6), $BiNb_2O_7^-$, $Ca_2Ta_3O_{10-x}N_x^-$, and $CaLaNb_2TiO_{10}^-$,[19-22] and for AU phase (i.e. $Bi_2Ti_3O_{10}^{2-}$, $Bi_xW_2O_7^{2-}$, and $Sr_{0.75}Bi_{0.16}Ta_2O_7^{2-}$)[23,24] and RP phase (e.g. $Eu_{0.56}Ta_2O_7^-$, $SrLaTi_2TaO_{10}^{2-}$, and $Ca_2Ta_2TiO_{10}^{2-}$) (Table 1.1).[25-28]

Table 1.1. Exfoliated perovskite nanosheets from their parent-layered perovskites with different physical properties.

Phase type	Nanosheet composition	Parent layered perovskite composition	Property
DJ	$LaNb_2O_7^-$	$KLaNb_2O_7$	Dielectric
	$La_2Ti_2NbO_{10}^-$	$KLa_2Ti_2NbO_{10}$	Dielectric
	$Sr_2Nb_3O_{10}^-$	$KSr_2Nb_3O_{10}$	Dielectric
	$Ca_2Nb_{m-3}Nb_mO_{3m+1}^-$ (m = 3 - 6)	$KCa_2Nb_{m-3}Nb_mO_{3m+1}$ (m = 3 - 6)	Dielectric/ Ferroelectric
	$BiNb_2O_7^-$	$A'[BiNb_2O_7]$ A' = Rb, Cs	Ferroelectric
	$CaLaNb_2TiO_{10}^-$	$A'[CaLaNb_2TiO_{10}]$ A' = K, Rb, Cs	Ferroelectric
AU	$Bi_2Ti_3O_{10}^{2-}$	$Bi_4Ti_3O_{12}$	Ferroelectric
	$Bi_xW_2O_7^{2-}$	$Bi_2W_2O_9$	Ferroelectric
	$Sr_{0.75}Bi_{0.16}Ta_2O_7^{2-}$	$SrBi_2Ta_2O_7$	Ferroelectric
RP	$Eu_{0.56}Ta_2O_7^-$	$LiEu_{0.56}Ta_2O_7$	-
	$SrLaTi_2TaO_{10}^{2-}$	$K_2SrLaTi_2TaO_{10}$	-
	$Ca_2Ta_2TiO_{10}^{2-}$	$K_2Ca_2Ta_2TiO_{10}$	-

Soft-chemical exfoliation procedure is considered as most facile method for the synthesis of perovskite nanosheets.[29] In layered perovskite-type oxometallates, exfoliation does not take place spontaneously due to their higher layer charge density. The general procedure consists of two steps and is demonstrated in Figure 1.3. First step involves the replacement of interlayer cations with protons to enlarge the interlayer distances. In the second step, the energetic barrier between neighboring layers is overcome by incorporation of exfoliating reagent into the interlayer space. This leads to further expansion due to introduction of solvent molecules into the interlayer spacing. With the appropriate selection of exfoliating agents such as tetrabutylammonium hydroxide (TBAOH), it is possible to separate out the layered material into single nanosheets, which are stable in the form of colloidal suspension. Thus, exfoliated perovskite nanosheets bare overall negative charge due to removal of interlayer cations. These perovskite nanosheets are 2D single crystals with well-defined compositions. 2D perovskite nanosheets are thinnest self-standing systems with lateral dimensions in sub-microns to few microns. The molecular thickness (1.4 – 3 nm) of 2D perovskite nanosheets

depends on the parent-layered materials from which they are exfoliated. With solution-based exfoliation method, it is possible to synthesize dozens of different perovskite nanosheets.

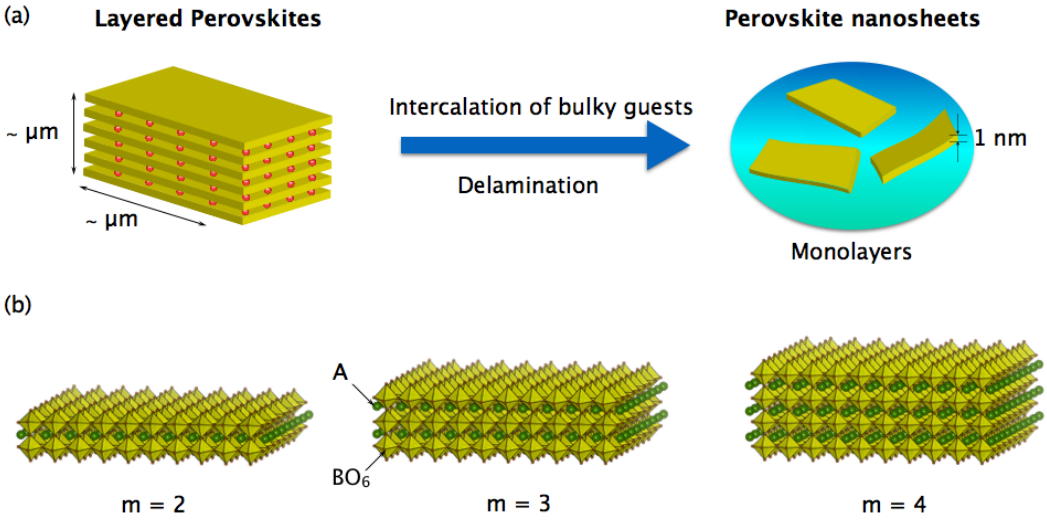

Figure 1.3. (a) A general procedure for delaminating layered perovskites into their single layers. **(b)** Illustrated structures of m = 2, 3 and 4 perovskite nanosheets $A_{m-1}B_mO_{3m+1}^-$ (A = La^{3+}, Eu^{3+}, Ca^{2+}, Sr^{2+}, Bi^3 and more; B = Ti^{4+}, Nb^{5+}, and Ta^{5+}).[19-28]

Perovskite nanosheets are exclusively comprised of surface atoms in the form of arranged perovskite building blocks such as NbO_6 in case of $Ca_2Nb_3O_{10}^-$. As a result, perovskite nanosheets are highly polarizable and are ideal material for high-k dielectrics and equally ferroelectrics with ultrathin thickness.

1.4. Layer-by-Layer Assembly of 2D Oxide Nanosheets

LbL assembly of perovskite nanosheets is an important methodology for the design of dielectric and ferroelectric films with precise thickness and composition. To date, the state-of-the-art film technologies such as molecular-beam epitaxy and pulse laser deposition have been widely adopted to achieve perovskite thin films. These techniques usually consist of complicated deposition procedures followed by high-temperature annealing (> 600 ^oC), which result in degradation of dielectric properties due to defects and thermal strains.[30] So, there is increasing motivation

to look for alternative paradigms that can address engineering of interface at atomic scale to magnify the full potential of perovskite superlattices. The best condition to grow thin film is the ambient environment. Through LbL assembly, it is possible to assemble 2D perovskite nanosheets for the construction of thin films at room temperature and hence the integration problems can be avoided that exist in current epitaxially grown thin films. Perovskite nanosheets with nanoscale thickness and infinite planar length in lateral dimensions are regarded as thinnest functional materials.[31] The polyelectrolyte nature of perovskite nanosheets enables them to be used as building blocks to fabricate highly organized multilayer and superlattice films (Figure 1.4) via sequential adsorption and LB technique. Sequential adsorption is an effective methodology for the fabrication of novel heterostructures with controlled thickness and composition on solid or flexible surfaces. Iler and Kirkland carried out the pioneer work on LbL assembly in 1964, which involved the assembly of inorganic films comprised of oppositely charged species.[32,33] However, the boost in LbL assembly processes started after Decher's report[34] on assembly of polyelectrolytes (PEs) in alternate fashion to precisely control the film architectures. The electrostatic LbL method is also known as "molecular beaker epitaxy" for fabricating novel nanostructures. For electrostatic assembly of multilayer films of perovskite nanosheets, usually poly(diallyldimethylammonium chloride) (PDDA) and poly(ethylenimine) (PEI) are employed as counter positively charged polycations. This method has been extensively used by various research groups to fabricate thin films of perovskites nanosheets.[35]

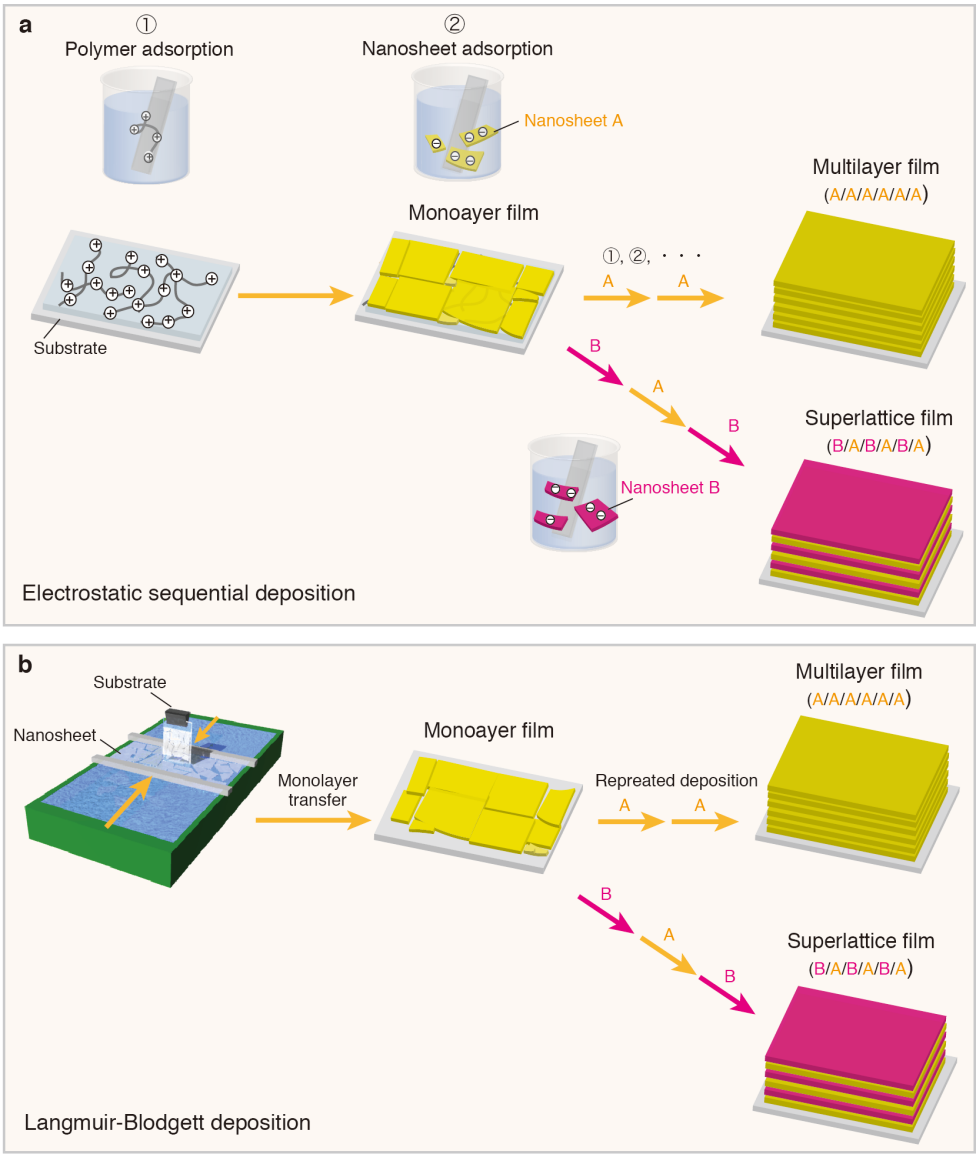

Figure 1.4. Schematic illustration for LbL assembly of 2D oxide nanosheets. **(a)** electrostatic sequential deposition and **(b)** LB process. Adopted with permission.[35] Copyright 2015, Nature publishing group.

LB is also observed to be an effective method for the LbL assembly of perovskite nanosheets with precise thickness control. During LB film fabrication, monolayer film of material can be formed by controlling the compression with the help of moveable barrier. Then with the dipping or lifting of solid substrate in/out of the solution contained in LB trough, it is possible to transfer well-packed monolayer film onto the substrate. Usually, LB method is effective for organic

materials; however, this has proven equally effective for inorganic materials. In a pioneer work, it has been exhibited that perovskite nanosheets in the presence of moderate amphiphilic compound such as tetrabutyl ammonium ions can float at air/water interface. While controlling the packing density of floating nanosheets at air/water interface with the help of moveable barrier, it is possible to transfer perovskite nanosheets from liquid phase on to solid surface by vertical lifting process using ordinary LB procedure.

It has been reported that multilayer and superlattice films can be fabricated via LB method on atomically flat $SrRuO_3$ substrate. These films exhibited highly packed deposition with atomically uniform and dense characteristics (Figure 1.5). The resulting multilayer and superlattice films realized high-*k* properties and novel ferroelectricity, hence suitable for various applications.[36]

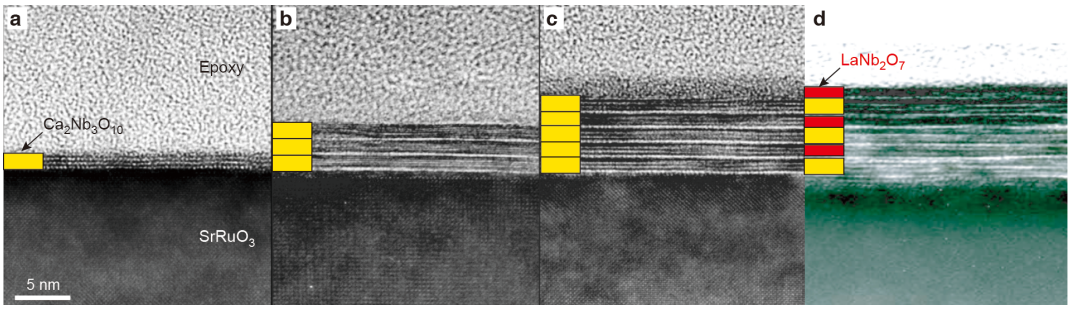

Figure 1.5. TEM images for multilayer and superlattice films assembled from perovskite nanosheets ($Ca_2Nb_3O_{10}^-$, $LaNb_2O_7^-$). **(a)** $(Ca_2Nb_3O_{10}^-)_1$, **(b)** $(Ca_2Nb_3O_{10}^-)_3$, **(c)** $(Ca_2Nb_3O_{10}^-)_5$, **(d)** $(LaNb_2O_7^-/Ca_2Nb_3O_{10}^-)_3$. These nanoarchitectures were fabricated by a LbL assembly using LB process. Adopted with permission.[35] Copyright 2015, Nature publishing group.

An important strategy is to use 2D perovskite nanosheets as a core component for electronic devices. Due to molecular thickness of perovskite nanosheets, it possesses advantage over conventional down-sizing approaches. Therefore, LbL assembly of perovskite nanosheets exhibited considerable attention for solution-processed electronics, especially for dielectric capacitors. To observe such possibilities, Osada *et al*. employed LB method as an effective technique for organizing perovskite $Ca_2Nb_3O_{10}^-$ nanosheets in LbL fashion. The resulting

multilayers with thickness between 5-20 nm were fabricated on atomically flat $SrRuO_3$ and Pt substrates. The multilayer films of perovskite nanosheets exhibited high dielectric constant of ~210 and low leakage current density of < 10^{-7} A/cm^2.[37] For tailoring high-*k* dielectric properties, doping and/or lattice engineering approaches have been utilized for $Ca_2Nb_3O_{10}^-$.[37] For example, *A*-site substitution with Sr^{2+} ions increased the ε_r value, whereas *B*-site substitution with Ta^{5+} ions improved the insulating properties with enlarged bandgap and breakdown voltage. Recently, Li *et al*. reported atomic scale engineering in multilayer films of homologous series of perovskite ($Ca_2Na_{m-3}Nb_mO_{3m+1}^-$; m = 3-6) nanosheets to demonstrate excellent high-*k* properties and low leakage current density (*J*) with ultrathin thickness (Figure 1.6). The multilayer film of m = 6 perovskite member exhibited highest dielectric constant of ~470. The observed value is highest among all known dielectric perovskites in ultrathin region (< 10 nm). Such a multilayer capacitor of $Ca_2Na_3Nb_6O_{19}^-$ nanosheets realized capacitance density of ~203 μF/cm^2, a value 3 times higher than current ceramic condensers, establishing a new direction for energy storage devices.[38]

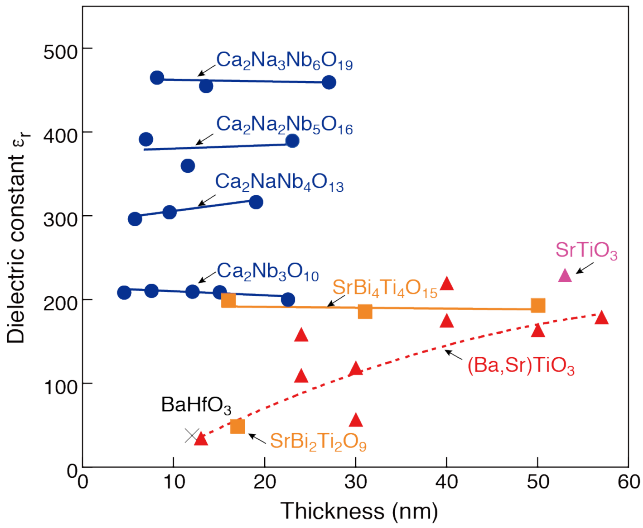

Figure 1.6. Dielectric response (ε_r) for homologous series of perovskites ($Ca_2Na_{m-3}Nb_mO_{3m+1}^-$; m = 3-6) nanosheets and various perovskite thin films. Adopted with permission.[38] Copyright 2017, American Chemical Society.

High-*k* properties and molecular thickness are peculiar features of perovskite nanosheets to be used as building blocks for designing new electronic devices. Li *et al*. fabricated artificial superlattice films comprised of perovskite $LaNb_2O_7^-$ and $Ca_2Nb_3O_{10}^-$ nanosheets via LB method. Such superlattice films exhibited enhanced dielectric response and improved leakage as compared to the multilayer films of its constituent nanosheets $[(LaNb_2O_7^-)_{10}$ and $(Ca_2Nb_3O_{10}^-)_{10}]$. In spite of paraelectric nature of constituent nanosheets, the superlattice film, $(LaNb_2O_7^-/Ca_2Nb_3O_{10}^-)_5$, demonstrated ferroelectric hysteresis (Figure 1.7). The ferroelectric property in superlattice films can be associated to the interface coupling, which is not possible in bulk form.[36]

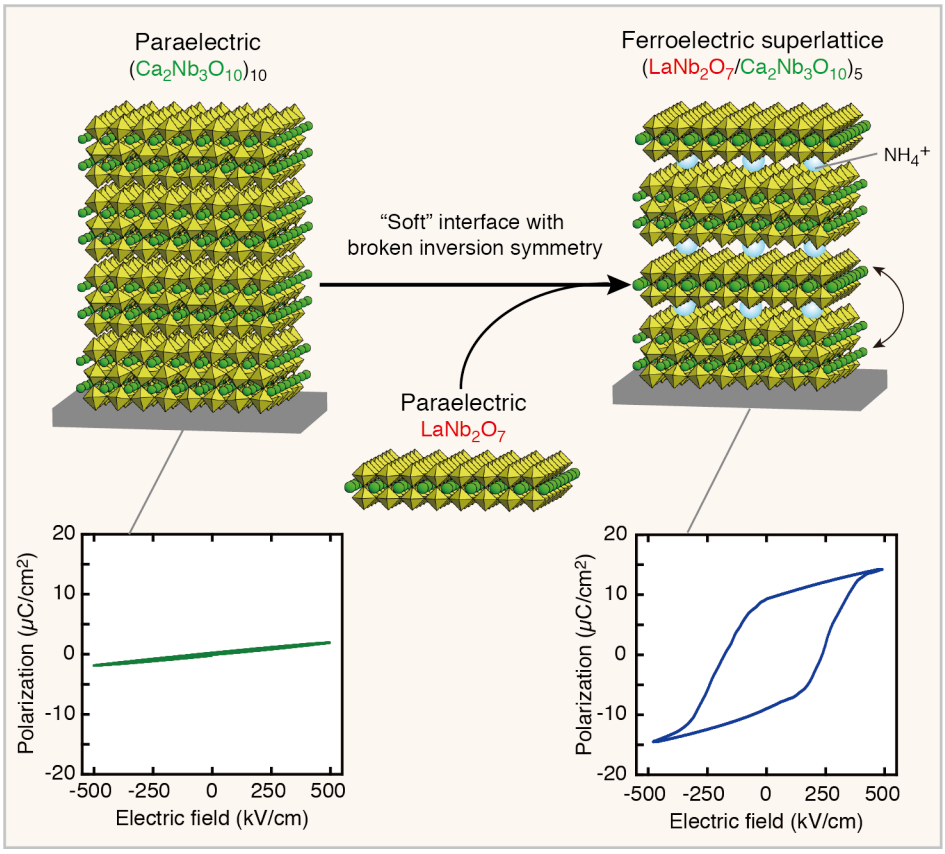

Figure 1.7. Artificial superlattice assembled from perovskite nanosheets. In contrast to the paraelectric nature of $Ca_2Nb_3O_{10}^-$, the $(LaNb_2O_7^-/Ca_2Nb_3O_{10}^-)$ superlattice possesses a new form of interface coupling, which gives rise to ferroelectricity. Adopted with permission.[35] Copyright 2015, Nature publishing group.

Through solution-based assembly of superlattices it is possible to design novel nanostructures with multiferroic characteristics. For this purpose, perovskite

$Ca_2Nb_3O_{10}^-$ nanosheets have been combined with ferromagnetic $Ti_{0.8}Co_{0.2}O_2^-$ nanosheets in the form superlattice assembled via LbL method. Such superlattice films demonstrate interlayer coupling between ferromagnetic and dielectric nanosheets leading to multiferroic behavior. These superlattices demonstrated magneto-capacitance and magneto-electric response.[39]

It can be summarized from previous work on perovskite multilayer and superlattice films that solution-based LbL assembly is an effective technique for the realization of novel heterostructures. However, the dielectric/ferroelectric properties of perovskite nanosheets have yet to be fully explored, and such exploration is required to utilize perovskite nanosheets in potential far-reaching applications. Considering their rich variety in composition, structure and electronic properties of layered perovskites, I foresee developing more complex perovskite nanoarchitectures exhibiting a wide range of new and sophisticated functions.

1.5. Purpose of Thesis

In this thesis, I focus on LbL assembly of DJ-type homologous series of perovskites nanosheets ($Ca_2Na_{m-3}Nb_mO_{3m+1}^-$; m = 3-6). The study focuses on following subjects.

1. Tuning of dielectric properties in multilayered stacked nanosheets films.
2. Hetero-assembly of perovskite nanosheets for multilayer capacitors.
3. High-temperature applications of nanosheets-based capacitors.
4. Engineering of dielectric/ferroelectric responses in perovskite superlattices.

Homologous series of perovskite nanosheets ($Ca_2Na_{m-3}Nb_mO_{3m+1}^-$; m = 3-6) are important class of materials. The multilayer films of these perovskite nanosheets have realized highest dielectric constant in ultrathin thickness (< 10 nm) (Figure 1.6). The increase in dielectric constant in homologous members can be associated to increase connectivity of NbO_6 octahedra along the *c*-axis that enables the displacement of Nb^{5+} in O^{2-}-Nb^{5+}-O^{2-} bonding leading to increase permittivity. These perovskite nanosheets also exhibited highly insulating properties below ~10^{-7} A/cm^2 at +1V which is dependent on m. These characteristics of homologous series of perovskite nanosheets ($Ca_2Na_{m-3}Nb_mO_{3m+1}^-$

; m = 3-6) make them interesting materials for LbL assembly to engineer dielectric/ferroelectric properties at molecular level in novel nanostructure films. However, the dielectric/ferroelectric properties of these perovskite nanosheets have yet to be fully explored, and such exploration is required to utilize perovskite nanosheets in potential far-reaching applications.

This thesis is consisted of 6 chapters. Chapter 1 discloses the background and purpose of this thesis. Chapter 2 covers the LbL assembly of $Ca_2Nb_3O_{10}^-$ nanosheets for tailored microwave dielectrics. Chapter 3 describes the LbL assembly of $Ca_2NaNb_4O_{13}^-$ nanosheets for fabrication of multilayer nanosheets capacitors. Chapter 4 extends the study of nanosheets-based capacitors ($Ca_2Nb_3O_{10}^-$, $Ca_2NaNb_4O_{13}^-$) for high-temperature applications. Chapter 5 explains the superlattice assembly of homologous perovskite nanosheets ($Ca_2Na_{m-3}Nb_mO_{3m+1}^-$; m = 3-6) for realizing artificial ferroelectrics. Chapter 6 outlines the summary and prospective of the thesis.

In Chapter 2, I fabricated multilayer films of 2D perovskite nanosheets for microwave dielectrics. I used $Ca_2Nb_3O_{10}^-$ perovskite nanosheet as a model system of this study. $Ca_2Nb_3O_{10}$ nanosheet composes of three NbO_6 octahedra, a key building block of perovskite dielectrics that establish the nanosheets as perfect material with high-k characteristic at molecular thickness. This nanosheet also possesses a highly crystal nature with large lateral size (> 10 μm) and highly insulting characteristic. LbL assembly of $Ca_2Nb_3O_{10}^-$ nanosheets is a powerful tool to engineer dielectric responses and breakdown voltages in ultrathin nanosheets capacitors. In previous studies, multilayer films of $Ca_2Nb_3O_{10}^-$ nanosheets have exhibited stable dielectric responses in MHz frequency region and large breakdown voltage of 3.5 MV/cm. In this study, I focused on the LbL assembly of multilayer-stacked films (5L, 10L, and 20L) of $Ca_2Nb_3O_{10}^-$ nanosheets to tune the dielectric response (ε_r = 200) in microwave frequency up to 10 GHz along with enhanced breakdown voltage up to 6 MV/cm. These ultrathin multilayer nanosheets films demonstrated high capacitance density of ~20 μF/cm^2 which was stable up to 250 ^{o}C.

In Chapter 3, I focus on LbL assembly of newly developed high-k perovskite nanosheets ($Ca_2NaNb_4O_{13}^-$; ε_r = 300) to realize ultrathin nanosheets capacitors. In

a previous report, multilayer film of $Ca_2NaNb_4O_{13}^-$ nanosheets has realized low leakage current density below 10^{-9} A/cm^2 at +1V owning to their large lateral size. Such characteristics of $Ca_2NaNb_4O_{13}^-$ nanosheets set the ground for their LbL assembly to fabricate multilayer nanosheets capacitors. Alternate deposition of metallic $Ru_{0.95}O_2^{0.2-}$ and dielectric $Ca_2NaNb_4O_{13}^-$ nanosheets has been demonstrated via LB technique. Millimeter sized, ultrathin multilayer nanosheets capacitor (~ 20 nm) fabricated on quartz glass exhibited excellent capacitance density of 52 μF/cm^2 and low leakage current density below 10^{-6} A/cm^2 at +1V.

In Chapter 4, nanosheets-based capacitors have been investigated for high-temperature applications. Two different types of nanosheets-based capacitors consisting of dielectric layers of $Ca_2Nb_3O_{10}^-$ and $Ca_2NaNb_4O_{13}^-$ nanosheets were assembled via LB technique. Metallic $Ru_{0.95}O_2^{0.2-}$ nanosheets were served as electrode layers. The dielectric and electrode layers were fabricated in specific sequences to realize metal-insulator-metal structures. A robust high-*k* response (> 155) and insulating properties (< 1 x 10^{-5} A/cm^2) were observed at high-temperatures up to 250 ^oC.

In Chapter 5, I present a new strategy to engineer ferroelectric response in 2D perovskite nanosheets superlattices. Homologous series of perovskite ($Ca_2Na_{m-3}Nb_mO_{3m+1}^-$; m = 3–6) nanosheets vary in thickness of 0.4 nm due to different number of NbO_6 octahedron units along the slab normal. The LbL assembly of homologous members of perovskite ($Ca_2Na_{m-3}Nb_mO_{3m+1}^-$; m = 3–6) nanosheets provides great control to fabricate perovskite superlattices with atomically precise interfaces and polar discontinuities to engineer dielectric/ferroelectric responses.

1.6. References

1. M.E. Lines and A.M. Glass, *Principles and Applications of Ferroelectrics and Related Materials, Oxford* (2001).
2. A.S. Bhalla, R. Guo, R. Roy, *Mat. Res. Innovat*. **4**, 3 (2000).
3. J. B. Goodenough, *Rep. Prog. Phys*. **67**, 1915 (2004).
4. N.A. Benedek, J. M. Rondinelli, H. Djani, P. Ghosez, P. Lightfoot, *Dalton Trans*. **44**, 10543 (2015).
5. L. Wang, L. Y. Ding, S. T. Zhang, Y. F. Chen, Z. G. Liu, *Solid State Commun*. **149**, 2061 (2009).
6. M. M. Fang, C. H. Kim, T. E. Mallouk, *Chem. Mater*. **11**, 1519 (1999).
7. B. W. Li, M. Osada, Y. Ebina, T. C. Ozawa, R. Ma, T. Sasaki, *Appl. Phys. Lett*. **96**, 182903 (2010).
8. N. Setter, R. Waser, *Acta Mater*. **48**, 151 (2000).
9. D. G. Schlom, L. Q. Chen, X. Pan, A. Schmehl, M. A. Zurbuchen, *J. Am. Ceram. Soc*. **91**, 2429 (2008).
10. L. W. Martin, Y. H. Chu, R. Ramesh, *Mater. Sci. Eng. R*. **68**, 89 (2010).
11. M. Osada, T. Sasaki, *Adv. Mater*. **24**, 210 (2012).
12. M. H. Frey, D. A. Payne, *Phys. Rev. B* **54**, 3158 (1996).
13. K. Ishikawa, K. Yoshikawa, N. Okada, *Phys. Rev. B* **37**, 5852 (1988).
14. T. Tybell, C. H. Ahn, J. M. Triscone, *Appl. Phys. Lett.* **75**, 856 (1999).
15. J. Petzelt, *Ferroelectrics* **400**, 117 (2010).
16. D. Damjanovic, *Rep. Prog. Phys*. **61**, 1267 (1998).
17. T. Mitsui, J. Furuichi, *Phys. Rev.* **90** 193 (1953).
18. T. M. Shaw, S. T. McKinstry, P. C. McIntyre, *Annu. Rev. Mater. Sci*. **30**, 263 (2000).
19. L. S. Zhang, W. Z. Wang, L. Zhou, H. L. Xu, *Small* **3**, 1618 (2007).
20. V. Chevallier, G. Nihoul, V. Madigou, *J. Solid State Chem*. **181**, 439 (2008).
21. R. K. Iler, *J. Colloid Interface Sci.* **21**, 569 (1966).
22. J. J. Kirkland, *Anal. Chem*. **37**, 1458 (1965).
23. T. C. Ozawa, K. Fukuda, K. Akatsuka, Y. Ebina, T. Sasaki, K. Kurashima, K. Kosuda, *J. Phys. Chem. C* **112**, 1312 (2008).
24. R. E. Schaak, T. E. Mallouk, *Chem. Mater.* **12**, 2513 (2000).

25. R. E. Schaak, T. E. Mallouk, *Chem. Mater.* **14**, 1455 (2002).
26. L. S. Zhang, W. Z. Wang, L. Zhou, H. L. Xu, *Small* **3**, 1618 (2007).
27. S. Ida, C. Ogata, U. Unal, K. Izawa, T. Inoue, O. Altuntasoglu, Y. Matsumoto, *J. Am. Chem. Soc*. **129**, 8956 (2007).
28. V. Chevallier, G. Nihoul, V. Madigou, *J. Solid State Chem*. **181**, 439 (2008).
29. Y. Ebina, K. Akatsuka, K. Fukuda, T. Sasaki, *Chem. Mater*. **24**, 4201 (2012).
30. M. Stengel, N. A. Spaldin, *Nature* **443**,679 (2006).
31. M. Osada, T. Sasaki, *J. Mater. Chem*. **19**, 2503 (2009).
32. R. K. Iler, *J. Colloid Interface Sci*. **21**, 569 (1966).
33. J. J. Kirkland, *Anal. Chem*. **37**, 1458 (1965).
34. G. Decher, *Science* **277**, 1232 (1997).
35. M. Osada, T. Sasaki, *Polym. J.,* **47**, 89 (2015).
36. B. W. Li, M. Osada, T. C.Ozawa, Y. Ebina, K. Akatsuka, R. Ma, H. Funakubo, T. Sasaki, *ACS Nano* **4**, 6673 (2010).
37. M. Osada, K. Akatsuka, Y. Ebina, H. Funakubo, K. Ono, K. Takada and T. Sasaki, ACS Nano **4**, 5225 (2010).
38. B. W. Li, M. Osada, Y-H Kim, Y. Ebina, K. Akatsuka, T. Sasaki, *J. Am. Chem. Soc.* **139**, 10868 (2017).
39. B. W. Li, M. Osada, Y. Ebina, S. Ueda, T. Sasaki, *J. Am. Chem. Soc*. **138**, 7621 (2016).

Chapter 2

Layer-by-Layer Engineering of Perovskite Nanosheets

2.1. Introduction

2D perovskite nanosheets provide remarkable potentials for designing thin-film architectures and nanodevices. Recent studies on perovskite nanosheets have demonstrated that the LB-based LbL approach is an effective way for fabricating uniform and densely packed multilayer films. An important challenge is to use perovskite nanosheets as core device component. The potential advantage of perovskite nanosheets is their molecular thickness, surpassing nanostructures that can be attained by conventional down-sizing approaches. Therefore, LbL approach using perovskite nanosheets has a great potential for solution-processed electronics, especially for dielectric components.

High-*k* dielectrics are very important for making smaller devices and improving the packaging density of electronic components. Of particular importance are capacitor components that are ubiquitous in electronic devices and systems. Because capacitors are the largest components in current electronic devices, increasing their capacitance in smaller areas/volumes is an important step for the relentless advances in microelectronic technologies. In microwave applications, the capacitors are embedded as a thin-film configuration on the chip to avoid the large paraelectric inductance in surface-mounted capacitors.

Ferroelectric perovskites such as $BaTiO_3$, $(Ba_{1-x}Sr_x)TiO_3$ and $Pb(Zr, Ti)O_3$ are a prime target for capacitor applications. However, they suffer from stability issues (such as high temperature coefficient, strong frequency dependence and low breakdown voltage) due to the ferroelectric phase transition. To overcome these issues, polymer-ceramic composites have been extensively studied because they combine the high breakdown strength of polymers with the high-*k* value of ferroelectric ceramic nanoparticles. In composite dielectrics, however, the dielectric constant is still limited (< 30) due to low-*k* value of polymer matrix.[3-5] From material viewpoint, the capacitor performance can be improved by increasing dielectric constant, and the dielectric loss is diminished by reducing polarization hysteresis and dissipation factor.

An ideal material should demonstrate high-*k* dielectric and highly insulating responses at nanoscale thickness. Furthermore, it should be free from stability issues related to high frequencies, large voltages/electric fields and elevated

temperatures. Moreover, multilayer films of ideal system should be free from extrinsic effects such as low-*k* dead layer and strain effects in order to realize full potential of intrinsic properties of the film.

$Ca_2Nb_3O_{10}^-$ nanosheets is an ideal perovskite with ultrathin thickness of 1.5 nm, which corresponds to three NbO_6 octahedra along the block normal. These are near perfect, thinnest self-standing crystals. Previously reported work realized atomically clean interfaces demonstrating excellent intrinsic properties. In previous studies, multilayer films of $Ca_2Nb_3O_{10}^-$ nanosheets exhibited stable dielectric properties of ~ 210 up to 10 MHz frequency and high leakage current density of $< 10^{-7}$ A/cm^2 at 2V.[2] In another study, monolayer film of $Ca_2Nb_3O_{10}^-$ nanosheets demonstrated high thermal stability up to 700 ^oC.[6] Furthermore, conducting atomic force microscopy (AFM) observation of individual $Ca_2Nb_3O_{10}^-$ nanosheet confirmed its highly insulating nature. Whereas, monolayer film of $Ca_2Nb_3O_{10}^-$ nanosheets observed to exhibit conducting paths only at the boundaries of each nanosheet, which were diminished in case of bilayer film of $Ca_2Nb_3O_{10}^-$ nanosheets (Figure 2.1).[7] Additionally, due to quantum confinement effect, $Ca_2Nb_3O_{10}^-$ nanosheets possess larger band gap of ~ 3.8 eV as compared to bulk cases. These reported characteristics make $Ca_2Nb_3O_{10}^-$ nanosheets an important material to investigate dielectric and insulating properties at high frequency and voltages to establish new direction of application for $Ca_2Nb_3O_{10}^-$ perovskite nanosheets.

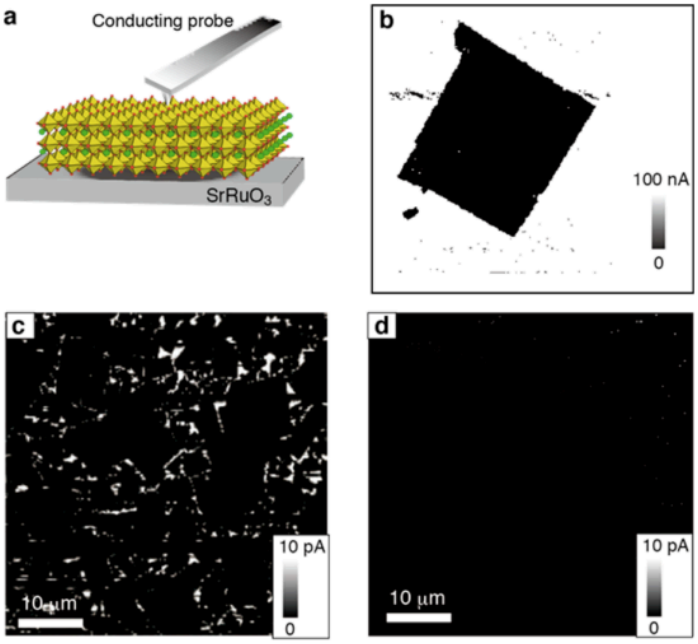

Figure 2.1. Insulating behavior of ultrathin perovskite layers. (a, b) Schematic illustration and conducting AFM image of individual $Ca_2Nb_3O_{10}^-$ nanosheet on a $SrRuO_3$ substrate. (c, d) Current mapping of monolayer and bilayer LB films of $Ca_2Nb_3O_{10}^-$ nanosheets on a $SrRuO_3$ substrate. Adopted with permission.[7] Copyright 2017, American Chemical Society.

According to first-principle calculations, $Ca_2Nb_3O_{10}^-$ nanosheets possess large atomic polarization and hence realize high-*k* properties. Such high-*k* response is structural feature of $Ca_2Nb_3O_{10}^-$ nanosheets. In microwave frequency region, atomic polarizations can take place, which enlighten the potential application of multilayer films of $Ca_2Nb_3O_{10}^-$ nanosheets for microwave devices. To best of my knowledge, there are no studies in which dielectric properties of multilayer film of $Ca_2Nb_3O_{10}^-$ nanosheets are studied in microwave frequency regions and leakage current density in large electric fields up to 6 MV/cm.

Here I demonstrate a new materials design for microwave capacitor dielectrics using high-*k* nanosheets ($Ca_2Nb_3O_{10}^-$). My approach to new dielectrics is multilayer implementation of high-*k* nanosheets with a paraelectric ground. Paraelectric materials exhibit no polarization hysteresis with a temperature-independent ε_r, ideal for realizing the temperature stability. $Ca_2Nb_3O_{10}^-$ nanosheet ($\varepsilon_r = 210$) is a new class of high-*k* nanodielectrics derived from layered compounds

by exfoliation.[8,9] Multilayered films with many nanosheet layers exhibited improved breakdown voltage due to barrier effect. LbL assembly of $Ca_2Nb_3O_{10}^-$ nanosheets also realizes frequency and temperature-stability, suitable for miniature microwave capacitor components with improved performances.

2.2. Experimental

2.2.1. Synthesis of $Ca_2Nb_3O_{10}^-$ nanosheets

$Ca_2Nb_3O_{10}^-$ nanosheets are exfoliated from their layered perovskites ($KCa_2Nb_3O_{10}$) as reported previously.[10] The starting layered material ($KCa_2Nb_3O_{10}$) was synthesized by solid-state reaction of K_2CO_3, $CaCO_3$ and Nb_2O_5 (1.05/2/3) at 1473 K for 12 h in air. The resulting layered material; $KCa_2Nb_3O_{10}$ (5 g) was treated with 200 cm^3 of 5M HNO_3 solution to exchange potassium ions with protons for 7 days. The protonic phase was filtered and washed with excess of milli-Q water and dried in air. Through XRD, protonic-layered material was observed to be $HCa_2Nb_3O_{10}.1.5H_2O$. The exfoliation of protonic form, $HCa_2Nb_3O_{10}.1.5H_2O$, was achieved through introduction of bulky guest group. The protonic form (0.4 g) was added in 100 cm^3 of tetrabutyl ammonium hydroxide (TBAOH). The molar ratio of TBA^+/H^+ was adjusted at 1 where H^+ represents exchangeable protons in protonic form. The resulting suspension was shaken at 170 rpm in a mechanical shaker for 7 days. Thus synthesized colloidal suspension was centrifuged at 1500 rpm for 10 min to separate unexfoliated residues.

2.2.2. Fabrication of multilayer films using $Ca_2Nb_3O_{10}^-$ nanosheets

Multilayer films of $Ca_2Nb_3O_{10}^-$ nanosheets were fabricated on atomically flat substrate such as $SrRuO_3$ and $(LaAlO_3)_{0.3}(Sr_2TaAlO_6)_{0.7}$ (LSAT). For the fabrication of multilayer films of $Ca_2Nb_3O_{10}^-$ nanosheets, LbL assembly process through LB deposition was adopted.[6] The fabrication procedure for monolayer film of $Ca_2Nb_3O_{10}^-$ nanosheets starts with the preparation of diluted suspension of perovskite $Ca_2Nb_3O_{10}^-$ nanosheets (96 mg/dm^3) as subphase. A schematic procedure for the deposition of monolayer films of $Ca_2Nb_3O_{10}^-$ nanosheets is given

in Figure 2.1. The diluted suspension of $Ca_2Nb_3O_{10}^-$ nanosheets was dispersed in LB trough (Figure 2.1a). The surface pressure of floating nanosheets can be observed with the help of Wilhelmy-type sensor. Through pressure-area (π-A) curve it was possible to observe 3 different regions of packing density starting with loosely packed nanosheet initially followed by densely packed monolayer films and lastly the over-packed monolayer films containing many overlaps. Figure 2.1c expresses the brief cartoon for the fabrication of monolayer films of $Ca_2Nb_3O_{10}^-$ nanosheets. In the first step, the diluted suspension of $Ca_2Nb_3O_{10}^-$ nanosheets was spread in LB trough and waited for 5 min to get stable nanosheets suspension surface. $Ca_2Nb_3O_{10}^-$ nanosheets floated at the air-water interface were well spread. The compression of nanosheet film was achieved by inward movement of barriers at a speed of 0.50 mm s^{-1} to get densely packed monolayer film of $Ca_2Nb_3O_{10}^-$ nanosheets floating at air/water interface. As desired surface pressure of 15 ± 0.5 mN/m was achieved, it was maintained for 10 minutes to achieve high surface stability of $Ca_2Nb_3O_{10}^-$ nanosheets. The transfer of monolayer films from water surface on to solid substrate was followed by substrate lift-up step at a speed of 0.0167 mm s^{-1}. The substrates containing monolayer films were washed with copious amount of water to remove excess of TBA^+ ions used during exfoliation followed by drying at 110 ^oC for 10 min and UV irradiation by Xe lamp for 10 min. Above procedure was followed *n* number of times to achieve desired number of layers of $Ca_2Nb_3O_{10}^-$ nanosheets. The fabricated films were then kept under heat treatment at 400 ^oC for 6 hours to decompose TBAOH present within the galleries of multilayers.

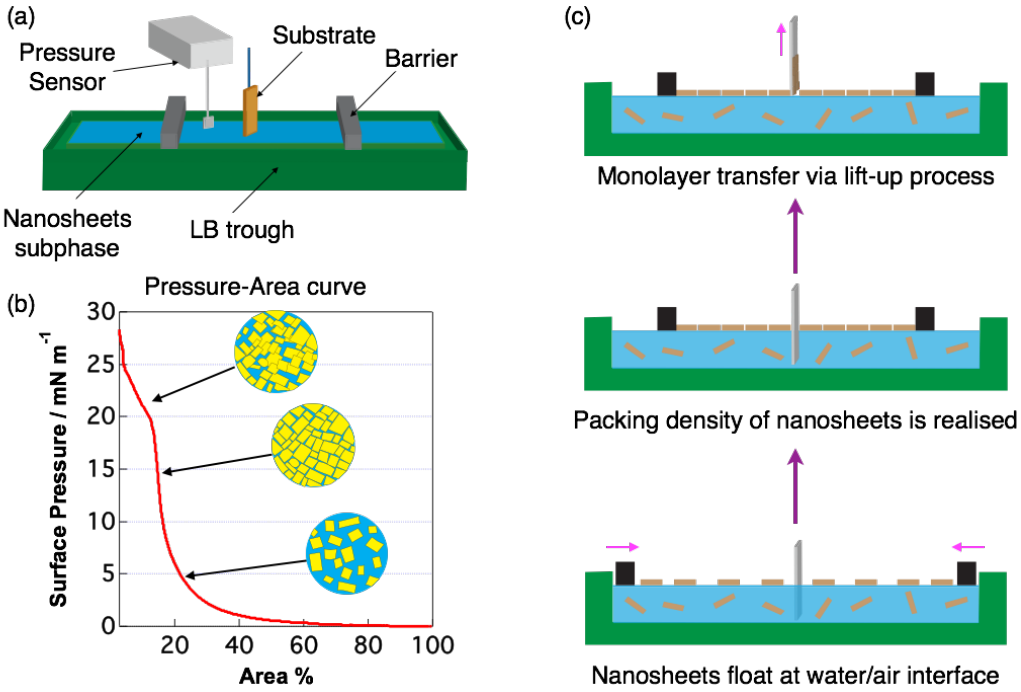

Figure 2.2. Schematic illustration of monolayer film deposition from liquid phase on to the solid substrate. **(a)** Cartoon of LB trough, **(b)** Pressure-area curve **(c)** Schematic to illustrate floating nanosheet at air/water interface, their close assembly by controlling compression of barrier followed by transfer of monolayer film on the solid substrate through lift-up process.

2.2.3. Characterization

LbL assembly of perovskite nanosheets have been realized using USI FSD-3-777 that contains double barrier trough in contact with a Wilhelmy-type balance for observing surface pressure (Figure 2.3). Multilayer film structure was evaluated with Hitachi H-9000 microscope functioning at 200 kV. Dielectric and insulating response of multilayer films of $Ca_2Nb_3O_{10}^-$ nanosheets were explored with the help of microprobe station at variable temperatures using a precision impedance analyzer (Agilent 4294A) and semiconductor parameter analyzer (Keithley 4200-SCS), respectively.

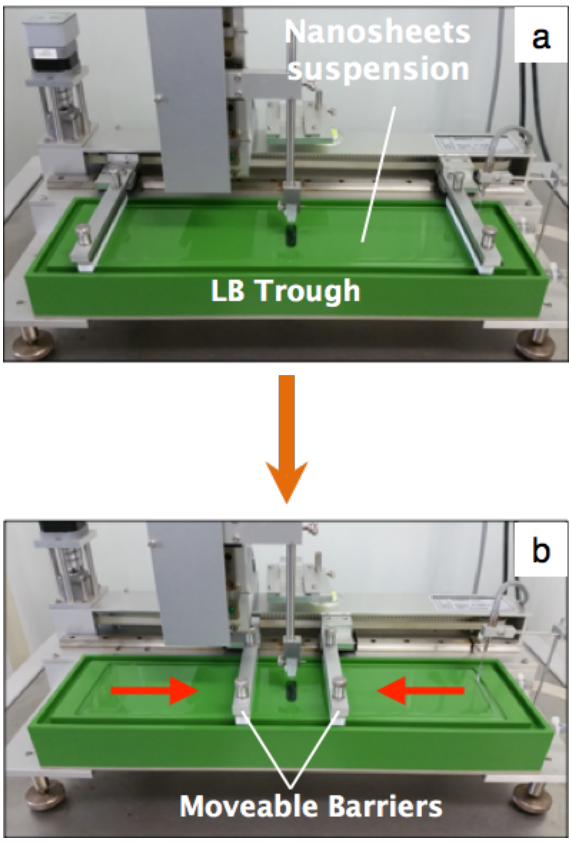

Figure 2.3. Experimental setup for LbL assembly of oxide nanosheets in our laboratory. **(a)** Exhibition of nanosheets suspension in LB trough, **(b)** Inward movement of barrier to get closely packed nanosheets film floating at air/water interface.

Coplanar waveguide (CPW) device were designed on $(Ca_2Nb_3O_{10}^-)_n$/LSAT through lithography, followed by deposition of Ti/Au electrodes (10/100 nm) and measurement of broadband dielectric properties in the range of 1 MHz 10 GHz. [11,12] The design of CPW device demonstrates 60 μm center conductor in thickness, possess 20 μm gaps, and contains 200-μm-wide ground planes. Radio frequency and microwave vector network analyzers are used to observe complex scattering parameters (*S*-parameters). The capacitance was transformed to in-plane dielectric constant of multilayer films.

2.3. Results and Discussion

2.3.1. Characterization of $Ca_2Nb_3O_{10}^-$ films

LB method is an effective technique for the realization of highly organized monolayer films of perovskite nanosheets. I successfully fabricated monolayer film of $Ca_2Nb_3O_{10}^-$ nanosheets with the use of atomically flat $SrRuO_3$ substrate to achieve atomically uniform monolayer film as shown in Figure 2.4. The same procedure given above is proceeded specific number of times to realize three different multilayer films (5L, 10L, 20L) of $Ca_2Nb_3O_{10}^-$ nanosheets. The resultant multilayer films were kept under heat treatment at 400 ^oC for 6 hours to decompose TBAOH present within the galleries of multilayers.

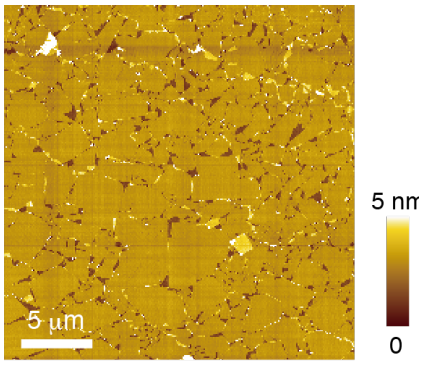

Figure 2.4. AFM image for a monolayer LB film of $Ca_2Nb_3O_{10}^-$ nanosheets.

Successful fabrication of multilayer films (~ 20 layers) has been examined via cross-sectional HRTEM. As displayed in Figure 2.5, the lamellar structure of multilayer film can be observed confirming the high quality of multilayer films on atomically flat substrate. Moreover, clean interface between dielectric layer and substrate was achieved with no interdiffusion. Through LB method, it is possible to fabricate dead-layer free multilayer films. Multilayer films of similar quality were also fabricated on LSAT substrate.

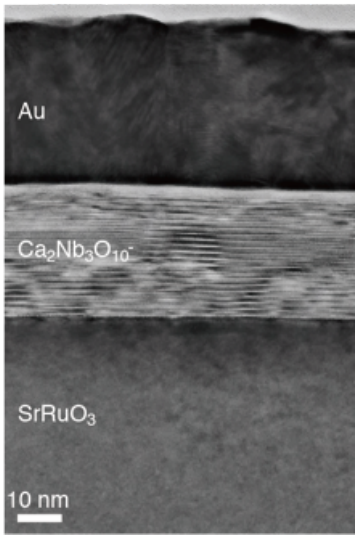

Figure 2.5. Cross-sectional HRTEM image of an Au/$(Ca_2Nb_3O_{10}^-)_n$/$SrRuO_3$ nanocapacitor (n = 20).

2.3.2. Dielectric properties of $Ca_2Nb_3O_{10}^-$ nanosheets

Firstly, insulating properties of multilayer films of $Ca_2Nb_3O_{10}^-$ nanosheets were observed. The measurements were performed by making metal-insulator-metal structure i.e. Au/$Ca_2Nb_3O_{10}^-$/$SrRuO_3$. Leakage current density was studies as factor of electric field for different multilayer films of $Ca_2Nb_3O_{10}^-$ nanosheets. All the films demonstrated excellent insulating properties, which showed an increasing insulation with increasing the number of layers. For 5-layer films, highly insulting properties below ~ 10^{-7} were observed (Figure 2.6). 5-layer film demonstrated a strong dielectric durability and high breakdown strength of ~3.5 MV/cm. The inset of Figure 2.5 confirms the improved response in breakdown strength for films with higher number of $Ca_2Nb_3O_{10}^-$ layers. For 20-layered $Ca_2Nb_3O_{10}^-$ films, significant enhancement in breakdown voltage ~6 MV/cm was observed. The improvement in breakdown voltage can be justified as barrier effect present in multilayer films of $Ca_2Nb_3O_{10}^-$ nanosheets. This response of enhanced breakdown voltage is analogous to phenomenon expressed by multilayer films of dielectric polymers.[13] In dielectric polymer films, the enhanced breakdown strength can be associated to presence of thin barrier along with dielectric layers that effectively blocks the transfer of charge carriers across the film. In multilayer film of $Ca_2Nb_3O_{10}^-$ nanosheets, dielectric layers and interfaces act as many barrier

layers to demonstrate enhanced breakdown voltage and decreased charge migration across the film. As reported previously, bi-layer LB films of $Ca_2Nb_3O_{10}^-$ nanosheets are highly insulating.[14] As a result; increasing number of multilayers films of $Ca_2Nb_3O_{10}^-$ nanosheets can ensure high breakdown strength. Second possibility for increased breakdown strength is 2D confinement effect. In case of lamellar dielectric films comprised of thin layers, usually dielectric strength increase with decrease in dielectric thickness due to flaw concentration effects.[15] Moreover, 2D $Ca_2Nb_3O_{10}^-$ nanosheets possess larger bandgap of ~3.8 eV due to quantum size effect results in improving the breakdown strength.[16,17]

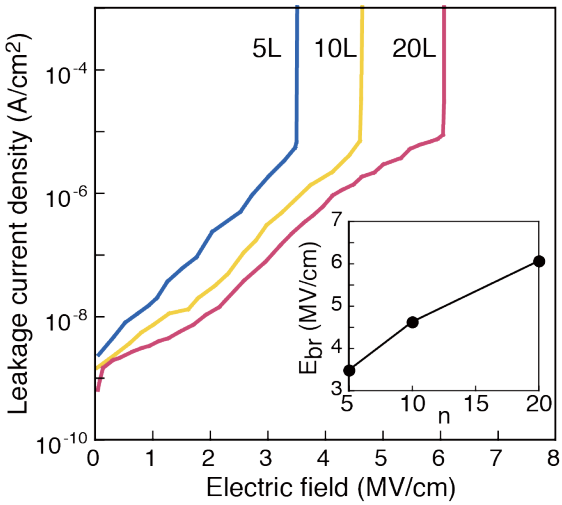

Figure 2.6. Leakage current density of Au/$(Ca_2Nb_3O_{10}^-)_n$/$SrRuO_3$ capacitors. (Inset) Thickness dependence of the dielectric strength (E_{br}) for $(Ca_2Nb_3O_{10}^-)_n$.

Frequency dependent ε_r response was measured for multilayer $Ca_2Nb_3O_{10}^-$ films (Figure 2.7). Multilayer films of $Ca_2Nb_3O_{10}^-$ nanosheets exhibited a stable dielectric behavior in 5-layer films in ultrathin form (< 10nm) due to its paraelectric nature. The observed ε_r value was ~200 at 1 - 10 GHz, a value in accordance with former low-frequency observations (1 kHz - 1 MHz). A stable dielectric response was observed at high frequencies up to 10 GHz. In contrast, ferroelectric films of $(Ba_{1-x}Sr_x)TiO_3$ and Pb(Zr, Ti)O_3 exhibit a significant dependence with respect to frequency at GHz region resulting in degradation of ε_r due to dielectric relaxation and domain contribution.[18]

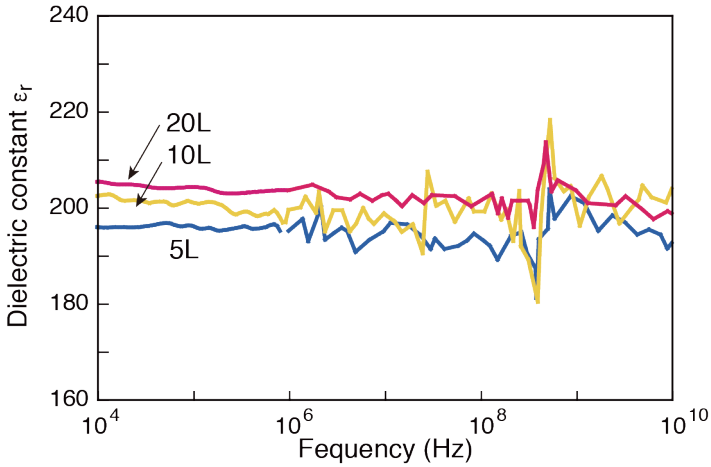

Figure 2.7. Frequency dependence of the dielectric constant of $(Ca_2Nb_3O_{10}^-)_n$ (n = 5, 10, 20).

Figure 2.8 presents the dielectric response as a function of electric field for 20-layered film at 25 and 250 °C. Robust high-k properties were observed at high temperature up to 250 °C; a small degradation in ε_r response is observed but the ε_r value was high enough (~ 195). Due to paraelectric nature of $Ca_2Nb_3O_{10}^-$ nanosheets, a linear ε_r-E curves was observed.

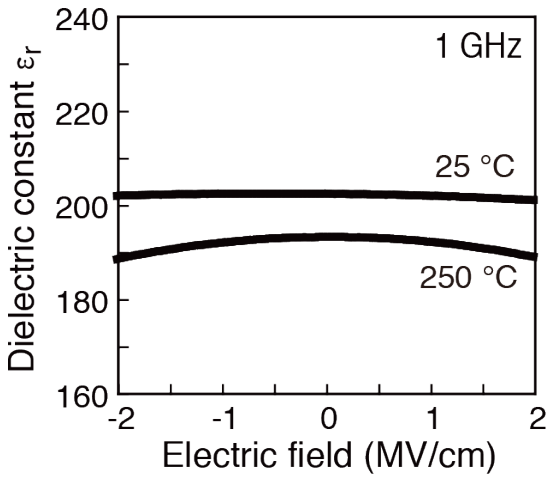

Figure 2.8. Electric field dependence of the dielectric constant of $(Ca_2Nb_3O_{10}^-)_n$ (n = 20) at 1 GHz.

Figure 2.9 shows the capacitance response of different perovskite film at elevated temperatures up to 250 °C. High-k perovskites film such as $(Ba_{1-x}Sr_x)TiO_3$ exhibited a significant decrease in capacitance in response to

increased temperatures. Where as, $Ca_2Nb_3O_{10}^-$ nanosheets film displayed a stable capacitance up to 250 ^oC with small variation of 3%. The τ was −180 ppm/K, which is much smaller than that of typical high-*k* dielectrics (−1000 ppm/K for $Ba_{1-x}Sr_xTiO_3$).[19,20]

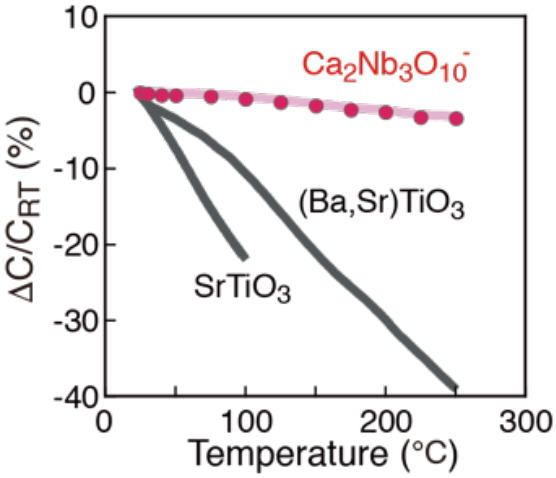

Figure 2.9. Temperature variation of the capacitance relative to RT value for $(Ca_2Nb_3O_{10}^-)_n$ (n = 20) and perovskite thin films.

These results are signature of potential applications of perovskite $Ca_2Nb_3O_{10}^-$ nanosheets as high-*k* dielectric material. International Technology Roadmap for Semiconductors (ITRS) define the minimum limit of capacitance (> 1 $\mu F/cm^2$) for dielectric layers in high-frequency circuits. Interestingly, $Ca_2Nb_3O_{10}^-$ nanosheets demonstrate high ε_r values (~ 200) at thickness < 30nm, which is completely different in case of size-induced deprivation in $Ba_{1-x}Sr_xTiO_3$. In case of dielectric materials with dielectric constant > 50 usually possess small bandgap (~ 3 eV) and low breakdown strength < 3MV/cm. Whereas, in case of dielectric materials with large breakdown strength usually have low dielectric constant < 20 (Figure 2.10).[21]. The concomitant high ε_r along with high breakdown voltage in multilayer perovskite $Ca_2Nb_3O_{10}^-$ nanosheets is quite unique. $Ca_2Nb_3O_{10}^-$ nanosheet demonstrate high capacitance density of ~ 20 $\mu F/cm^2$ that is two order magnitude higher than current available ceramic materials.

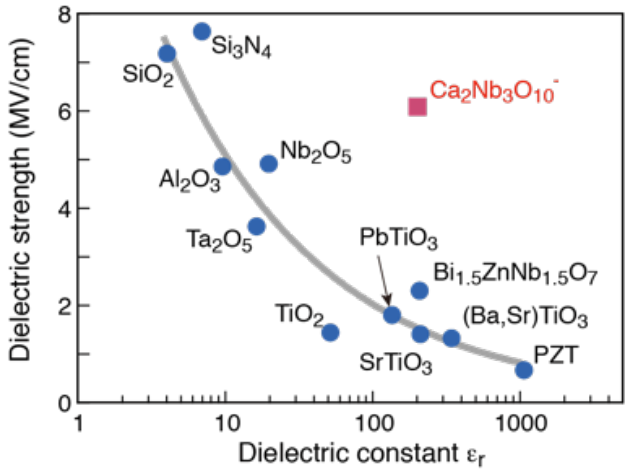

Figure 2.10. Dielectric strength versus dielectric constant for various dielectrics.

The possible origin of high-*k* response and high breakdown strength in multilayer films can be associated to intrinsic and extrinsic effects. From theoretical point of view, first principle calculations state that $Ca_2Nb_3O_{10}^-$ nanosheet demonstrate large atomic polarization and softening of soft phonon, which result in enhanced dielectric properties. From experimental aspects, conducting AFM observation testify the highly insulating properties of monolayer of $Ca_2Nb_3O_{10}^-$ nanosheet. Secondly, large band gap of ~3.8 eV also contribute to highly insulating nature of $Ca_2Nb_3O_{10}^-$ nanosheet. Figure 2.4 is signature of high quality nanofilms of $Ca_2Nb_3O_{10}^-$ nanosheet on $SrRuO_3$ substrate with clean interface ruling out the possibility of low-*k* dead layer. As a result, multilayer films of $Ca_2Nb_3O_{10}^-$ nanosheet can realize full potential of high-*k* property. Multilayer implementation is also quite important to realize enhanced breakdown strength in 20L $Ca_2Nb_3O_{10}^-$ nanosheets film. There are two possibilities of enhanced breakdown strength in 20L $Ca_2Nb_3O_{10}^-$ nanosheet film. First possibility is ultrathin profile of $Ca_2Nb_3O_{10}^-$ nanosheets. Usually very thin dielectric demonstrate enhanced breakdown strength. In case of dielectric with decrease thickness demonstrate increase in breakdown strength due to decrease of defects and can be named as flaw concentration effects. Due to this reason $Ca_2Nb_3O_{10}^-$ nanosheet realize highly insulting nature even at monolayer level. Second reason may include the presence of barrier effect offered by large number of dielectric layers and interfaces in the multilayered film to breakdown and charge migration within

the film.

2.4. Summary

In this work, I have successfully fabricated multilayer films of perovskite $Ca_2Nb_3O_{10}^-$ nanosheet on various substrates. LbL assembly using LB method is an effective strategy to fabricate atomically uniform and highly dense monolayer film, which was confirmed with AFM. The resultant monolayer film deposition was repeated *n* times to achieve multilayer nanofilms. I investigated the lamellar structure of resultant multilayer films with the help of cross-sectional HRTEM. Through cross-sectional HRTEM, it was obvious that multilayer $Ca_2Nb_3O_{10}^-$ nanosheets films covered the substrate surface with uniform and dense packing with no signs of interdiffusion. Multilayer films of perovskite $Ca_2Nb_3O_{10}^-$ nanosheet realized frequency and temperature dependent stable permittivity and improved breakdown voltages. Perovskite nanosheets films demonstrated high ε_r values of ~ 200 and ~195 up to 10 GHz and 250 ^oC, respectively. Nanosheets-based films exhibited high capacitance density of ~ 20 $\mu F/cm^2$ at higher temperatures up to 250 ^oC. Perovskite films displayed a stable capacitance up to 250 ^oC with small variation of 3%. The τ was −180 ppm/K, which is much smaller than that of typical high-*k* dielectrics (−1000 ppm/K for $Ba_{1-x}Sr_xTiO_3$). The simultaneous presence of high-*k* dielectric properties and high breakdown voltage of multilayer $Ca_2Nb_3O_{10}^-$ nanosheets films make it superior material as compared to other oxide dielectrics, which either demonstrate high-*k* dielectric response or high breakdown voltage. In the end, it was concluded that presence of intrinsic and extrinsic effect resulted in superior dielectric properties in microwave region for multilayer films of $Ca_2Nb_3O_{10}^-$ nanosheets. The enhanced breakdown strength can be justified due to presence of flaw concentration effect and barrier effect from ultrathin profile of dielectric and multilayer implementation technique of $Ca_2Nb_3O_{10}^-$ nanosheets, respectively. The characteristics of perovskite films along with facile fabrication procedure possess great advantages that are not possible to achieve through vacuum based thin film deposition processes.

2.5. References

1. T. M. Shaw, Z. Suo, M. Huang, E. Liniger, R. B. Laibowitz, J. D. Baniecki, *Appl. Phys. Lett.* **75**, 2129 (1999).
2. M. Osada, T. Sasaki, *Adv. Mater.* **24**, 210 (2012).
3. J. A. Bur, *Polymer* **26**, 963 (1985).
4. S. Rimdusit, H. Ishida, *Polymer* **41**, 7941 (2000).
5. S. George, P. S. Anjana, M. T. Sebastian, J. Krupka, S. Uma, J. Philip, *Int. J. Appl. Ceram. Technol.* **7**, 461 (2010).
6. B. W. Li, M. Osada, Y. Ebina, K. Akatsuka, K. Fukuda, T. Sasaki, *ACS Nano* **8,** 5449 (2014).
7. B. W. Li, M. Osada, Y-H Kim, Y. Ebina, K. Akatsuka, T. Sasaki, *J. Am. Chem. Soc.* **139**, 10868 (2017).
8. M. Osada, K. Akatsuka, Y. Ebina, H. Funakubo, K. Ono, K. Takada, T. Sasaki, *ACS Nano* **4**, 5225 (2010).
9. H. -J. Kim, M. Osada, T. Sasaki, *Jpn. J. Appl. Phys.* **55**, 1102A3 (2016).
10. Y. Ebina, T. Sasaki, M. Watanabe, *Solid State Ionics* **151**, 177 (2002).
11. C. -H. Lee, N. D. Orloff, T. Birol, Y. Zhu, V. Goian, E. Rocas, R. Haislmaier, E. Vlahos, J. A. Mundy, L. F. Kourkoutis, Y. Nie, M. D. Biegalski, J. Zhang, M. Bernhagen, N. A. Benedek, Y. Kim, J. D. Brock, R. Uecker, X. X. Xi, V. Gopalan, D. Nuzhnyy, S. Kamba, D. A. Muller, I. Takeuchi, J. C. Booth, C. J. Fennie, D. G. Schlom, *Nature* **502**, 532 (2013).
12. N. D. Orloff, W. Tian, C. J. Fennie, C. H. Lee, D. Gu, J. Mateu, X. X. Xi, K. M. Rabe, D. G. Schlom, I. Takeuchi, J. C. Booth, *Appl. Phys. Lett.* **94**, 042908 (2009).
13. M. Mackey, D. E. Schuele, L. Zhu, E. Baer, *J. Appl. Phys.* **111**, 113702 (2012).
14. B. W. Li, M. Osada, Y. -H Kim, Y. Ebina, K. Akatsuka, T. Sasaki, *J. Am. Chem. Soc.* **139**, 10868 (2017).
15. M. Mackey, A. Hiltner, E. Baer, L. Flandin, M. A. Wolak, J. S. Shirk, *J. Phys. D* **42**, 175304 (2009).
16. K. Akatsuka, G. Takanashi, Y. Ebina, M. Haga, T. Sasaki, *J. Phys. Chem. C* **116**, 12426 (2012).
17. P. Xu, T. J. Milstein, T. E. Mallouk, *ACS Appl. Mater. Interfaces* **8**, 11539

(2016).
18. T. Teranishi, T. Hoshina, T. Tsurumi, *Mater. Sci. Eng. B* **161**, 55 (2009).
19. P. Bao, T. J. Jackson, X. Wang, M. J. Lancaster, *J. Phys. D: Appl. Phys.* **41**, 063001 (2008).
20. C. V. Weiss, M. B. Okatan, S. P. Alpay, M. W. Cole, E. Ngo, R. C. Toonen, *J. Mater. Sci.* **44**, 5364 (2009).
21. Y. Imanaka, T. Shioga, J. D. Baniecki, *Fujitsu Sci. Tech. J.* **38**, 22 (2002).

Chapter 3

Hetero Assembly of Perovskite Nanosheets for Multilayer Nanosheets Capacitors

3.1. Introduction

Relentless demand for electronic devices with small package sizes and increased performances, significantly directed intense research to design smaller but superior active and passive components. Many of these components employ ferroelectric and dielectric perovskites oxides as core materials. A few examples include multilayer ceramic capacitors (MLCCs), radio frequency and microwave antennae, nonvolatile memories, sensors and actuators. These applications usually employ $BaTiO_3$, $(Ba_{1-x}Sr_x)TiO_3$ and $Pb(Zr, Ti)O_3$ as important dielectric materials with thickness of an order of 1 μm or less.[1-3] To operate at reduced voltages and achieve high capacitance, these applications used either submicron size grains or thin ferroelectric films. As the physical dimensions of ferroelectrics are reduced, it usually results in decreased phase transition temperatures and reduced ferroelectric distortion, which leads to either complete loss or significant decline in polarization and hence reduced permittivity.[4-7] These effects can be refer as fundamental size effects and are common in ferroelectric materials. It is concluded from experimental and theoretical work that when ferroelectric materials with at least one dimension in range of 10s of nm, demonstrate fundamental size effect significantly.[8-11]

To solve this problem, 2D materials technology is emerging strategy with the objective of using 2D oxide nanosheets to build ultrathin heterostructure that exhibit interesting physical properties that are not possible to achieve in bulk systems. Here, important direction is capacitors, which are largest components in electronic devices. An important issue is to increase their capacitance with smaller areas/volumes. In this regard, perovskite nanosheets with high-*k* characteristics and ultrathin thickness are ideal material for the LB-based LbL assembly to achieve novel nanofilms.

Here it is quite important to compare the dielectric properties of ultrathin films of perovskite nanosheets with the dielectric properties of conventional ferroelectric materials when they are reduced down to few 10s nm in thickness (Figure 1.6).[12] It can be observed that multilayer films of perovskite nanosheets with ultrathin thickness (< 20 nm) demonstrated excellent dielectric properties as

compared to various conventional perovskite thin films such as $(Ba_{1-x}Sr_x)TiO_3$, and $SrBi_2Ti_2O_9$. The simultaneous presence of high-*k* characteristics and ultrathin thickness of perovskite nanosheets makes them ideal building blocks for the fabrication of nanodevices. A new direction for compact capacitor design is to use 2D perovskite nanosheets as core device component. This can be achieved by engaging 2D perovskite nanosheets to realize ultrathin films fabricated via LbL method, which can demonstrate excellent dielectric characteristic at ultrathin thickness (< 20 nm).

2D materials establish new direction with the advantage of molecular thickness to fabricate ultrathin devices. LbL assembly of 2D perovskite nanosheets possesses potential advantage of room temperature solution-based assembly process. Li *et al.* demonstrated that multilayer films of 2D perovskite nanosheets ($Ca_2Na_{m-3}Nb_mO_{3m+1}^-$; m = 3-6) demonstrate high-*k* response of over 200 when assembled through LB technique. These high-*k* properties of multilayer films of homologous series of perovskite nanosheets are intrinsic properties of these films due to high quality of respective films with absence of extrinsic factor such as strain effect or low-*k* dead layer effect at interface. Among these perovskites the leakage current density was observed to be least for ($Ca_2NaNb_4O_{13}$; m = 4) due large lateral size that resulted in decreased leakage boundaries in that multilayer film.[12] Li *et al.* reported that $Ca_2Nb_3O_{10}^-$ based multilayer capacitor when assembled in a LbL method interspersed between metallic $Ru_{0.95}O_2^{0.2-}$ nanosheets films as electrode, has realized high capacitance density (27.5 μF/cm^2).[13] The overall thickness of $Ca_2Nb_3O_{10}^-$ based multilayer capacitor was observed to be 28 nm. However, this work utilized small area electrodes (< 100 μmΦ) of $Ru_{0.95}O_2^{0.2-}$ nanosheets fabricated via photolithography followed by sequential adsorption of $Ru_{0.95}O_2^{0.2-}$ nanosheets electrode. For practical application, assemblies of large-area electrode films are required to make superior devices.

In this work, perovskite nanosheets ($Ca_2NaNb_4O_{13}^-$; ε_r = 300) with molecular thickness of ~ 2 nm have been employed as dielectric layers. The purpose of choosing $Ca_2NaNb_4O_{13}^-$ nanosheets among other homologous members of perovskite nanosheets ($Ca_2Na_{m-3}Nb_mO_{3m+1}^-$; m = 3-6) is to find a delicate balance between dielectric and leakage properties among various nanosheets.

$Ca_2NaNb_4O_{13}^-$ and $Ru_{0.95}O_2^{0.2-}$ nanosheets have been assembled via LbL technique at alternate sequences. $Ca_2NaNb_4O_{13}^-$ nanosheets characterized as 2D single crystal contains four NbO_6 octahedra blocks along thickness that are susceptible to large polarizability. The large lateral size over 10 μm for $Ca_2NaNb_4O_{13}^-$ nanosheets is helpful to realize insulating dielectric film even < 10 nm due to decrease leakage paths. The fabrication procedure involves the deposition of dielectric and electrode layers via LB method. The resultant MNCs structure consists of two dielectric films of $Ca_2NaNb_4O_{13}^-$ nanosheets interspersed with three metallic films of $Ru_{0.95}O_2^{0.2-}$ nanosheets and demonstrate a total device thickness of ~ 20 nm.

3.2. Experimental

3.2.1. Synthesis of $Ca_2NaNb_4O_{13}^-$ and $Ru_{0.95}O_2^{0.2-}$ nanosheets

$Ca_2NaNb_4O_{13}^-$ and $Ru_{0.95}O_2^{0.2-}$ nanosheets were exfoliated from layered $KCa_2NaNb_4O_{13}$ and $K_{0.2}RuO_{2.1}\cdot nH_2O$ materials through a soft-chemical exfoliation process, respectively.[14,15] For the synthesis of layered $KCa_2NaNb_4O_{13}$, Na_2CO_3, K_2CO_3, $CaCO_3$ and Nb_2O_5 were used as raw materials. In the first step, $KCa_2Nb_3O_{10}$ was prepared by solid-state reaction between K_2CO_3, $CaCO_3$ and Nb_2O_5 with 1.05/2/3 molar ratios at 1473 K for 12 h in air. Simultaneously, $NaNbO_3$ was synthesized by reacting a mixture of Na_2CO_3 and Nb_2O_5 with Na/Nb = 1 at 1473 K for 12 h. Layered $KCa_2NaNb_4O_{13}$ was synthesized by reaction of equal molar ratio of $KCa_2Nb_3O_{10}$ and $NaNbO_3$ at 1573 K. The resultant layered $KCa_2NaNb_4O_{13}$ (10 g) was treated with 400 cm^3 aqueous solution of 5 M HNO_3 for 3 days followed by washing with milli-Q water and drying. The acid treated layered $HCa_2NaNb_4O_{13}\cdot 1.5H_2O$ (1.2 g) was exfoliated with the help of bulky organic TBAOH solution (300 cm^3) when molar ratio of TBA^+/H^+ was adjusted at 1. The suspension was vigorously shaken for 7 days by mechanical shaker at 170 rpm. The resulting colloidal suspension was centrifuged at 1500 rpm for 10 min to separate unexfoliated residues.

The typical exfoliation procedure for $Ru_{0.95}O_2^{0.2-}$ nanosheets starts with synthesis of layered $K_{0.2}RuO_{2.1}\cdot nH_2O$ material. The pelletized mixture of K_2CO_3 and RuO_2 at a molar ratio of 5:8 was heated at 1025 K for 12 hours in Ar

environment. The resultant layered $K_{0.2}RuO_{2.1}\cdot nH_2O$ was washed thoroughly to remove minor components and consequently treated with 1 molar HCl aqueous solution for 3 days to exchange K^+ ions with protons. The protonated layered $H_{0.2}RuO_{2.1}\cdot 0.9H_2O$ (0.2g) was added in 50 cm^3 of aqueous TBAOH solution with molar ratio of TBA^+/H^+ at 5 (Figure 3.1). After 10 days of vigorous shaking, the auburn suspension was centrifuged at 2000 rpm for 30 min to separate exfoliated nanosheets from unexfoliated residues.

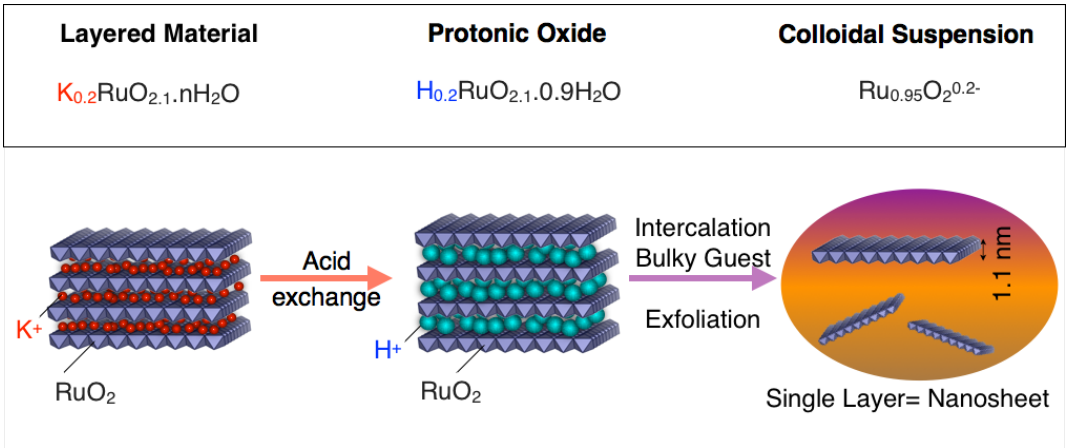

Figure 3.1. Soft-chemical exfoliation of layered $K_{0.2}RuO_{2.1}\cdot nH_2O$ to fabricate single layer $Ru_{0.95}O_2^{0.2-}$ nanosheets.

3.2.2. Fabrication of multilayer nanosheet capacitors

The surface profiles of $Ca_2NaNb_4O_{13}^-$ and $Ru_{0.95}O_2^{0.2-}$ nanosheets were evaluated by spreading the respective nanosheets on Si substrate. The loosely packed nanosheets were deposited via LB method through appropriate control of surface pressure during the lift-up process of substrate.[15,16] The morphology and height profiles of $Ca_2NaNb_4O_{13}^-$ and $Ru_{0.95}O_2^{0.2-}$ nanosheets were observed through taping mode AFM. The AFM images (Figure 3.2) confirm the sheets like morphology of both types of nanosheets and thickness of 2.05 ± 0.10 nm and 1.1 ± 0.10 nm corresponds to monolayers of $Ca_2NaNb_4O_{13}^-$ and $Ru_{0.95}O_2^{0.2-}$ nanosheets, respectively. These results confirmed the successful exfoliation of $Ca_2NaNb_4O_{13}^-$ and $Ru_{0.95}O_2^{0.2-}$ nanosheets. Moreover, it was observed that $Ca_2NaNb_4O_{13}^-$ nanosheets possess large lateral size > 10 μm, which will be effective for its

insulting properties due to less number of leakage boundaries/paths within the dielectric films.

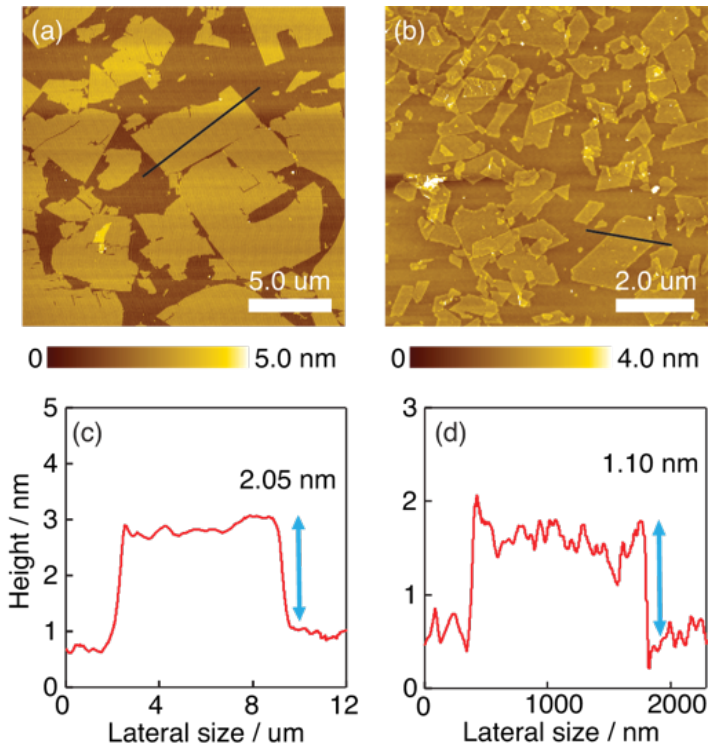

Figure 3.2. (a, c) AFM image and height profile of $Ca_2NaNb_4O_{13}^-$ nanosheets. **(b, c)** AFM image and height profile of $Ru_{0.95}O_2^{0.2-}$ nanosheets.

The schematic illustration of multilayer nanosheets capacitors (MNCs) is given in Figure 3.3. The structure of MNCs consists of two dielectric films ($Ca_2NaNb_4O_{13}^-$ nanosheets) interspersed between electrode films ($Ru_{0.95}O_2^{0.2-}$ nanosheets). The fabrication of MNCs consists of two main steps (Figure 3.3). The first step involves the LB deposition of $Ru_{0.95}O_2^{0.2-}$ nanosheets on Si wafer and quartz substrate. The substrates were pre-cleaned by treatment with CH_3OH:HCl (1:1) solution followed by immersion in 18M H_2SO_4 solution for 30 min each. As it can be observed from π-A curve in Figure 3.4b, the optimum surface pressure for deposition of $Ru_{0.95}O_2^{0.2-}$ is 16 ± 0.5 mN/m. The diluted suspension (48 mg/dm^3) of $Ru_{0.95}O_2^{0.2-}$ nanosheets is spread in LB trough and wait for 5 min before the barriers were moved inward at a speed of 0.5 mm s^{-1} to achieve desired 16 ± 0.5 mN/m surface pressure. After desired surface pressure was maintained, it

was maintained for 10 min to achieve high surface stability of floating nanosheets followed by lift-up process of substrate at 0.0167 mm s^{-1}. The monolayer film deposited on Si wafer and quartz glass was washed with excess of Milli-Q water, dried at 110 ^{o}C for 10 min followed by UV-irradiation under Xe lamp (1 mW cm^{-2}) for 10 min. LB deposition is repeated *n* number of times to achieve required thickness of electrode film.

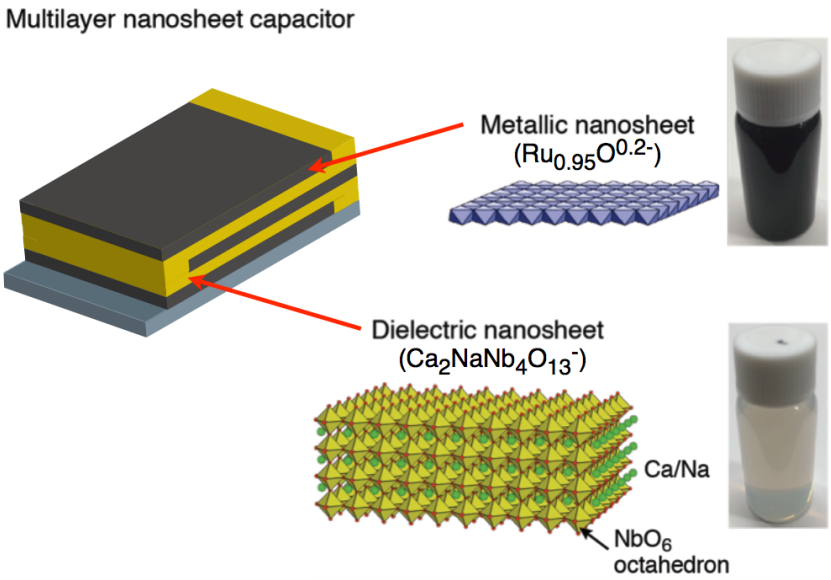

Figure 3.3. Schematic illustration for multilayer nanosheet capacitor of metallic $Ru_{0.95}O_2^{0.2-}$ and dielectric $Ca_2NaNb_4O_{13}^-$ nanosheets.

The second step addresses the deposition of high-*k* $Ca_2NaNb_4O_{13}^-$ nanosheets as dielectric film via LB method (Figure 3.4a). The optimum surface pressure was examined with the help of π-A isotherms and applied to achieve monolayer films of densely packed $Ca_2NaNb_4O_{13}^-$ nanosheet. The π-A isotherms in Figure 3.4b revealed an optimum surface pressure of 15 ± 0.5 mN/m. The colloidal suspension of $Ca_2NaNb_4O_{13}^-$ nanosheets was diluted up to 108 mg dm^{-3} and poured in LB trough. Diluted $Ca_2NaNb_4O_{13}^-$ nanosheets suspension was stabilized for 5 min and then barriers were allowed to move inward at 0.5 mm s^{-1}. $Ca_2NaNb_4O_{13}^-$ nanosheets were stabilized at air/water interface by the presence of tetrabutyl ammonium cations for 5 min and then densely packed monolayer films of $Ca_2NaNb_4O_{13}^-$ nanosheets was transferred during substrate lift-up procedure. A thorough washing of substrates was carried out to remove access TBA^+ ions

present on the surface of the film following by heat treatment at 110 ^{o}C for 10 min and UV irradiation by Xe lamp for 10 min. The monolayer films were transferred *n* number of times to achieve the required film thickness. Figure 3.4c demonstrate the UV-visible absorption spectra for 5-layer films of $Ca_2NaNb_4O_{13}^-$ and $Ru_{0.95}O_2^{0.2-}$ nanosheets on separate quartz substrates.

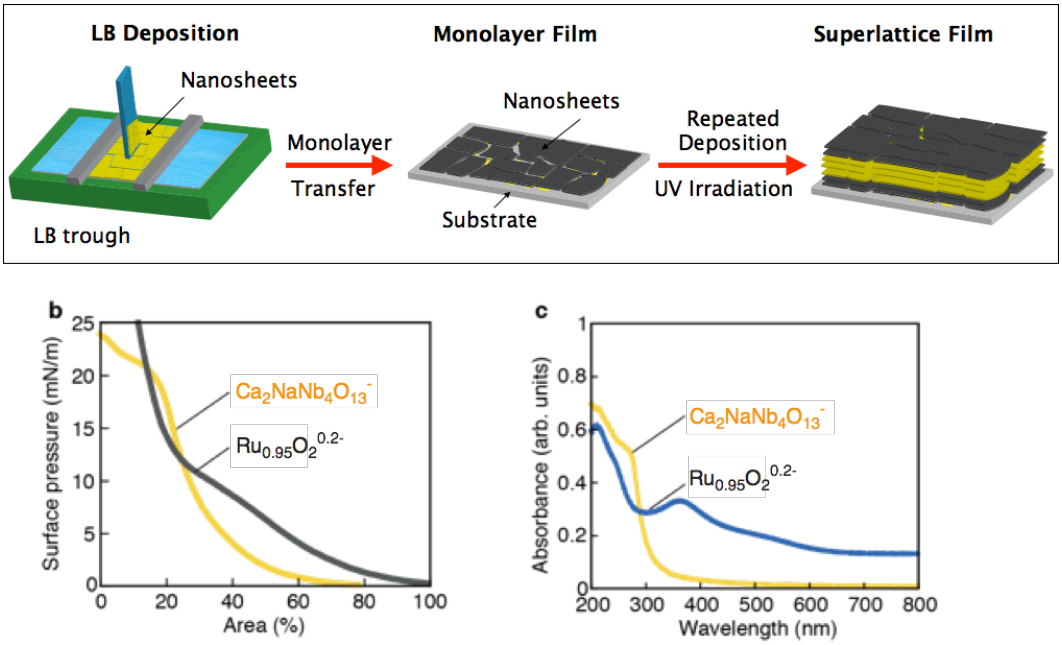

Figure 3.4. (a) Schematic illustration for fabricating multilayer nanosheet capacitors using LB technique. **(b)** Pressure-area (π-A) isotherms for nanosheet suspensions ($Ru_{0.95}O_2^{0.2-}$ and $Ca_2NaNb_4O_{13}^-$). **(c)** UV-visible spectra for the 5-layer films of $Ru_{0.95}O_2^{0.2-}$ and $Ca_2NaNb_4O_{13}^-$ nanosheets.

3.2.3. Characterization

I observed UV-visible absorption spectra exploiting Hitachi U-4100 spectrophotometer in transmission mode. Surface profiles of nanosheets films were recorded via SII Nanotechnology E-sweep AFM. The lamellar structure of the films was studied via cross-sectional HRTEM using Hitachi H-9000 microscope with point resolution of 0.1 nm and operated at 200 kV.

Au contacts were deposited on MNC devices with the use of metal mask through electron beam evaporation. Electrical properties were measured from

ambient temperature to 250 °C in a probe-station. Leakage current characteristics (*J–V*) were realized with semiconductor parameter analyzer (Keithley 4200-SCS). The capacitance density and dielectric loss were examined via precision impedance analyzer (Agilent Technologies 4294A) in the range of 1 kHz – 1 MHz.

3.3. Results and Discussion

3.3.1. Characterization of all-nanosheet capacitors

AFM observations (Figure 3.5 a, b) are evidence of neatly tiled monolayers of $Ru_{0.95}O_2^{0.2-}$ and $Ca_2NaNb_4O_{13}^-$ nanosheets deposited on Si substrates via above-mentioned procedures.[13] The monolayer films comprised of $Ru_{0.95}O_2^{0.2-}$ and $Ca_2NaNb_4O_{13}^-$ nanosheets exhibited ~95% of broad surface coverage of substrates with minimum number of gaps and overlaps. Monolayer films were observed to be atomically flat with average surface roughness of ~ 0.3 nm. The flat surfaces of $Ru_{0.95}O_2^{0.2-}$ nanosheets with highly conducting properties are favorable for deposition of highly packed $Ca_2NaNb_4O_{13}^-$ nanosheet films.

The LbL assembly process of $Ru_{0.95}O_2^{0.2-}$ and $Ca_2NaNb_4O_{13}^-$ nanosheets was monitored via UV-visible spectroscopy for two different sequences (Figure 3.5c, d) on quartz glass substrates. Each spectral line is representation of absorption shown by monolayer of either $Ru_{0.95}O_2^{0.2-}$ or $Ca_2NaNb_4O_{13}^-$ nanosheets. A regular increase in absorbance with each deposition cycle is evidence of successful transfer of high quality monolayer during MNC build up process. Blue and yellow lines represent the absorption spectra of monolayer layer of $Ru_{0.95}O_2^{0.2-}$ and $Ca_2NaNb_4O_{13}^-$ nanosheets, respectively.

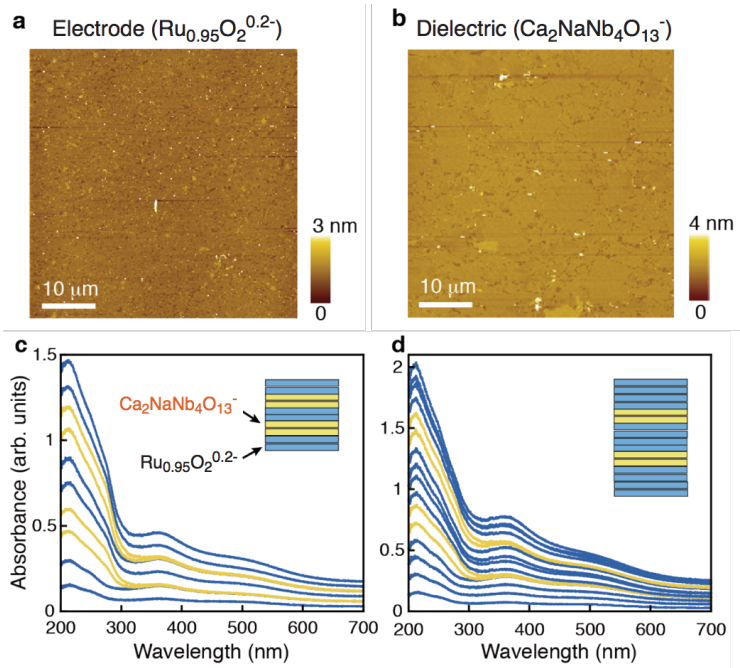

Figure 3.5. (a, b) AFM images of monolayer of **(a)** $Ru_{0.95}O_2^{0.2-}$ and **(b)** $Ca_2NaNb_4O_{13}^-$ nanosheets on Si substrates. **(c, d)** UV-visible absorption spectra of two different sequences **(c)** $[(Ru_{0.95}O_2^{0.2-})_2/(Ca_2NaNb_4O_{13}^-)_2]_2/(Ru_{0.95}O_2^{0.2-})_2$, $[(R_2/C_2)_2/R_2]$ and **(d)** $[(Ru_{0.95}O_2^{0.2-})_4/(Ca_2NaNb_4O_{13}^-)_2]_2/(Ru_{0.95}O_2^{0.2-})_4$, $[(R_4/C_2)_2/R_4]$.

A photograph (Figure 3.6a) of MNC fabricated on quartz glass exhibited a visibly transparent profile because of molecular thickness and low absorption of $Ru_{0.95}O_2^{0.2-}$ and $Ca_2NaNb_4O_{13}^-$ nanosheets in visible spectrum. Cross-sectional HRTEM image (Figure 3.6b) of MNC structure demonstrated that film coverage and thickness were uniform over a wide area. The dielectric layers were dense and gap free, covering the $Ru_{0.95}O_2^{0.2-}$ electrode in smooth, nearly conformal layers. The thickness of each $Ca_2NaNb_4O_{13}^-$ nanosheets layer was observed as 2.0 nm, which is in close resemblance with crystallographic thickness of 1.9 nm. The thickness of each dielectric layers ~ 4 nm corresponds two layers of $Ca_2NaNb_4O_{13}^-$ film as observed in Figure 3.7c. However, the lamellar structure of $Ru_{0.95}O_2^{0.2-}$ nanosheets (Figure 3.6c) was not visible, possibly due to more thinner and flexible profile and/or being susceptible to electron beam.[17] However, the thickness of $Ru_{0.95}O_2^{0.2-}$ electrode layers ~4 nm was consistent with 4 layers films of $Ru_{0.95}O_2^{0.2-}$ nanosheets. There was no detectable stacking defects between

electrode and dielectric layers was observe which is clear evidence of high quality stacking of dielectric and electrode layers in MNCs. The cross-sectional EDS elemental analysis Ru-*L* and Nb-*L* edge spectra clearly resolved the $Ru_{0.95}O_2^{0.2-}$ electrodes and dielectric $Ca_2NaNb_4O_{13}^-$ layers.

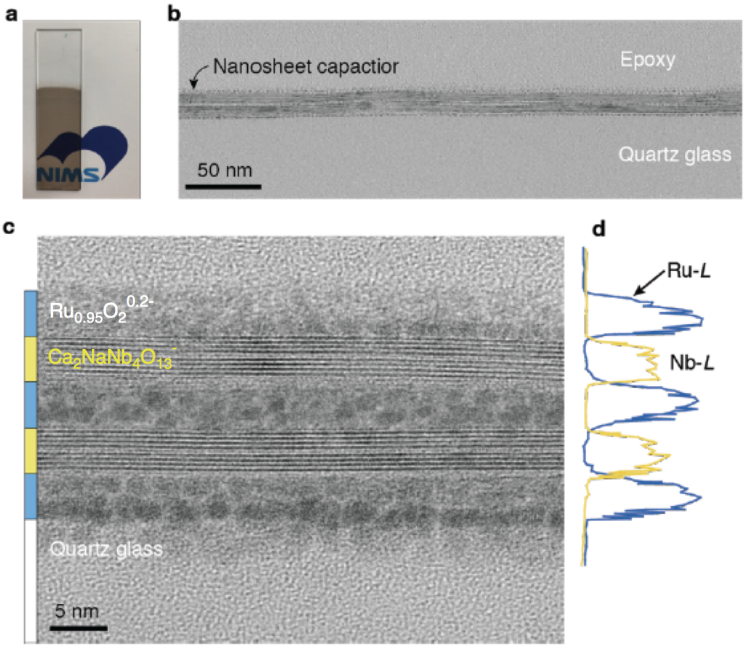

Figure 3.6. (a) Photograph of the MNC $[(R_4/C_2)_2/R_4]$ on a quartz glass substrate (10 x 50 mm^2). **(b, c)** Wide view and high magnification of cross sectional HRTEM images of the MNC $[(R_4/C_2)_2/R_4]$. **(d)** EDS analysis of the cross section.

3.2.2. Dielectric properties of all-nanosheet capacitors

I first investigated insulting properties of MNCs with different number of dielectric layers. MNC devices are fabricated on quartz glass substrate (5 x 10 mm^2) and Au contacts were fabricated using metal mask by electron beam evaporation (Figure 3.7a, b). Figure 3.7c illustrates leakage current density (*J-V*) profiles for three MNCs designs. It was assumed that leakage current density in all MNCs was governed by Schottky-type barrier at the interface between $Ca_2NaNb_4O_{13}^-$ and $Ru_{0.95}O_2^{0.2-}$ layers. $Ca_2NaNb_4O_{13}^-$ nanosheets possess large band gap of ~ 3.5eV form a large barrier height of ~ 1.6 eV with high work function (> 5 eV) $Ru_{0.95}O_2^{0.2-}$ nanosheets. Schottky-type barrier effectively blocks the passage

of charge carriers across the dielectric layers. As a result, all of the devices demonstrate highly insulting properties below 10^{-6} A/cm at +1V. However, insulting profiles are also dependent on number of dielectric layers in each dielectric film. There exists an inverse relation between the number of dielectric layers and leakage current density; larger the number of dielectric layers, smaller is leakage current density (Figure 3.7b). Such insulating behavior can be associated to barrier effects in the multilayer films. As a result, greater number of dielectric layers and interfaces could result in larger barriers leading to improvement in insulting properties.[18]

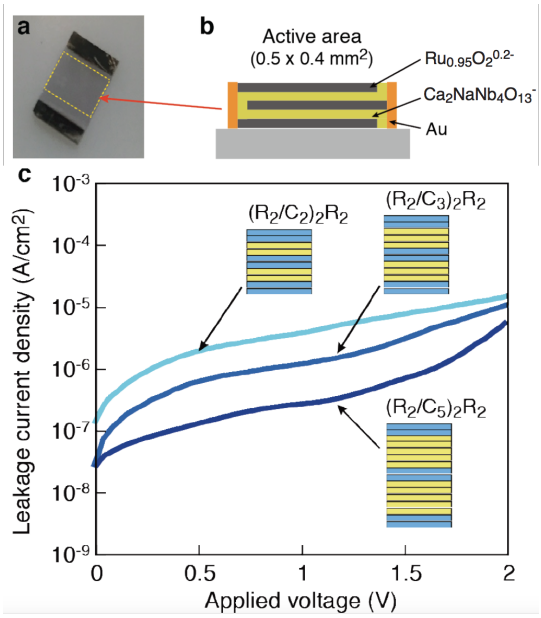

Figure 3.7. (a, b) Photograph and structure of the MNC $[(R_2/C_3)_2/R_2]$ on a quartz glass substrate (5 x 10 mm^2). **(c)** Leakage current density for the MNC devices with different $Ca_2NaNb_4O_{13}^-$ dielectric layers.

The capacitance response of MNCs was observed over a frequency range of 1 kHz to 1 MHz. As displayed in Figure 3.8a, MNCs with variable sequences demonstrated fairly stable frequency dispersion in the range of 1 kHz to 1 MHz. A well-known expression to demonstrate the capacitance of parallel plate capacitor can be written as:

$$C = \varepsilon_r \varepsilon_0 A/d$$

where C demonstrates capacitance density, ε_r expresses dielectric constant of material, ε_0 denotes permittivity of free space, A expresses electrode area and d

defines the thickness of dielectric material. MNCs device possess all the key parameters including high-*k* dielectric films, ultrathin dielectric films (smaller *d*), and large contact area between electrode and dielectric layers. Due to ultrathin thickness (~ 4nm) and high-*k* characteristics, MNC with two layers of $Ca_2NaNb_4O_{13}^-$ films exhibited highest capacitance density of ~52 $\mu F/cm^2$. According to above expression, if the thickness of dielectric film (*d*) is increased, the capacitance density should decrease due to inverse relationship only when the dielectric film has intrinsic property of no degraded capacitance response at lower thicknesses. As multilayer films of $Ca_2NaNb_4O_{13}^-$ nanosheets show no thickness dependent degradation in their dielectric properties (< 10 nm),[12] MNC devices with decreasing number of layers of $Ca_2NaNb_4O_{13}^-$ from 5 to 2, resulted in increase in capacitance density.

Moreover, thickness of the $Ca_2NaNb_4O_{13}^-$ layers also has effect on dielectric properties of MNC devices. Due to comparatively higher leakage exhibited by MNC device with two layers of $Ca_2NaNb_4O_{13}^-$ nanosheet films resulted in decrease in dielectric response (~ 162). However, MNC device with 3 layers of $Ca_2NaNb_4O_{13}^-$ nanosheets is effective enough to realize high-*k* dielectric response of ~ 192. However this value is considerably smaller than dielectric response exhibited by multilayer film of $Ca_2NaNb_4O_{13}^-$ nanosheets fabricated on atomically flat $SrRuO_3$ substrate. In case of $SrRuO_3$ as bottom electrode, the presence of atomically flat surfaces allowed for densely packed dielectric layers responsible for superior dielectric and reduced leakage current density. In the current MNCs with dielectric films consisting of 3 and 5 layers of $Ca_2NaNb_4O_{13}^-$ nanosheets, the presence of $Ru_{0.95}O_2^{0.2-}$ electrodes can contribute to slightly higher surface roughness as a result lead to decreased dielectric response in these MNC devices (Figure 3.8b). The high temperature capacitance response of MNCs is discussed in Chapter 4.

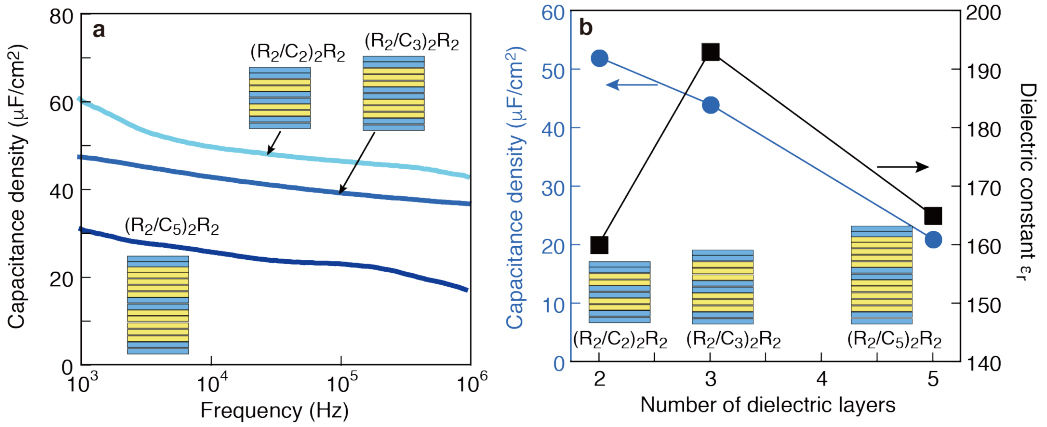

Figure 3.8. (a) Frequency dependence of the capacitances for the MNC devices with different $Ca_2NaNb_4O_{13}^-$ dielectric layers. **(b)** Effect of dielectric layer thickness on capacitance density and dielectric constant in the MNC devices.

In order to further justify the effect of surface roughness provided by $Ru_{0.95}O_2^{0.2-}$ electrode, MNC device was fabricated in which $Ru_{0.95}O_2^{0.2-}$ nanosheets have been deposited by sequential adsorption method. In case of sequential adsorption method, the surface of substrate is made positively charge by adsorption of polycations followed by excessive washing and then immersing the substrate in $Ru_{0.95}O_2^{0.2-}$ nanosheets suspension. Such monolayer films of $Ru_{0.95}O_2^{0.2-}$ nanosheets possess an average roughness of ~1.1 nm which is comparatively larger than $Ru_{0.95}O_2^{0.2-}$ monolayer film fabricated through LB method (roughness, ~ 0.3 nm). The higher surface roughness of film fabricated via sequential adsorption method can be associated to presence large number of overlaps and gaps. This effect is presented in Figure 3.9a, where two different types of $[(R_2/C_2)_2/R_2]$ MNC devices have been compared. In first $[(R_2/C_2)_2/R_2]$ MNC device all the dielectric and electrode layers have been deposited via LB method and in second $[(R_2/C_2)_2/R_2]$ MNC device, electrode layers are deposited via LbL sequential adsorption method (red square). Due to high surface roughness presented by sequential adsorption method, the resulting device exhibited higher leakage current density due to imperfect deposition of dielectric film. Furthermore, as the number of layers of $Ru_{0.95}O_2^{0.2-}$ nanosheets increased from 2 layers to 4 layers, it also resulted in increased leakage current density due to higher surface roughness possessed by larger number of layers.

Figure 3.9b demonstrate the effect of number of layers of $Ca_2NaNb_4O_{13}^-$ nanosheets in MNC devices. As the number of dielectric layers increase, the leakage current density is decreased due to barrier effect presented by larger number of dielectric layers and interfaces and hence effectively reduced the passage of charge carriers across the dielectric layers leading to highly insulating properties.

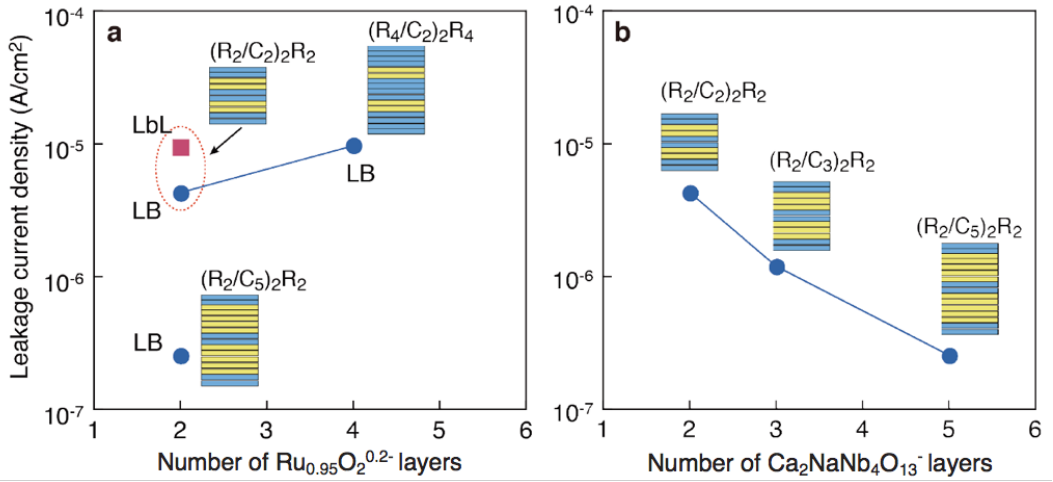

Figure 3.9. (a) Correlation between the leakage current density and the number of $Ru_{0.95}O_2^{0.2-}$ electrode layers in the MNCs. **(b)** Correlation between the leakage current density and the number of $Ca_2NaNb_4O_{13}^-$ dielectric layers in the MNCs.

These results indicate that $Ca_2NaNb_4O_{13}^-$ and $Ru_{0.95}O_2^{0.2-}$ nanosheets are potential candidate for ultrathin assembly of dielectric and electrode layers to built MNC devices, respectively. The molecular thickness of $Ca_2NaNb_4O_{13}^-$ nanosheets with high-*k* properties is an intriguing feature to realize high capacitance densities even at thickness < 10 nm. An important feature of solution-based assembly process via LbL fabrication of $Ca_2NaNb_4O_{13}^-$ and $Ru_{0.95}O_2^{0.2-}$ films is to have clean interfaces with no strain effects and interdiffusion of adjacent layers. Due to large band gap of ~ 3.5 eV, and highly insulating nature of $Ca_2NaNb_4O_{13}^-$ nanosheets contributed by flaw concentration effect due to thinner dielectric profile and additional advantage of large lateral size produce a synergistic effect to realize highly insulating properties. Furthermore, the Schottky-type contact between n-type $Ca_2NaNb_4O_{13}^-$ nanosheets and high work function $Ru_{0.95}O_2^{0.2-}$

nanosheets result in formation of large barrier height for holes and electrons, as a result effectively blocks charge carrier transfer across the dielectric layer. In contrast to this $BaTiO_3$ and $Ba_xSr_{1-x}TiO_3$, which are common dielectric materials for capacitor application suffer from many limitations when their size is reduced down to few 10n of nm. [19-21] This size-dependent effect suppresses the dielectric response and raises leakage current profile. Particularly, when the thickness of high-*k* material such as $Ba_xSr_{1-x}TiO_3$ is decreased down to few 10s nm, the effect of interfacial layer become significant. Usually during the heating process, a low-*k* dead layer is produced at the interface between substrate and dielectric films and hence degrade the dielectric response of the films. In this context, dielectric films comprised of $Ca_2NaNb_4O_{13}^-$ nanosheets possess unique characteristics discussed above and are potential materials for ultrathin design of novel nanodevices.

3.4. Summary

I have successfully demonstrated the fabrication of ultrathin MNCs with high capacitance density using iterative LB method for deposition of dielectric layers of $Ca_2NaNb_4O_{13}^-$ and electrodes layers of $Ru_{0.95}O_2^{0.2-}$ nanosheets. The lamellar structure of MNCs was investigated with HRTEM. The cross-sectional HRTEM image confirmed the uniform and homogenous coverage of glass substrate with nanosheets film. By changing the sequences for the deposition of $Ca_2NaNb_4O_{13}^-$ nanosheets and $Ru_{0.95}O_2^{0.2-}$ nanosheets, it is possible to fabricated different MNC devices and investigated the effect of number of layers of $Ca_2NaNb_4O_{13}^-$ and $Ru_{0.95}O_2^{0.2-}$ nanosheets on the dielectric and leakage current density of the various devices. It was observed that MNCs with two perovskite layers of $Ca_2NaNb_4O_{13}^-$ nanosheets exhibited highest capacitance density of ~ 52 μF/cm and low leakage current density below 10^{-6} A/cm at +1V. However, as the thickness of dielectric film is increased, it resulted in decrease of capacitance density because of inverse relationship between capacitance and thickness of dielectric films according to parallel capacitor formula, However, this response is observed only when the dielectric film has intrinsic property of no degraded capacitance response at lower thicknesses, which is unique feature of perovskite $Ca_2NaNb_4O_{13}^-$ nanosheets.

Although, MNC devices with larger number of layers of $Ca_2NaNb_4O_{13}^-$ nanosheets exhibited superior leakage current density due to barrier effect offer by large number of dielectric layers and interfaces. Furthermore, it was also observed that there exist significant effects of surface roughness of bottom electrode layers on the leakage current density. MNC devices with larger number of $Ru_{0.95}O_2^{0.2-}$ layers or $Ru_{0.95}O_2^{0.2-}$ layers fabricated via electrostatic sequential adsorption method demonstrated higher leakage current density due to higher surface roughness. It is concluded that $Ca_2NaNb_4O_{13}^-$ nanosheets based MNCs performed better than commercially available MLCCs at comparable thicknesses. The fabrication design of MNC devices is observed to be simple, low cost and environmentally friendly room temperature solution process.

3.5. References

1. M. J. Pan, C. A. Randall, *IEEE Elect. Insul. Mag.* **26**, 44 (2010).
2. H. Kishi, Y. Mizuno, H. Chazono, *Jpn. J. Appl. Phys.* **42**, 1 (2003).
3. H. Nagata, S. W. Ko, E. Hong, C. A. Randall, S. T. McKinstry, P. Pinceloup, D. Skamser, M. Randall, A. Tajuddin, *J Am. Ceram. Soc.* **89**, 2816 (2006).
4. A. V. Polotai, I. Fujii, D. P. Shay, G. Yang, E. C. Dickey, C. A. Randall, *J. Am. Ceram. Soc.* **91**, 2540 (2008).
5. J. Y. Lee, J. H. Lee, S. H. Hong, Y. K. Lee, J. Y. Choi, *Adv. Mater.* **15**, 1655 (2003).
6. G. Y. Yang, S. I. Lee, Z. J. Liu, C. J. Anthony, E. C. Dickey, Z. K. Liu, C. A. Randall, *Acta Mater.* **54**, 3513 (2006).
7. T. Dechakupt, G. Yang, C. A. Randall, S. T. McKinstry, I. M. Reaney, *J. Am. Ceram. Soc.* **91**, 1845 (2008).
8. K. Binder, *Ferroelectrics*, **73**, 43 (1987).
9. T. Tsurumi, T. Hoshina, H. Takeda, Y. Mizuno, H. Chazono, *IEEE Trans. Ultrason. Ferroelectr. Freq. Control*, **56**, 1513 (2009).
10. C. A. Randall, *J. Ceram. Soc. Jpn.* **109**, 2 (2001).
11. A. V. Polotai, G. Yang, E. C.Dickey, C. A. Randall, *J. Am. Ceram. Soc.* **90**, 3811 (2007).
12. B. W. Li, M. Osada, Y. -H Kim, Y. Ebina, K. Akatsuka, T. Sasaki, *J. Am. Chem. Soc.* **139**, 10868 (2017).
13. C. Wang, M. Osada, Y. Ebina, B. W. Li, K. Akatsuka, K. Fukuda, W. Sugimoto, R. Ma, T. Sasaki, *ACS Nano* **8**, 2658 (2014).
14. Y. Ebina, K. Akatsuka, K. Fukuda, T. Sasaki, *Chem. Mater.* **24**, 4201 (2012).
15. M. Osada, K. Akatsuka, Y. Ebina, H. Funakubo, K. Ono, K. Takada, T. Sasaki, *ACS Nano* **4**, 5225 (2010).
16. J. Sato, H. Kato, M. Kimura, K. Fukuda, W. Sugimoto, *Langmuir* **26**, 18049 (2010).
17. Y. C. Lin, R. K. Ghosh, R. Addou, N. Lu, S. M. Eichfeld, H. Zhu, M. -Y. Li, X. Peng, M. J. Kim, L. J. Li, R. M. Wallace, S. Datta, J. A. Robinson, *Nat. Commun*. **6**, 7311 (2015).
18. M. Mackey, D. E. Schuele, L. Zhu, E. Baer, *J. Appl. Phys.* **111**, 113702 (2012).

19. C. S. Hwang, S. O. Park, H. J. Cho, C. S. Kang, H. K. Kang, S. I. Lee, M. Y. Lee, *Appl. Phys. Lett.* **67**, 2819 (1995).
20. P. Padmini, T. R. Taylor, M. J. Lefevre, A. S. Nagra, R. A. York, J. S. Speck, *Appl. Phys. Lett.* **75**, 3186 (1999).
21. C. S. Hwang, J. Appl. Phys. **92**, 432 (2002).
22. K. Frohlich, J. Aarik, M. Tapajna, A. Rosova, A. Aidla, E. Dobrocka, K. Huskova, *J. Vac. Sci. Technol. B* **27**, 266 (2009).

Chapter 4

High-Temperature Dielectric Responses of Ultrathin Nanosheets Capacitors

4.1. Introduction

Capacitors are important components of electronic devices. Their major responsibilities are to perform variety of functions including voltage smoothing, pulse discharge, filtering, coupling and decoupling, dc blocking, snubbing and power conditioning. With the increasing demands for multifunctional electronic devices, the requirements for capacitor materials are also getting more complex. In this regard, high-temperature electronic devices are quite important as these units are to be placed close to engines and transmissions. Such a design provides the advantage of simplification of assembly of overall product such as automobiles. For the purpose of miniaturization, cost reduction and lighter in weight, high temperature electronic devices are needed for various applications including automotive, aerospace and defense technologies.[1-3]

In all high-temperature applications, the electronic devices are required to operate under harsh conditions while demonstrating decent electrical characteristics and high reliability at high-temperatures above 200 ^{o}C. The most challenging components among required passive devices are capacitors. A capacitor must exhibit relatively stable capacitance over the whole operational range. Usually, high permittivity is required to achieve high capacitances needed for power conditioning circuits. The dielectric with low volumetric efficiency usually lead to large capacitor sizes and therefore ill-suited for system miniaturization and can also face failure due to thermal stresses. A capacitor must exhibit high resistivity and low losses at elevated temperatures. Moreover, it is required to express low frequency dispersion of capacitance and low loss factor.

$BaTiO_3$ is an important ferroelectric material, which demonstrates high-*k* dielectric response at room temperature. However, $BaTiO_3$ based capacitor are not suitable for high-temperature applications due to relatively low Curie Temperature (T_C) of 120 ^{o}C.[4] As the temperature is raised above T_C, a severe degradation in dielectric properties is experienced due to phase transition from tetragonal to cubic phase. Figure 4.1 gives an overview of the dielectric permittivity variation as a function of temperature. At high-temperatures, $BaTiO_3$ exhibit paraelectric cubic phase. As the temperature is decreased, $BaTiO_3$ demonstrate three sequential phase transitions with tetragonal, orthorhombic and rhombohedral symmetries at 393,

273, and 183 *K*, respectively.[5] The maximum permittivity is observed at T_C. However, it is important that a capacitor must demonstrate relatively stable dielectric response over operational range of temperature.

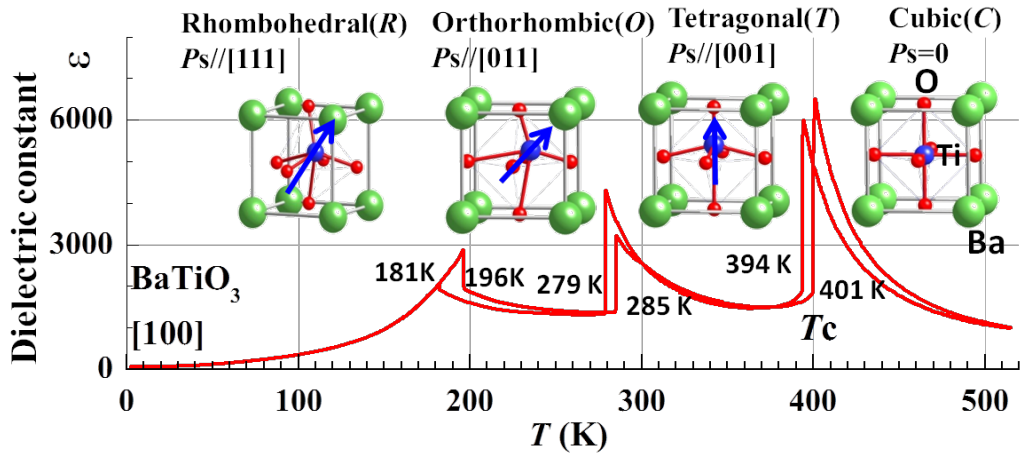

Figure 4.1. Dielectric response of $BaTiO_3$ as function of temperature. Adapted with permission.[5] Copyright 2015, InTech.

In this context, extensive research has been carried out to increase the phase transition temperature and decrease the temperature dependent fluctuations in the dielectric constant of $BaTiO_3$. Important strategies to modify the dielectric responses include doping with rare earth metals and/or forming solid solutions with metal oxides. However, thin films of modified composition of $BaTiO_3$ often demonstrate few orders decreased ε_r response as compared to bulk values (Figure 4.2). Moreover, thin films of $(Ba,Sr)TiO_3$ result in enhanced dielectric loss and leakage profiles. [6-8]

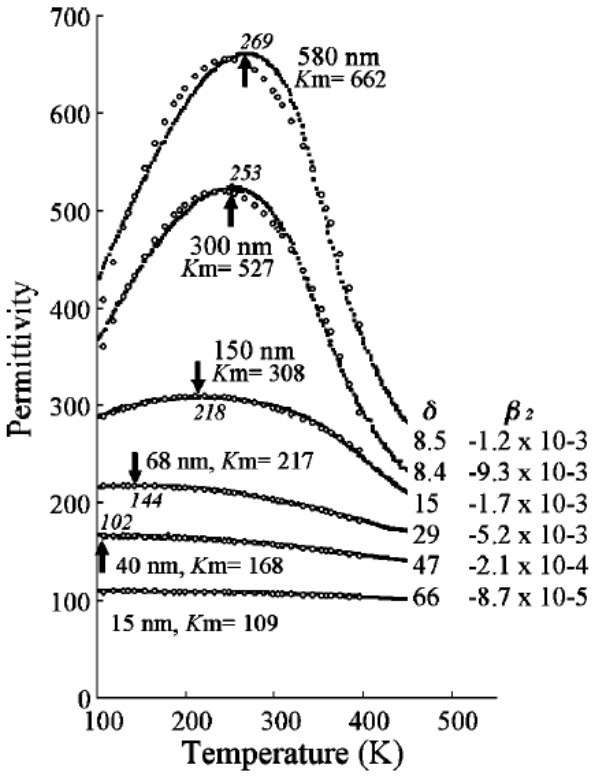

Figure 4.2. Permittivity as function of temperature for different thicknesses. Adapted with permission.[7] Copyright 2002, AIP Publishing LLC.

Another important class of materials is simple oxides such as TiO_2, HfO_2, and Al_2O_3, which exhibit temperature independent dielectric responses, suitable for high-temperature applications. However, these materials are paraelectric in nature and hence posses lower ε_r (< 100) and can not be treated as important candidate for high-temperature applications.[9-11] Furthermore, relaxor dielectrics are also important materials with relatively large dielectric constants. $Pb(Mg_{1/3}Nb_{2/3})O_3$ is a typical relaxor dielectric that possess high-*k* values in the range of ~20,000. However, toxicity of Pb is an environmental issue for such materials and its volatility at high sintering temperature at 1200 ^oC presents a processing drawback.[12] Hence, the focus of today's research is to improve the existing materials and/or develop new dielectric materials suitable for miniaturized electronic devices with high-temperature applications and demonstrating temperature independent high-*k* response, lower loss (tan δ) and reduced leakage (J).[13,14]

$Ca_2Nb_3O_{10}^-$ and $Ca_2NaNb_4O_{13}^-$ nanosheets are 2D single crystals with a thickness of 1.55 ± 0.10 nm and 2.05 ± 0.10 nm, which corresponds to three and four NbO_6 octahedra along the block normal, respectively.[15] Exfoliated nanosheets contains key blocks of their respective layered materials and are restacked to realize high-*k* properties at critical thickness. Li *et al.* reported that multilayer films of $Ca_2Nb_3O_{10}^-$ and $Ca_2NaNb_4O_{13}^-$ nanosheets has realized highest permittivity of ~210 and ~290, respectively, which is quite high as compared to all known perovskite in ultrathin region (< 10 nm).[16] Wang *et al.* presented multilayer films of $Ca_2Nb_3O_{10}^-$ nanosheets as dielectric layers sandwiched between electrode $Ru_{0.95}O_2^{0.2-}$ layers. Such metal-insulator-metal structure was observed to demonstrate high capacitance density of 27.5 $\mu F/cm^3$ with the ultrathin thickness of 28 nm.[17] Le *et al.* investigated an important feature of $Ca_2Nb_3O_{10}^-$ nanosheets, which is its thermal stability. In-situ XRD study confirmed that monolayer films of $Ca_2Nb_3O_{10}^-$ nanosheets are stable up to 700 ^oC.[18] Thermal stability and high-*k* properties of $Ca_2Nb_3O_{10}^-$ nanosheets make it potential candidate for investigation of high-*k* material for elevated temperature applications. In this chapter, I will study the high-temperature response of $Ca_2NaNb_4O_{13}^-$ based multilayer nanosheets capacitor.

4.2. Experimental

4.2.1. Fabrication of nanosheet-based capacitors

The colloidal suspension of $Ca_2Nb_3O_{10}^-$ and $Ru_{0.95}O_2^{0.2-}$ were synthesized according to previously reported procedure.[19,20] The synthesis of $Ca_2Nb_3O_{10}^-$ nanosheets and $Ru_{0.95}O_2^{0.2-}$ nanosheets have been already explained in Chapter 2 and Chapter 3, respectively. Through AFM, the lateral sizes of $Ca_2Nb_3O_{10}^-$ and $Ru_{0.95}O_2^{0.2-}$ were observed as 5-7 μm and 1 μm, respectively. The LbL assembly $Ca_2Nb_3O_{10}^-$ and $RuO_2^{0.2-}$ was carried out via LB and sequential absorption procedure. In the typical procedure, all-nanosheets capacitor was fabricated on silicon substrate and quartz glass. The substrates were made hydrophilic by treating with CH_3OH/HCl (1:1) solution and 18M H_2SO_4 for 30 minutes each. Firstly, the cleaned substrates were dipped in polyvinyl amine/polyvinyl alcohol

solution (C-601) with 1 wt% concentration for 5 minutes to make positively charged surfaces. The substrates were washed with excess of milli-Q water to achieve monolayer films of polycations. Secondly, the substrates were dipped in diluted suspension of $Ru_{0.95}O_2^{0.2-}$ nanosheets (0.2 g/dm^3) for 15 minutes to achieve densely packed monolayer film.[17, 21] (C-601/$Ru_{0.95}O_2^{0.2-}$) steps were repeated to develop required electrode thickness.

Dielectric film consisting of $Ca_2Nb_3O_{10}^-$ nanosheets was fabricated through facile LbL assembly using LB technique.[22, 23] A diluted suspension of 96 mg/dm^3 of $Ca_2Nb_3O_{10}^-$ nanosheets was prepared and used as subphase for the transfer of each monolayer film. The surface pressure of floating $Ca_2Nb_3O_{10}^-$ nanosheets at air-water interface was monitored with the help of Wilhelmy-type balance. The packing density was controlled with the help of moveable barrier and surface pressure was adjusted at 15.5 ± 0.5 mN/m. After 5 min of wait after achieving optimum surface pressure, the immersed substrate is lifted up to achieve densely packed monolayer film of $Ca_2Nb_3O_{10}^-$ nanosheets. The substrates were washed vigorously with milli-Q water. Before the next deposition, substrates were dried at 110 ^oC for 10 min and kept under UV irradiation in Xe lamp to get the hydrophilic surfaces. The above procedure was repeated 10 times to fabricate multilayer film of $Ca_2Nb_3O_{10}^-$ nanosheets as dielectric film. Lastly, the top electrode consisting of $Ru_{0.95}O_2^{0.2-}$ nanosheets layers were fabricated in a similar way as bottom electrode. The as-fabricated all-nanosheets capacitors were exposed to UV light using a Xe lamp (4mW/cm^2) for 48 h to decompose TBAOH. Figure 4.3 demonstrates the schematic for the fabrication of all-nanosheets capacitor.

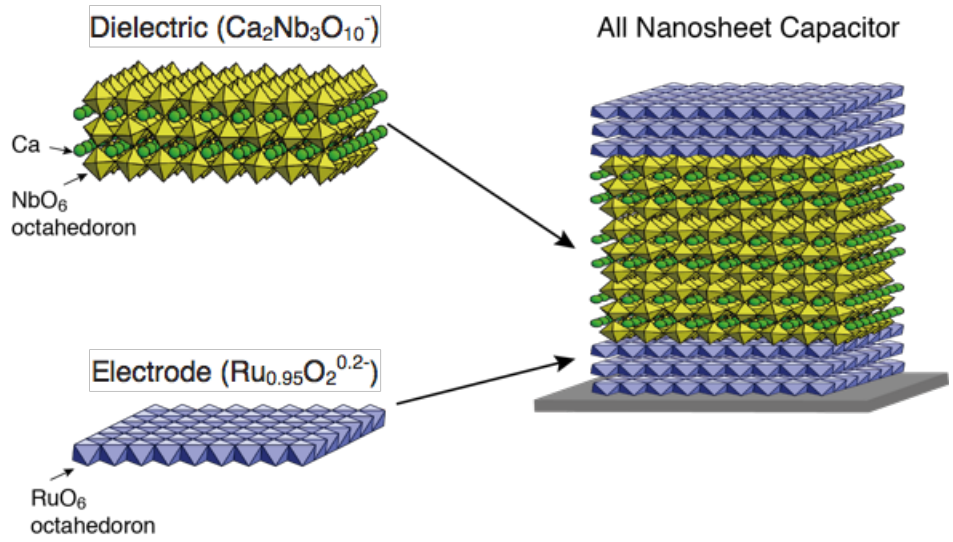

Figure 4.3. Schematic illustration for fabricating all nanosheet capacitor using high-*k* dielectric $Ca_2Nb_3O_{10}^-$ and conducting $Ru_{0.95}O_2^{0.2-}$ nanosheets.

4.2.2. Characterization

The lamellar structure of all-nanosheets capacitor was observed via cross-sectional HRTEM observation through Hitachi H-9000 microscope. High temperature dielectric properties (ε_r and *J*) were studied with the help of temperature variable microprobe station. Capacitance and leakage profiles of all-nanosheets capacitors were investigated with precision impedance analyzer (Agilent 4294A) and semiconductor parameter analyzer (Keithley 4200-SCS), respectively.

4.3. Results and Discussion

4.3.1. Characterization of $Ca_2Nb_3O_{10}^-$ -based capacitors

Figure 4.4 illustrates cross-sectional HRTEM image of all nanosheets capacitor, $[(Ru_{0.95}O_2^{0.2-})_5/(Ca_2Nb_3O_{10}^-)_{10}/(Ru_{0.95}O_2^{0.2-})_5]$, which possesses total thickness of 28 nm. It is confirmed form cross-sectional HRTEM that all nanosheets capacitor demonstrate a uniform coverage and thickness over a wide area. The lamellar structure of $Ca_2Nb_3O_{10}^-$ nanosheets film was evident and each

monolayer film can be visualized as three apex-sharing NbO_6 octahedra in form of three dark parallel fringes. Each monolayer of $Ca_2Nb_3O_{10}^-$ nanosheets has thickness of 1.45 nm, which is close to crystallographic thickness. The lamellar structure of $Ru_{0.95}O_2^{0.2-}$ nanosheets was not observed due to its thin and weak characteristics susceptible to electron beam.[17] Although, the thickness (5-6 nm) of each electrode was according to 5-layers of $Ru_{0.95}O_2^{0.2-}$ nanosheets. HRTEM images confirmed the presence of clean and sharp interface between $Ca_2Nb_3O_{10}^-$ and $Ru_{0.95}O_2^{0.2-}$ layers ruling out the possibility of interdiffusion and disorders at the interface.

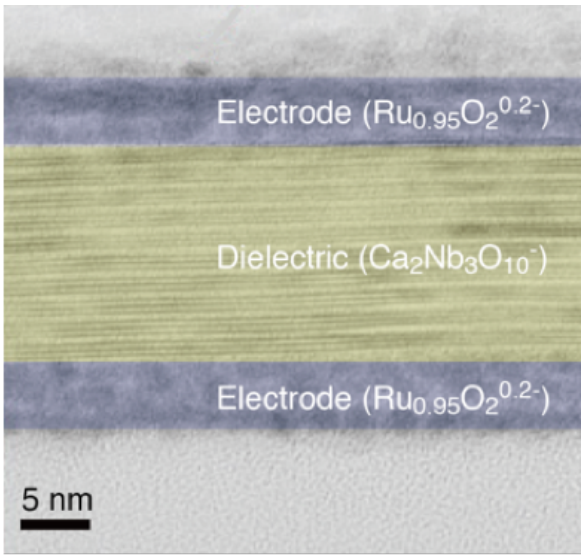

Figure 4.4. Cross-sectional HRTEM image of all nanosheet capacitor $(Ru_{0.95}O_2^{0.2-})_5/(Ca_2Nb_3O_{10}^-)_{10}/(Ru_{0.95}O_2^{0.2-})_5$ fabricated on a quartz substrate.

4.3.2. Dielectric properties of $Ca_2Nb_3O_{10}^-$-based capacitors

Dielectric response (Figure 4.5) with respect to electric field is given for all nanosheets capacitor along with $Ba_{1-x}Sr_xTiO_3$ capacitor (t ~ 24 nm) and $Au/(Ca_2Nb_3O_{10}^-)_{10}/SrRuO_3$ capacitor. All-nanosheets capacitor realized stable ε_r ~ 180 at zero applied field, which is relatively low as compared to $Au/(Ca_2Nb_3O_{10}^-)_{10}/SrRuO_3$ capacitor (ε_r ~ 210).[7,16,24] The decrease in dielectric response for all-nanosheets capacitor can be associated to surface roughness of bottom $Ru_{0.95}O_2^{0.2-}$ electrode that prevented from dense packing of dielectric layers and ultimately

affected the dielectric response. A linear hysteresis is signature of paraelectric nature of $Ca_2Nb_3O_{10}^-$ nanosheets with no substantial dependency on high electric field (2 MV/cm).[7,8] Where as, $Ba_{1-x}Sr_xTiO_3$ capacitor exhibited 50% loss up to 2 MV/cm.

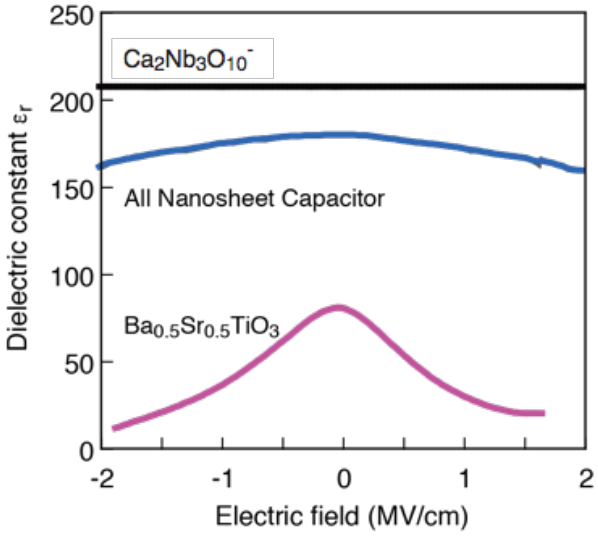

Figure 4.5. ε_r–V profiles for all nanosheet capacitor $(Ru_{0.95}O_2^{0.2-})_5/(Ca_2Nb_3O_{10}^-)_{10}/(Ru_{0.95}O_2^{0.2-})_5$, Au/$(Ca_2Nb_3O_{10}^-)_n$/$SrRuO_3$, and BST film at room temperature.

Figure 4.6 shows dielectric response with respect to frequency at variable temperatures for all nanosheets capacitors. At ambient condition (25 ^oC), all nanosheet capacitor exhibited stable ε_r of ~180 at 10 kHz. Between 1 kHz to 1 MHz, flat frequency dispersion was observed. A slight increase in dielectric response below 1 kHz can be associated to charge relaxation and interface polarization.[25, 26] At 200 ^oC, a relatively high ε_r value of ~155 was observed. A slight decline in ε_r value at elevated temperatures can be associated to imperfect polarization triggered by thermal energy. Moreover, at high frequency, scattered dipole could not proceed in case of high temperatures, resulting in decrease in dielectric behavior.

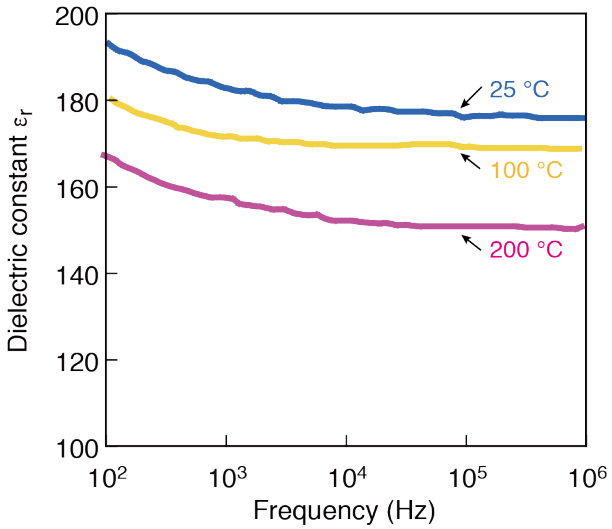

Figure 4.6. ε_r response as factor of frequency for all nanosheet capacitor $(Ru_{0.95}O_2^{0.2-})_5/(Ca_2Nb_3O_{10}^-)_{10}/(Ru_{0.95}O_2^{0.2-})_5$ at 25, 100, and 200°C.

Figure 4.7 demonstrates change in capacitance in response to change in temperature for various devices. All-nanosheets capacitors realized thermal stability in the range of 0-200 ^oC. The deviation in capacitance with respect to room temperature for all-nanosheets capacitors was observed as -12.5%. Whereas, $Ba_{1-x}Sr_xTiO_3$ capacitor exhibited a loss of -80% in capacitance at a comparable thickness.[7] Furthermore, all-nanosheets capacitors revealed higher capacitance deviation as compared to same $Ca_2Nb_3O_{10}^-$ on atomically flat $SrRuO_3$ substrate.

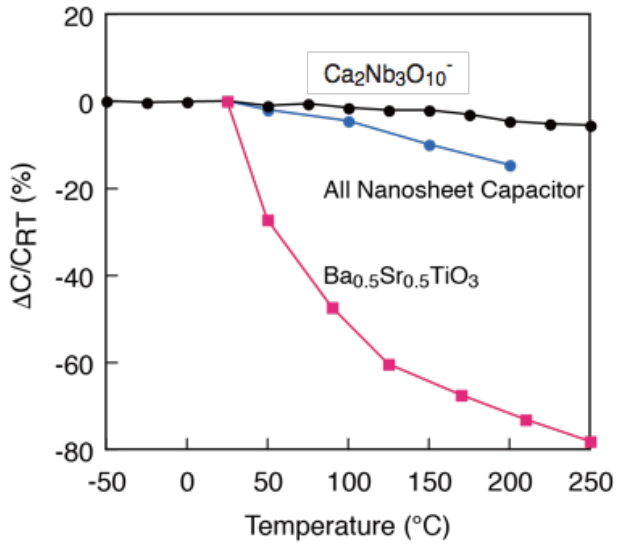

Figure 4.7. Temperature dependent capacitance response ($\Delta C/C_{RT}$) for all nanosheet capacitor, Au/$(Ca_2Nb_3O_{10}^-)_n$/$SrRuO_3$, and BST film.

Figure 4.8 reveals leakage profiles for all nanosheets capacitor with respect to applied voltages at different temperatures. At 25 ^oC, leakage current density was 10^{-6} A/cm^2 at +1V, which was relatively larger than 10^{-7} A/cm^2 observed for $Ca_2Nb_3O_{10}^-$ fabricated on $SrRuO_3$.[16, 24] This increased in leakage profile can be associated to presence of larger leakage path in all-nanosheets capacitor due to more surface roughness of bottom $Ru_{0.95}O_2^{0.2-}$ electrode. At high temperature, 200 ^oC, all nanosheets capacitor exhibited larger leakage profile of 10^{-5} A/cm^2 at +1 V. However, this value is still one order smaller in magnitude than that of $Ba_{1-x}Sr_xTiO_3$ capacitor. It is assumed that Schottky-type contact between electrode and dielectric layers is present where electrons flow from *n*-type $Ca_2Nb_3O_{10}^-$ nanosheets towards conducting $Ru_{0.95}O_2^{0.2-}$ nanosheets with high work function (> 5 eV). Moreover, due to quantum confinement effect, $Ca_2Nb_3O_{10}^-$ nanosheets possess larger band gap (~ 3.8 eV), as a result inhibit the passage of current in contrast to bulk.

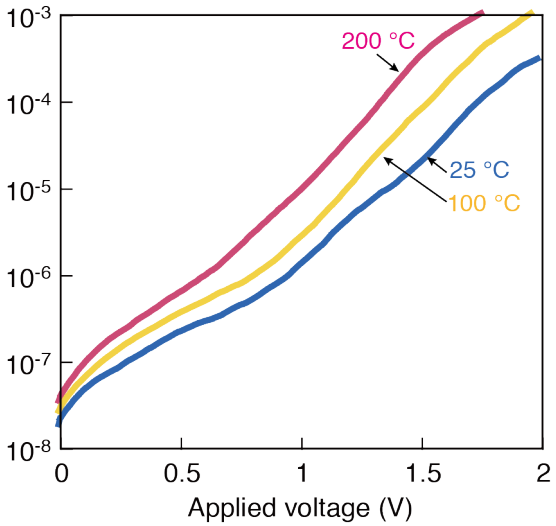

Figure 4.8. Leakage current *vs.* bias voltage (*J*-*V*) profiles of all nanosheet capacitor $(Ru_{0.95}O_2^{0.2-})_5/(Ca_2Nb_3O_{10}^-)_{10}/(Ru_{0.95}O_2^{0.2-})_5$ at 25, 100, and 200 °C.

4.3.3. Dielectric properties of $Ca_2NaNb_4O_{13}^-$-based capacitors

In this section, I explained the high-*k* properties of $Ca_2NaNb_4O_{13}^-$-based capacitors. As it can be observed (Figure 4.9) that capacitance density for the MNC $[(R_2/C_3)_2/R_2]$ (structure details in Chapter 3) exhibited a stable response as a function of applied voltage up to +4V. The *C*-*V* curve of MNC exhibited paraelectric nature without hysteresis. In contrast, MLCCs demonstrated larger dependence in capacitance (reduced by 80% up to +4V) as a function of applied voltage.

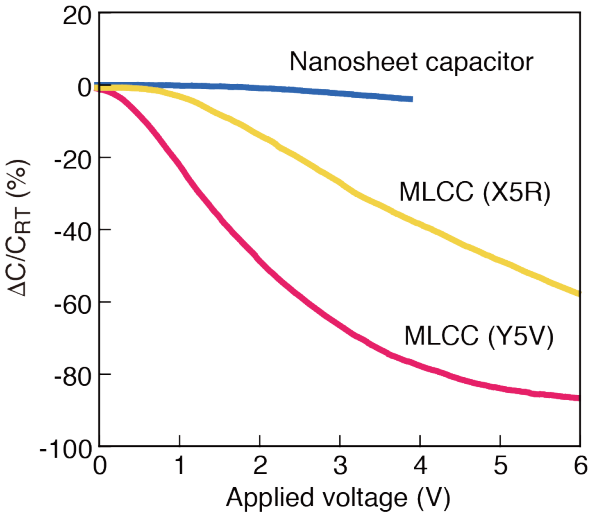

Figure 4.9. Electric-field dependence of the capacitance change for the MNC $[(R_2/C_3)_2/R_2]$ and MLCCs (X5R, Y5V).

Figure 4.10 demonstrates the change in capacitance with respect to temperature for MNC and various MLCC technologies. MNC realized stable capacitance response over a wide temperature range of -50 ~ 250 ^{o}C with small capacitance deviation of -5.5%. In contrast, various MLCCs exhibited degraded capacitance response as a function of temperature. I observed that nanosheets based capacitors with dielectric layers (< 10 nm) exhibited high-*k* properties and high insulating features at temperatures up to 250 °C. These features are signature of superior profile of multilayer nanosheets capacitors over existing MLCCs technologies such as X5R, Y5V, X8R, X9R.

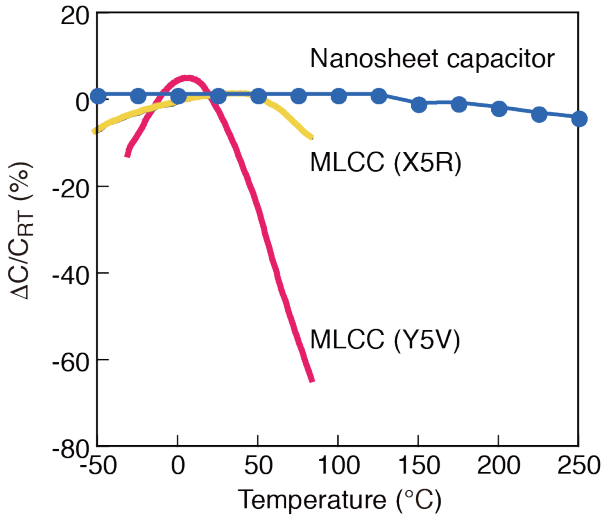

Figure 4.10. Temperature dependence of the capacitance change for the MNC $[(R_2/C_3)_2/R_2]$ and MLCCs (X5R, Y5V)

$Ca_2Nb_3O_{10}^-$ and $Ca_2NaNb_4O_{13}$-based nanosheets capacitor exhibited high-*k* properties for elevated temperatures. However, its was observed that in case of $Ca_2Nb_3O_{10}^-$ the dielectric constant and leakage current density were slightly dependent at high temperature and exhibited small decrease in the properties as the temperature was raised to 200 ^oC. The possible reason for decreased response can be associated to the higher surface roughness of the bottom $Ru_{0.95}O_2^{0.2-}$ nanosheets electrode fabricated via electrostatic sequential adsorption procedure which usually have surface roughness of 1.1 nm for each monolayer. Collectively, 5-layer film of bottom $Ru_{0.95}O_2^{0.2-}$ nanosheets has considerable effect on the packing density of afterward LbL assembled dielectric $Ca_2Nb_3O_{10}^-$ nanosheets layers. In case of $Ca_2NaNb_4O_{13}$-based nanosheets capacitor, a robust capacitance response was observed as function of high temperature and high voltages. The excellent capacitance properties of $Ca_2NaNb_4O_{13}$-based nanosheets capacitor can be associated to high quality films of $Ru_{0.95}O_2^{0.2-}$ nanosheets electrode fabricated via LB method with surface roughness of ~ 0.3 nm for each monolayer which is considerably small as compared to ~1.1 nm for $Ru_{0.95}O_2^{0.2-}$ nanosheets deposited via electrostatic sequential adsorption procedure. Secondly, the large lateral size of $Ca_2NaNb_4O_{13}$ nanosheets also contribute effectively to realized high voltage stability.

4.4. Summary

In this chapter, high temperature dielectric response of $Ca_2Nb_3O_{10}^-$ and $Ca_2NaNb_4O_{13}^-$ nanosheets based multilayer capacitors was investigated. $Ca_2Nb_3O_{10}^-$ nanosheets based all-nanosheets capacitors were successfully fabricated via electrostatic sequential adsorption of $Ru_{0.95}O_2^{0.2-}$ nanosheets and LB deposition of $Ca_2Nb_3O_{10}^-$ nanosheets to make metal-insulator-metal structure. The structure of resultant multilayer nanosheets capacitor, $(Ru_{0.95}O_2^{0.2-})_5/(Ca_2Nb_3O_{10}^-)_{10}/(Ru_{0.95}O_2^{0.2-})_5$, was evaluated with HRTEM. The cross-sectional HRTEM confirmed the metal-insulator-metal structure with clean interface. The nanosheets-based capacitor was uniformly present over substrate surface with no inter-diffusion. The lamellar structure of multilayers of $Ca_2Nb_3O_{10}^-$ nanosheets was visualized between two $Ru_{0.95}O_2^{0.2-}$ films. However, the $Ru_{0.95}O_2^{0.2-}$ multilayer did not exhibited lamellar structure due to instability to electron beam. However, the overall thickness of $Ru_{0.95}O_2^{0.2-}$ nanosheets layers was according to number of deposited layers of $Ru_{0.95}O_2^{0.2-}$ nanosheets. $Ca_2Nb_3O_{10}^-$ based all-nanosheets capacitors exhibited moderate dielectric response of ~ 155 and small deviation of -12.5% in capacitance density at 200 ^oC. The leakage current densities of $Ca_2Nb_3O_{10}^-$ based all-nanosheets capacitors was investigated at various temperatures. At 25 ^oC, leakage current density was 10^{-6} A/cm^2 at +1V, which increase to 10^{-5} A/cm^2 at +1V at 250 ^oC which can be associated to larger leakage paths due to high surface roughness caused by $Ru_{0.95}O_2^{0.2-}$ nanosheets multilayers. The capacitance response of $Ca_2NaNb_4O_{13}^-$ based nanosheets capacitor fabricated in Chapter 3 is also studied. The studied MNC device demonstrated stable capacitance response as a factor of both temperature and voltage. MNC device realized stable capacitance response over a wide temperature range of -50 ~ 250 ^oC with small capacitance deviation of -5.5%.

It can be concluded that solution-based assembly of $Ca_2Nb_3O_{10}^-$ and $Ca_2NaNb_4O_{13}^-$ nanosheets as dielectric layers is an effective strategy to fabricate ultrathin multilayer nanosheets capacitors that realize high capacitance densities and low leakage current profiles at high temperatures and voltages. The simultaneous demonstration of high-*k* responses, low leakage profiles, and thermal stabilities by $Ca_2Nb_3O_{10}^-$ and $Ca_2NaNb_4O_{13}^-$ nanosheets capacitor with ultrathin

thickness < 30 nm, is signature of unique characteristics of ultrathin 2D perovskite nanosheets. However, such properties are not possible to achieve with thin films of current perovskites at ultrathin scale. Moreover, superior high-*k* properties of $Ca_2NaNb_4O_{13}^-$ nanosheets and large lateral size responsible for high insulating nature provides additional advantage over $Ca_2Nb_3O_{10}^-$ nanosheets based capacitors.

4.5. Reference

1. A. N. Hammoud, I. T. Myers, *Annu. Rep. Conf. Electr. Insul. Dielectr. Phenom.* p. 459 (1989).
2. R. W. Johnson, J. L. Evans, P. Jacobsen, J. R. Thompson, M. Christopher, *IEEE Trans. Electron. Packag. Manuf.* **27**, 164 (2004).
3. C. A. Randall, H. Ogihara, J. -R. Kim, G. -Y. Yang, C. S. Stringer, S. T. McKinstry, M. Lanagan, *IEEE Int. Pulsed Power Conf. Proc.* p. 346 (2009).
4. R. Z. Chen, X. H. Wang, Z. L. Gui, *J. Am. Ceram. Soc.* **86,** 1022 (2003).
5. D. Fu, M. Itoh, *Ferroelectric Material-Synthesis and Characterizatio*n, *InTech*. pp 105, (2015).
6. J. B. Lim, S. Zhang, N. Kim, T. R. Shrout, *J. Am. Ceram. Soc.* **92**, 679 (2009).
7. C. B. Parker, J. -P. Maria, A. I. Kingon, *Appl. Phys. Lett.* **81**, 340 (2002).
8. P. Padmini, T. R.Taylor, M. J. Lefevre, A. S. Nagra, R. A. York, J. S. Speck, *Appl. Phys. Lett.* **75**, 3186 (1999).
9. C. S. Hwang, *J. Appl. Phys.* **92**, 432 (2002).
10. G. D. Wilk, R. M. Wallace, J. M. Anthony, *J. Appl. Phys.* **89**, 5243 (2001).
11. S. K. Kim, W. -D. Kim, K. -M. Kim, C. S. Hwang, J. Jeong, *Appl. Phys. Lett.* **85**, 4112 (2004).
12. S. K. Kim, S. W. Lee, J. H. Han, B. Lee, S. Han, C. S. Hwang, *Adv. Funct. Mater*. **20**, 2989 (2010).
13. M. Osada, T. Sasaki, *Adv. Mater.* **24**, 210 (2012).
14. C. A. Randall, A. S. Bhalla, *Jpn. J. Appl. Phys.* **29**, 327 (1990).
15. Y. Ebina, K. Akatsuka, K. Fukuda, T. Sasaki, *Chem. Mater.* **24**, 4201 (2012).
16. Y. -H. Kim, H. -J. Kim, M. Osada, B. W. Li, Y. Ebina, T. Sasaki, *ACS Appl. Mater. Interfaces* **6**, 19510 (2014).
17. C. Wang, M. Osada, Y. Ebina, B. W. Li, K. Akatsuka, K. Fukuda, W. Sugimoto, R. Ma, T. Sasaki, *ACS Nano* **8**, 2658 (2014).
18. B. W. Li, M. Osada, Y. Ebina, K. Akatsuka, K. Fukuda, T. Sasaki, *ACS Nano* **8**, 5449 (2014).
19. Y. Ebina, T. Sasaki, M. Watanabe, Solid State Ionics, **151**, 177 (2002).
20. W. Sugimoto, H. Iwata, Y. Yasunaga, Y. Murakami, Y. Takasu, *Angew. Chem. Int. Ed.* **42**, 4092 (2003).

21. K. Fukuda, T. Saida, J. Sato, M. Yonezawa, Y. Takasu, W. Sugimoto, *Inorg. Chem.* **49**, 4391 (2010).
22. K. Akatsuka, M. Haga, Y. Ebina, M. Osada, K. Fukuda, T. Sasaki, *ACS Nano* **3**, 1097 (2009).
23. M. Osada, K. Akatsuka, Y. Ebina, Y. Kotani, K. Ono, H Funakubo, S. Ueda, K. Kobayashi, K. Takada, T. Sasaki, *Jpn. J. Appl. Phys.* **47**, 7556 (2008).
24. M. Osada, K. Akatsuka, Y. Ebina, H. Funakubo, K. Ono, K. Takada, T. Sasaki, *ACS Nano* **4**, 5225 (2010).
25. A. K. Jonscher, *J. Phys. D* **32**, R57 (1999).
26. B. W. Li, M. Osada, T. C. Ozawa, Y. Ebina, K. Akatsuka, R. Ma, H. Funakubo, T. Sasaki, *ACS Nano* **4**, 6673 (2010).

Chapter 5

Superlattice Assembly of 2D Perovskites for Tailored Ferroelectrics

5.1. Introduction

A constant demand for high performance and low-power consumption electronics triggered the quest for advanced materials with sophisticated functionalities.[1-3] To this end, the fast developments of two-dimensional (2D) materials have attracted extensive attention in this field. Inspired from the discovery and unique properties of graphene,[4] considerable research efforts on non-graphene 2D materials lead to establishment of vast library of inorganic 2D materials[5] such as *h*-BN,[6] chalcogenides,[7] oxides,[8] phosphites[9] and many more. Due to atomic scale thickness, 2D materials demonstrate far superior physical, chemical and electronic properties as compared to their bulk counterparts. For example, exciting 2D electronic phenomenon such as confined charge transport and enhanced surface polarization[10] provides possibilities to current technologies for the development of ultrathin future devices.

In parallel to the discovery of new 2D materials, an emerging research field is the LbL stacking of various 2D materials via van der Waals epitaxy to achieve novel heterostructures.[11,12] 2D materials with various compositions and electronic structures can be assembled in chosen sequences with atomic scale precision to realize artificial materials. This strategy offers rational choice of 2D materials as building blocks to explore new artificial materials with tailored properties. In this study, I implemented this concept to study new class of 2D perovskite nanosheets for the fabrication of new ultrathin electronic materials.

Complex perovskite oxides are technologically important inorganic materials due to their fascinating physical properties such as dielectric, ferroelectricity, colossal magnetoresistance and superconductivity.[13-15] To control these interesting properties at atomic scale in ultrathin perovskites is important to study new physics and device properties. The current advances in the synthesis of perovskite superlattices have provided access to create and control the degrees of freedom and afford new functionalities for future devices. Usually, the synthesis of perovskite superlattices has been achieved with modern technologies such as molecular beam epitaxy[16] and pulse laser deposition.[17] However, the quality of such superlattices is subject to close lattice matching among the constituent

perovskites to realize intergrowth free interfaces. These constraints limit the choice of materials to be employed by current thin-film technologies.[18]

Analogous to perovskite superlattices fabricated via modern thin film techniques, it is possible to fabricate perovskite superlattice comprised of perovskite nanosheets fabricated via solution-based assembly process. In previous work, Li *et al*. studied the LbL assembly of artificial superlattices consisting of $LaNb_2O_7^-$ and $Ca_2Nb_3O_{10}^-$ nanosheets as constituent materials. The superlattices assembly realized enhanced dielectric constant with development of ferroelectric property. However, $LaNb_2O_7^-$ nanosheets possess low ε_r value of 50 possibly because of lower *m* number and defects introduced by La presence. To this end, multilayer films of homologous series of perovskite nanosheets ($Ca_2Na_{m-3}Nb_mO_{3m+1}^-$; *m* = 3-6) due to higher *m* numbers exhibited high ε_r values of 210 (*m* = 3), 305 (*m* = 4), 390 (*m* = 5), and 470 (*m* = 6).[19]

Here, 2D perovskite nanosheets have been employed as building blocks, neatly tiled in unit-cell-level, for fabrication of perovskite heterostructures that possess potential applications as electronic materials. DJ-type homologous series of perovskite nanosheets ($Ca_2Na_{m-3}Nb_mO_{3m+1}^-$; *m* = 3-6) demonstrate variable thickness along the block normal due to presence of different number of NbO_6 octahedron units (i.e. integer *m*) and have virtually infinite perovskite blocks in the 2D planes. The precise control over the arrangement of exfoliated nanosheets of homologous perovskites ($Ca_2Na_{m-3}Nb_mO_{3m+1}^-$; *m* = 3-6) would lead to engineer the dielectric/ferroelectric properties at atomic scale level. Here, I established LbL assembly of homologous perovskite nanosheets ($Ca_2Na_{m-3}Nb_mO_{3m+1}^-$; *m* = 3-6) to study dielectric/ferroelectric responses.

5.2. Experimental

5.2.1. Synthesis of $Ca_2Na_{m-3}Nb_mO_{3m+1}^-$ nanosheets

Homologous series of perovskites nanosheets ($Ca_2Na_{m-3}Nb_mO_{3m+1}^-$; *m* = 3-6) have been synthesized via soft-chemical exfoliation of layered materials ($KCa_2Na_{m-3}Nb_mO_{3m+1}$; *m* = 3-6).[20] Na_2CO_3, K_2CO_3, $CaCO_3$, and Nb_2O_5 were used as precursors for the synthesis of starting layered material ($KCa_2Na_{m-3}Nb_mO_{3m+1}$; *m*

= 3-6). In the first step, the template material of $KCa_2Nb_3O_{10}$ was synthesized by burning mixture of K_2CO_3, $CaCO_3$, and Nb_2O_5 at molar ratio of 1.05/2/3 at 1473 K for 12 h in air. In second step, $NaNbO_3$ was synthesized by heating the mixture of Na_2CO_3 and Nb_2O_5 keeping Na/Nb = 1 at 1473 K for 12 h. Homologous layered materials $KCa_2Na_{m-3}Nb_mO_{3m+1}$; m = 4-6 were prepared by reaction of template $KCa_2Nb_3O_{10}$ material with specific amount of $NaNbO_3$ at 1573 K. Resultantly, layered $KCa_2Na_{m-3}Nb_mO_{3m+1}$; m = 3-6 materials were treated with aqueous solution of 400 cm^3 of HNO_3 (5 mole/cm^3) for 3 days. During acid treatment, acid is replaced every day. After 3 days, the protonic form was filtered and washed with excess amount of water and dried in air. The protonated forms $HCa_2Na_{m-3}Nb_mO_{3m+1}\cdot 1.5H_2O$; m = 3-6 were treated with TBAOH aqueous solution (300 cm^3) and TBA^+/H^+ ratio was adjusted at 1 to achieve exfoliation of layered protonated phase into single nanosheets (Figure 5.1). In the end, unexfoliated residues are separated from exfoliated nanosheets via centrifugation at 1500 rpm for 10 min.

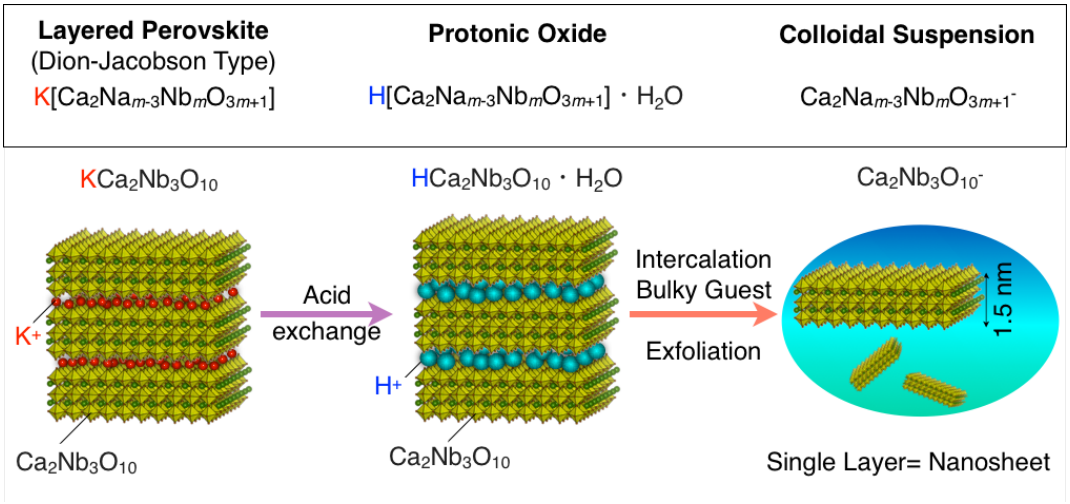

Figure 5.1. Soft-chemical exfoliation of layered perovskite to synthesize homologous series of perovskite nanosheets.

5.2.2. Fabrication of superlattice films using $Ca_2Na_{m-3}Nb_mO_{3m+1}^-$ nanosheets

Facile LB method is employed for LbL assembly of homologous series of perovskite nanosheets to realize superlattice films.[21] Substrates such as Si wafers

and quartz glass were cleaned by immersion in CH_3OH/HCl (1:1) solution followed by dipping in 18M H_2SO_4 for 30 minutes each. Atomically flat $SrRuO_3$ substrates were cleaned under UV-light treatment in ozone for 30 min. For the fabrication of multilayers/superlattices, the diluted suspension of 96 mg/dm^3, 108 mg/dm^3, 112 mg/dm^3 and 116 mg/dm^3 were used for homologous nanosheets from m = 3-6, respectively. The diluted suspensions of perovskite nanosheets were spread in LB trough seperately and for each homologous perovskite nanosheets, the waiting time was 5 min after spreading the diluted suspensions. The surface pressures of homologous series of perovskite nanosheets were adjusted between 15-16 mN/m through inward movement of barriers at 0.5 mm s^{-1}. A waiting time of 5-10 was employed after achieving the desired surface pressure for homologous perovskite nanosheets. All the multilayers/superlattice films have been fabricated at regulated temperature of 25 ± 0.50 ^{o}C. Densely pack monolayer films of perovskite nanosheets floating at the air/water interface were transferred on to substrate through lifting-up the substrates at 0.0167 mm s^{-1}. The similar procedure was repeated n number of times to fabricate multilayer/superlattice films of homologous series of perovskite nanosheets. The fabricated multilayer/superlattice films were kept under UV treatment for 48 hours to decompose tetrabutyl ammonium ions present in the galleries of multilayer/superlattice films. It was confirmed through Infrared absorption results that UV-treated nanosheets films were consisted of lamellar structure of negatively charged nanosheets and positively charged cations such as NH_4^+ ions. The schematic for multilayer/superlattices fabrication is given in Figure 5.2.

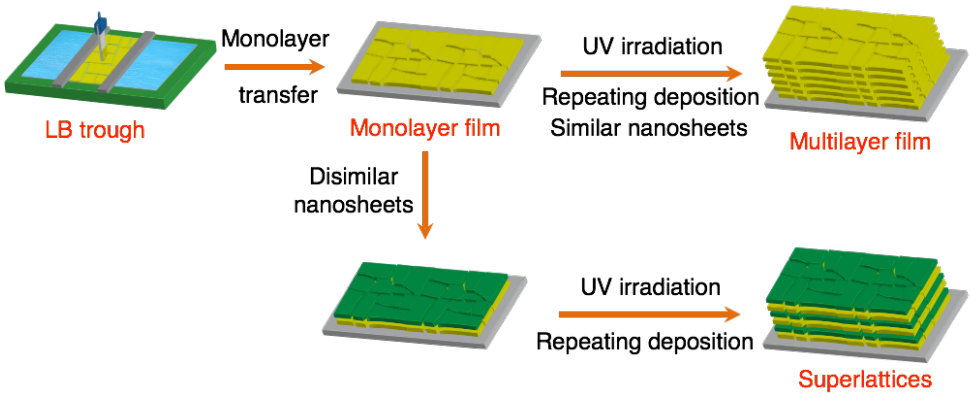

Figure 5.2. Fabrication of multilayer/superlattice films of homologous series of perovskite nanosheets via LB technique.

5.2.3. Characterization

UV-visible spectra were collected by a Hitachi U-4100 spectrophotometer during multilayers and superlattices fabrication process. Surface profiles of monolayer films of homologous series of perovskite nanosheets were observed using SII Nano- technology E-sweep AFM. The fabrication quality of superlattices was examined through cross-sectional view with the help of Hitachi H-9000 TEM operating a 200 kV with a point resolution of 0.1 nm.

Electrical properties were recorded by preparing Au/(nanosheet)$_n$/$SrRuO_3$ ultrathin capacitors. Top Au electrodes with thickness of 50 nm and diameter of 100 μm were deposited with the help of vacuum-evaporation method. Dielectric and leakage current profiles were observed with Keithley 4200-SCS-semiconductor parameter analyzer and Agilent 4294A precision impedance analyzer, respectively. Ferroelectric properties were measured by using a virtual system (Toyo corporation 6252 Rev. C).

5.3. Results and Discussion

5.3.1. Characterization of $Ca_2Na_{m-3}Nb_mO_{3m+1}$ superlattices

The AFM images (Figure 5.3) confirmed the sheet like morphology of

homologous series of perovskite nanosheets. The height profiles of these nanosheets exhibited thickness of 1.87 ± 0.10, 2.29 ± 0.10, 2.86 ± 0.10, and 3.27 ± 0.10 nm for $Ca_2Nb_3O_{10}^-$, $Ca_2NaNb_4O_{13}^-$, $Ca_2Na_2Nb_5O_{16}^-$, and $Ca_2Na_3Nb_6O_{19}^-$ nanosheet, respectively. The thickness of each homologous member is inherited to the number of NbO_6 octahedra present in respective host layer in the parent compound.

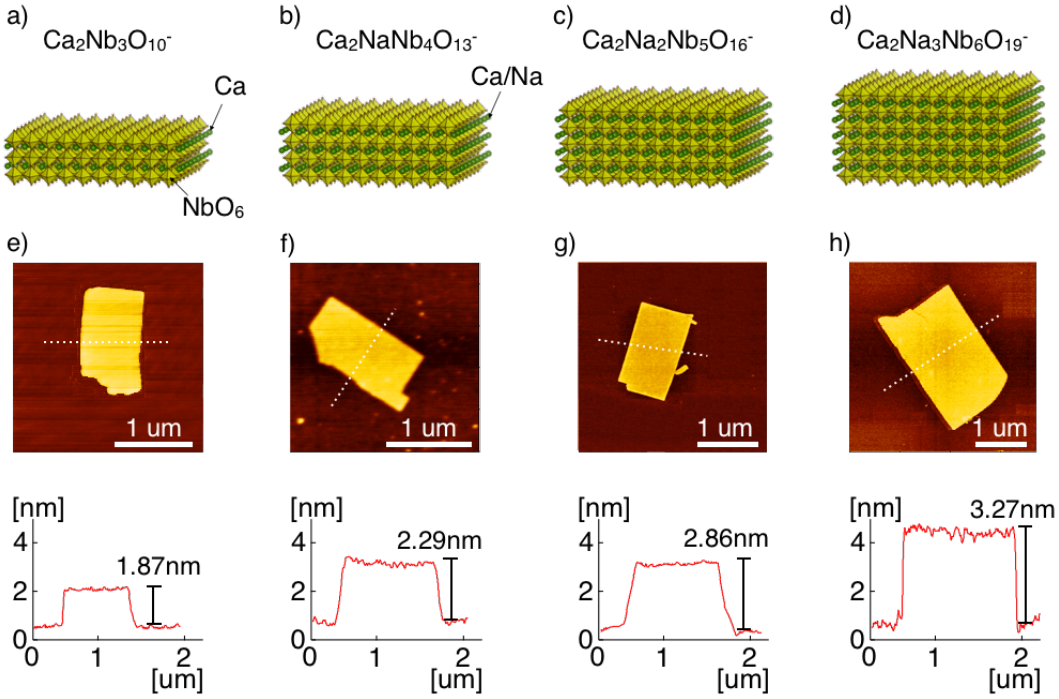

Figure 5.3. Structure and AFM images of **(a, e)** $Ca_2Nb_3O_{10}^-$, **(b, f)** $Ca_2NaNb_4O_{13}^-$ **(c, g)** $Ca_2Na_2Nb_5O_{16}^-$ **(d, h)** $Ca_2Na_3Nb_6O_{19}^-$ nanosheets. Height profiles are illustrated for each nanosheet in their bottom panels.

LB method is an effective approach for fabricating atomically uniform films with the help of atomically flat substrate such as $SrRuO_3$. Taping mode AFM images (Figure 5.4a-d) confirmed the successful fabrication of densely packed monolayer films of homologous series of perovskite nanosheets. The average surface roughness observed for monolayer layers was ~ 0.3 nm with surface coverage above 95%. A high-quality deposition of monolayer films were repeated *n* number of times to achieve desired multilayer/superlattice films. Monolayer films of perovskite nanosheets were observed via taping-mode AFM under

vacuum condition.

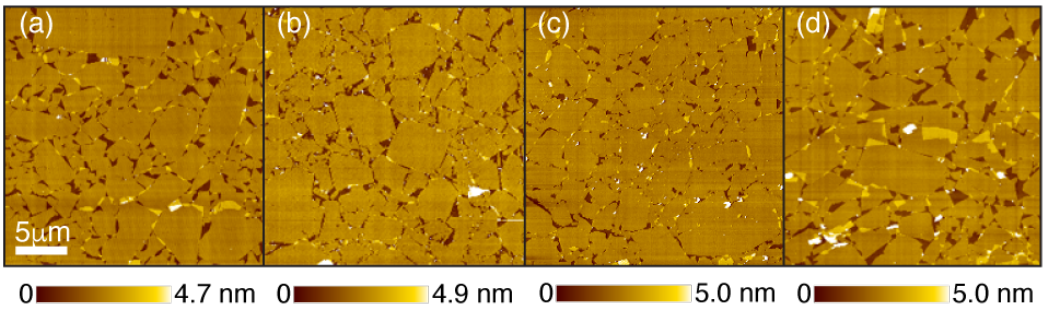

Figure 5.4. AFM images monolayer films of **(a)** $Ca_2Nb_3O_{10}^-$, **(b)** $Ca_2NaNb_4O_{13}^-$, **(c)** $Ca_2Na_2Nb_5O_{16}^-$, **(d)** $Ca_2Na_3Nb_6O_{19}^-$ nanosheets.

Figure 5.5 displays the structure of homologous members of perovskites nanosheets ($Ca_2Na_{m-3}Nb_mO_{3m+1}^-$; m = 3-6) along with schematic for the superlattice fabrication. Each superlattice film is composed of two different homologous series of perovskite members. In this study, I prepared 3 different superlattices including $(Ca_2Nb_3O_{10}^-/Ca_2NaNb_4O_{13}^-)_6$, $(Ca_2Nb_3O_{10}^-/Ca_2Na_2Nb_5O_{16}^-)_6$ and $(Ca_2Nb_3O_{10}^-/Ca_2Na_3Nb_6O_{19}^-)_6$. I also fabricated multilayer films of each homologous series of perovskite nanosheets to study the effect of superlattices assembly process.

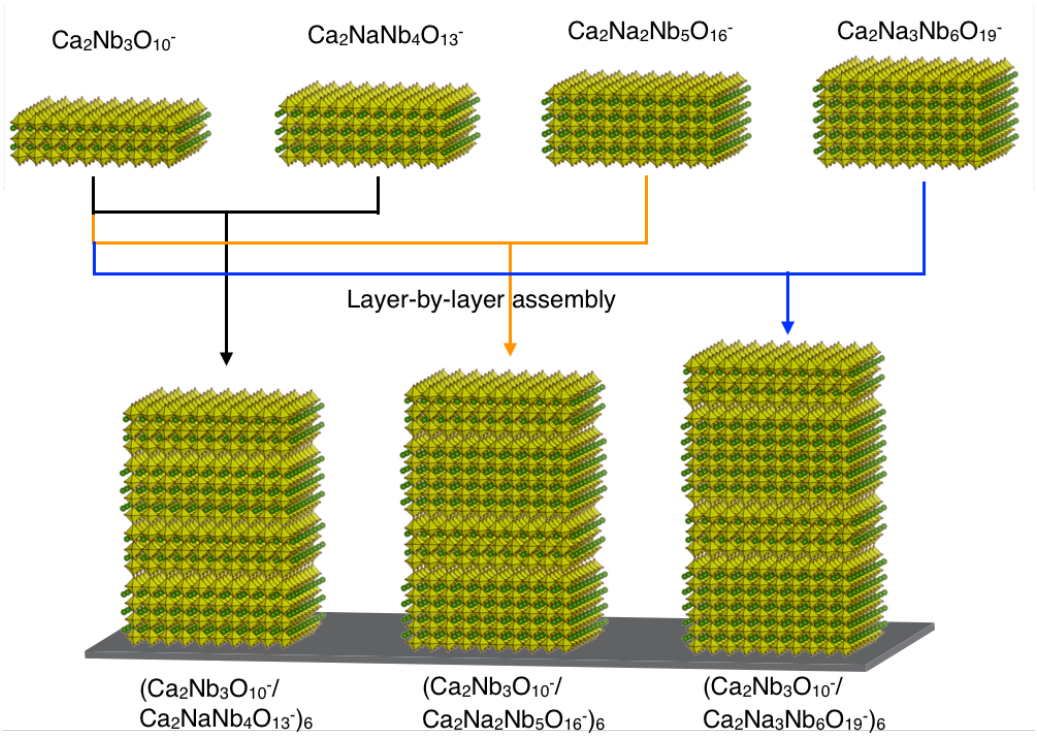

Figure 5.5. Structure and schematic view of LbL assembly of $(Ca_2Nb_3O_{10}^-/Ca_2NaNb_4O_{13}^-)_6$, $(Ca_2Nb_3O_{10}^-/Ca_2Na_2Nb_5O_{16}^-)_6$ and $(Ca_2Nb_3O_{10}^-/Ca_2Na_3Nb_6O_{19}^-)_6$ superlattices.

Cross-sectional HRTEM observations (Figure 5.6a, b) demonstrate that $(Ca_2Nb_3O_{10}^-/Ca_2NaNb_4O_{13}^-)_5$ superlattice is homogenous in coverage and films thickness. Moreover, a clean interface can be observed between the constituent layers and the substrate confirming the fabrication of high quality superlattice film. Figure 5.6b revealed that approximate thickness of ~1.80 and ~2.20 nm can be associated to $Ca_2Nb_3O_{10}^-$ and $Ca_2NaNb_4O_{13}^-$ nanosheets lamellar structure which is in close representation with thickness observed via topographic AFM images for $Ca_2Nb_3O_{10}^-$ and $Ca_2NaNb_4O_{13}^-$ nanosheets, respectively. Moreover, there were no observable stacking imperfections in the superlattice film. Consequently, the alternate tiling of $Ca_2NaNb_4O_{13}^-$ and $Ca_2Nb_3O_{10}^-$ nanosheets is preserved with atomic scale precision over a broader area.

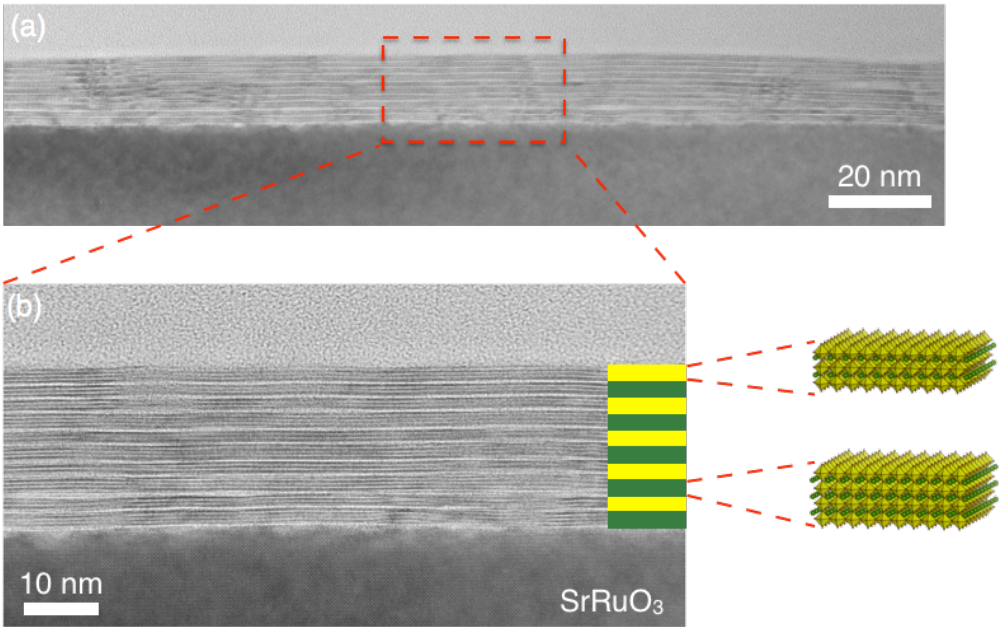

Figure 5.6. Cross-sectional HRTEM image of $(Ca_2Nb_3O_{10}^-/Ca_2NaNb_4O_{13}^-)_5$. **(a)** Cross-sectional HRTEM image of superlattice film of $(Ca_2Nb_3O_{10}^-/Ca_2NaNb_4O_{13}^-)_5$. and **(b)** High-resolution HRTEM image of specific area shown in (a).

Table 5.1. Abbreviation used for different multilayer and superlattice films.

S. No.	Multilayers/Superlattices	Sample Name
1	$(Ca_2Nb_3O_{10}^-)_{10}$	ML-1
2	$(Ca_2NaNb_4O_{13}^-)_{10}$	ML-2
3	$(Ca_2Na_2Nb_5O_{16}^-)_{10}$	ML-3
4	$(Ca_2Na_3Nb_6O_{19}^-)_{10}$	ML-4
5	$(Ca_2Nb_3O_{10}^-/Ca_2NaNb_4O_{13}^-)_6$	SL-1
6	$(Ca_2Nb_3O_{10}^-/Ca_2Na_2Nb_5O_{16}^-)_6$	SL-2
7	$(Ca_2Nb_3O_{10}^-/Ca_2Na_3Nb_6O_{19}^-)_6$	SL-3

The multilayers/superlattices build-up process was examined by obtaining UV-visible absorption spectra after each deposition of monolayer film. Figure 5.7a-d describes the build-up process for $(Ca_2Nb_3O_{10}^-)_{10}$, $(Ca_2NaNb_4O_{13}^-)_{10}$,

$(Ca_2Na_2Nb_5O_{16}^-)_{10}$ and $(Ca_2Na_3Nb_6O_{19}^-)_{10}$ multilayer films. The absorption peaks centered at 232, 258, 265 and 269 nm are characteristic of $Ca_2Nb_3O_{10}^-$, $Ca_2NaNb_4O_{13}^-$, $Ca_2Na_2Nb_5O_{16}^-$, and $Ca_2Na_3Nb_6O_{19}^-$, respectively. Figure 5.7e-g displays the absorption spectra for $(Ca_2Nb_3O_{10}^-/Ca_2NaNb_4O_{13}^-)_6$, $(Ca_2Nb_3O_{10}^-/Ca_2Na_2Nb_5O_{16}^-)_6$, and $(Ca_2Nb_3O_{10}^-/ Ca_2Na_3Nb_6O_{19}^-)_6$ superlattices. Each spectral line in these figures represents the absorption given by transferred monolayer on quartz substrate confirming the deposition of high quality monolayers in every step.

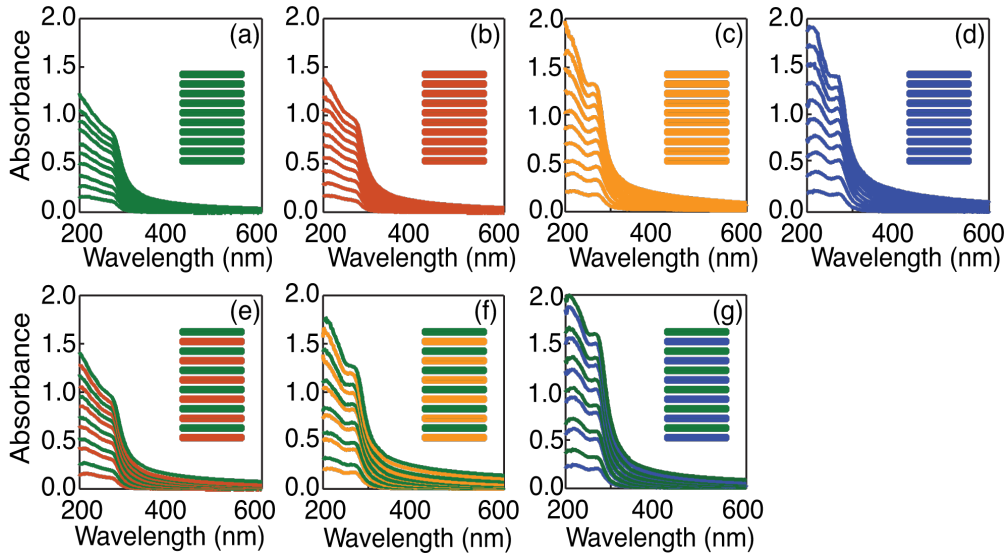

Figure 5.7. UV-visible absorption profiles during multilayer/superlattice fabrication process. **(a)** $(Ca_2Nb_3O_{10}^-)_{10}$, **(b)** $(Ca_2NaNb_4O_{13}^-)_{10}$, **(c)** $(Ca_2Na_2Nb_5O_{16}^-)_{10}$, **(d)** $(Ca_2Na_3Nb_6O_{19}^-)_{10}$, (e) $(Ca_2Nb_3O_{10}^-/Ca_2NaNb_4O_{13}^-)_6$, (f) $(Ca_2Nb_3O_{10}^-/Ca_2Na_2Nb_5O_{16}^-)_6$, **(g)** $(Ca_2Nb_3O_{10}^-/Ca_2Na_3Nb_6O_{19}^-)_6$. In-sets exhibit graphical designs of multilayers/superlattice structures with corresponding colors.

In order to investigate the lamellar structure of superlattice films, I have measured XRD profiles. The presence of sharp peaks with flat region in between confirmed that lamellar structure of perovskite nanosheet in superlattice films (Figure 5.8 a-c) has been realized in a perfect manner. The main peaks for $(Ca_2Nb_3O_{10}^-/Ca_2NaNb_4O_{13}^-)_6$ superlattice appeared at $2\theta = \sim 22.7^o$ and 46.4^o can be indexed as 001 and 002 reflections, respectively and the presence of other small peaks can be considered as reflection form Laue interference function.[22]

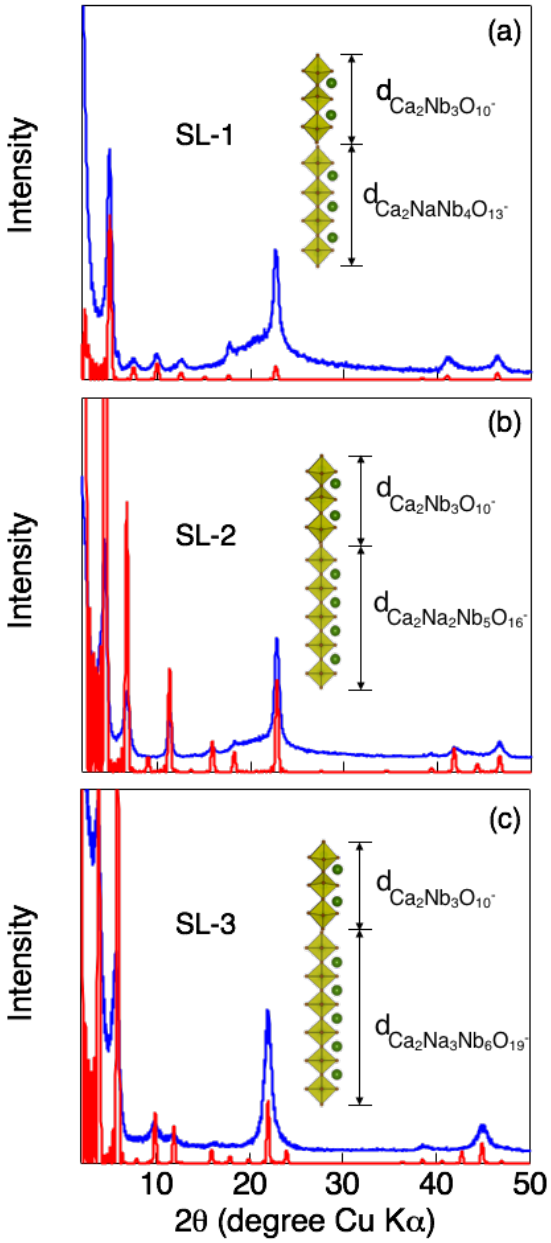

Figure 5.8. XRD data for superlattice films of **(a)** $(Ca_2Nb_3O_{10}^-/Ca_2NaNb_4O_{13}^-)_6$, **(b)** $(Ca_2Nb_3O_{10}^-/Ca_2Na_2Nb_5O_{16}^-)_6$ and **(c)** $(Ca_2Nb_3O_{10}^-/Ca_2Na_3Nb_6O_{19}^-)_6$. The blue and red spectra express experimental and calculated profiles, respectively.

With small deviation to lower angles, the position of main peaks for $(Ca_2Nb_3O_{10}^-/Ca_2Na_2Nb_5O_{16}^-)_6$ and $(Ca_2Nb_3O_{10}^-/Ca_2Na_3Nb_6O_{19}^-)_6$ superlattices was observed. Moreover, the increase in small peaks between main peaks for SL-2 and SL-3 can be assigned to increasing thickness profile of one constituent of

superlattices. To understand the lamellar structure of superlattice films, the structure factor, F for each superlattice film were calculated based on the scattering vector normal to film surface and XRD intensities are simulated from following equations:

$$F = \sum_j f_j \exp\left(2\pi i\left(2z_j \frac{\sin\theta}{\lambda}\right)\right) \quad \text{(5.1)}$$

$$I = \frac{1 + \cos^2 2\theta}{\sin^2\theta \cos\theta} FF^* \quad \text{(5.2)}$$

where, f_j and Z_j are atomic scattering factors and location of jth atom, λ represents wavelength of X-rays and θ expresses the scattering angle. First term in equation 5.1 is Lorentz polarization factor. In case of superlattice films, the calculation is done based on the structural mode given for each superlattice in Figure 5.8 a-c. The height of NbO_6 is considered as 0.3935 nm, that are connected via corner sharing mode and Ca/Na ions are presents in ratio of 2:m-3; (m = 3-6) at midline among two octahedra. The simulated profiles (red lines in Figure 5.8) are in well match with the XRD spectra of our superlattices films confirming the successful deposition of superlattice films.

5.3.2. Dielectric and ferroelectric properties of $Ca_2Na_{m-3}Nb_mO_{3m+1}^-$ superlattices

Figure 5.9 combines the *P-E* profiles of three superlattices ($Ca_2Nb_3O_{10}^-$/ $Ca_2NaNb_4O_{13}^-)_6$, ($Ca_2Nb_3O_{10}^-/Ca_2Na_2Nb_5O_{16}^-)_6$, and ($Ca_2Nb_3O_{10}^-/Ca_2Na_3Nb_6O_{19}^-)_6$ together. The ($Ca_2Nb_3O_{10}^-/Ca_2Na_2Nb_5O_{16}^-)_6$ superlattice (blue profile) exhibits a well-defined hysteresis behavior inherent to ferroelectricity, whereas ($Ca_2Nb_3O_{10}^-$ /$Ca_2NaNb_4O_{13}^-)_6$ superlattice exhibit weak ferroelectric response (red profile) and ($Ca_2Nb_3O_{10}^-$/ $Ca_2Na_3Nb_6O_{19}^-)_6$ superlattice (green profile) is paraelectric in nature. These observations indicate the potential effect of heterointerface on polarization properties in the superlattice film with constituent nanosheets comprised of odd number of NbO_6 as in case of ($Ca_2Nb_3O_{10}^-/Ca_2Na_2Nb_5O_{16}^-)_6$ superlattice. The superlattices with one constituent nanosheet consisting of even number of NbO_6 unit may neutralize the polarization developed as a result of heterointerface, leading to weak or no ferroelectric behavior as in ($Ca_2Nb_3O_{10}^-/Ca_2NaNb_4O_{13}^-)_6$ and

$(Ca_2Nb_3O_{10}^-/ Ca_2Na_3Nb_6O_{19}^-)_6$, respectively. In case of $(Ca_2Nb_3O_{10}^-/Ca_2Na_2Nb_5O_{16}^-)_6$ superlattice, the connectivity of NbO_6 octahedra along the c-axis in odd number of NbO_6 especially in m = 5 enables the displacement of Nb^{5+} in O^{2-}-Nb^{5+}-O^{2-} bonding leading to increase polarizability. Due to higher polarizability in larger m member such as m = 5, is responsible to induce ferroelectric instabilities.[19] This can lead to development of ferroelectric property in $(Ca_2Nb_3O_{10}^-/Ca_2Na_2Nb_5O_{16}^-)_6$ superlattice. Hence, the ferroelectric response in $(Ca_2Nb_3O_{10}^-/Ca_2Na_2Nb_5O_{16}^-)_6$ superlattice is an intrinsic signature of engineered interface and not an outcome of leakage current.

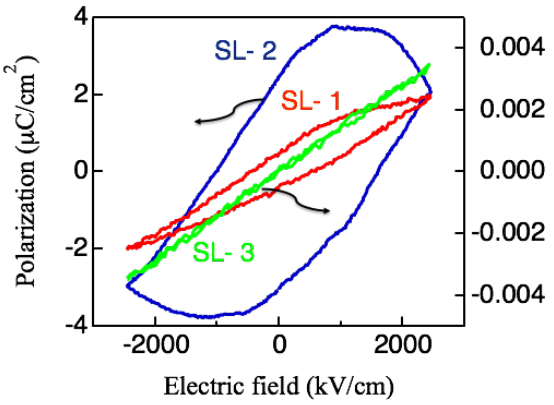

Figure 5.9. Ferroelectric responses measured from $(Ca_2Nb_3O_{10}^-/Ca_2NaNb_4O_{13}^-)_6$, $(Ca_2Nb_3O_{10}^-/Ca_2Na_2Nb_5O_{16}^-)_6$ and $(Ca_2Nb_3O_{10}^-/Ca_2Na_3Nb_6O_{16}^-)_6$ superlattices.

The insulating properties of multilayer films along with their superlattice films (Figure 5.10 a-c) were studied. In all three cases, the superlattices exhibited superior insulating properties than multilayer films of their constituent nanosheets. The possible presence of Na at *A*-site of one constituent ($Ca_2NaNb_4O_{13}^-$, $Ca_2Na_2Nb_5O_{16}^-$ and $Ca_2Na_3Nb_6O_{19}^-$) and Ca at *A*-site of $Ca_2Nb_3O_{10}^-$ nanosheets in superlattices can produce polar discontinuities at the interface between $Ca_2Nb_3O_{10}^-/Ca_2NaNb_4O_{13}^-$, $Ca_2Nb_3O_{10}^-/Ca_2Na_2Nb_5O_{16}^-$ and $Ca_2Nb_3O_{10}^-/Ca_2Na_3Nb_6O_{16}^-$, leading to compensation of polarization bound charge at interface. The resulting structure is locally polarized and has strongly broken inversion symmetry. Superlattices of such type observed to demonstrate better insulating properties.[23] Moreover, the interface between $SrRuO_3$ substrate and perovskites nanosheets is supposed to have more polar discontinuities due to presence of different *A*- and *B*-

site cations and contributing to enhance insulating behavior.

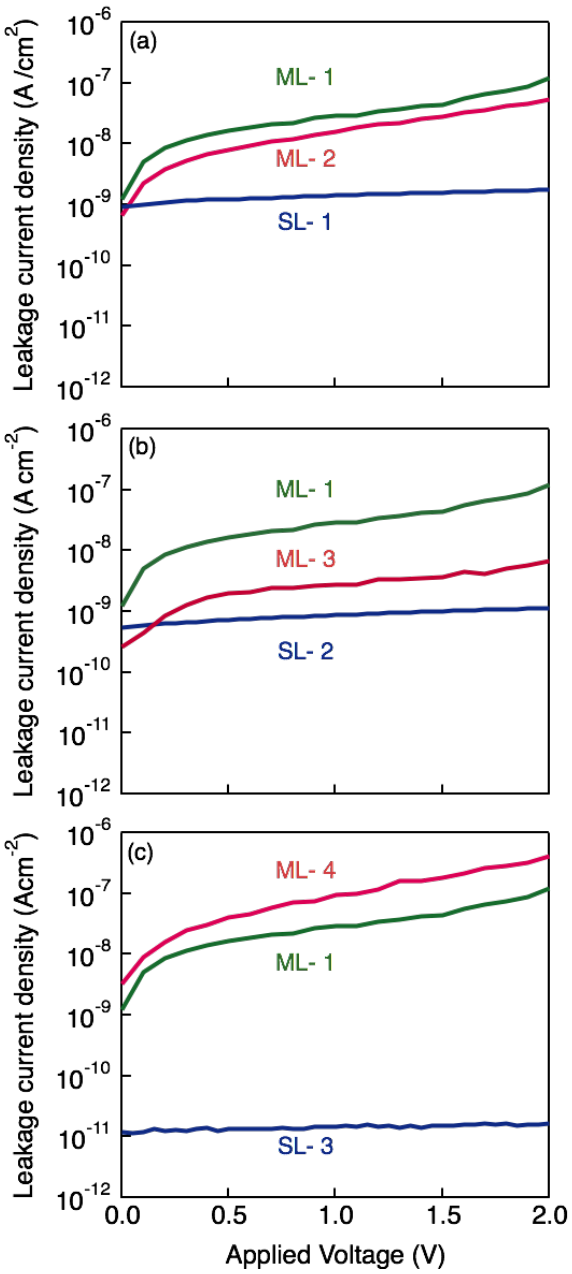

Figure 5.10. *J*—*V* curves of various nanosheet superlattices in comparison with their constituent multilayer films. **(a)** $(Ca_2Nb_3O_{10}^-/Ca_2NaNb_4O_{13}^-)_6$, **(b)** $(Ca_2Nb_3O_{10}^-/Ca_2Na_2Nb_5O_{16}^-)_6$, **(c)** $(Ca_2Nb_3O_{10}^-/Ca_2Na_3Nb_6O_{16}^-)_6$.

Moreover, it is supposed that contact between homologous nanosheets in perovskites superlattices at interface is governed by Schottky emission. The energy band diagram at interface between homologous nanosheets is given in

Figure 5.11. At interface, the homologous nanosheets, which possess different energy gaps values results in different position of valence band maximum (E_V) and conduction band minimum (E_C) leading to discontinuities called offsets. The discontinuities form barriers for charge transport at the interface and are responsible for insulating properties. Due to increased discontinuities in $Ca_2Nb_3O_{10}$ and $Ca_2Na_3Nb_6O_{19}$ band alignments, the resulting superlattice showed maximum blockage of charge carriers and hence responsible for large insulation.

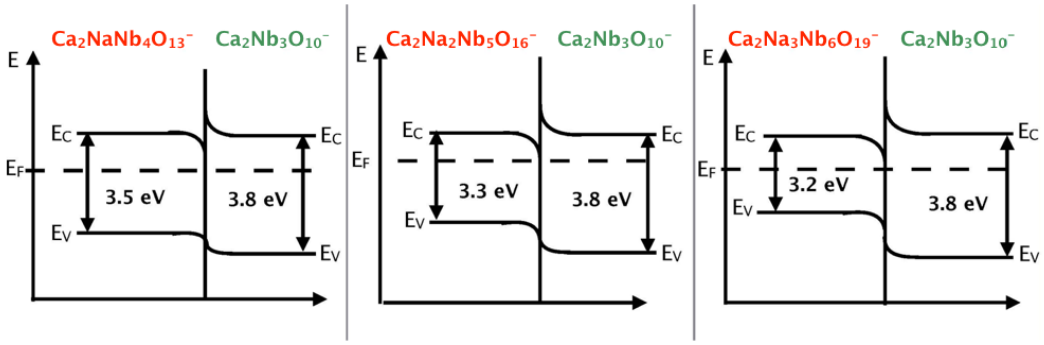

Figure 5.11. Leakage current density in different superlattice films is governed by Schottky emission at interface between different homologous nanosheets.

Dielectric response for superlattice films along with their constituent multilayer films is given in Figure 5.12 a-c. Usually, dielectric characteristics of two-component system can be explained with the help of series of the parallel capacitor model, and ε_r value of the $(Ca_2Nb_3O_{10}^-/Ca_2Na_2Nb_5O_{16}^-)_6$ superlattice can account for following formula:

$$\frac{t_{\text{Superlattice}}}{\varepsilon_{\text{Superlattice}}} = \frac{t_{Ca_2Nb_3O_{10}}}{\varepsilon_{Ca_2Nb_3O_{10}}} + \frac{t_{Ca_2Na_2Nb_5O_{16}}}{\varepsilon_{Ca_2Na_2Nb_5O_{16}}} \qquad \text{(5.3)}$$

where, t is the thickness of the dielectric component. Similarly, the calculated dielectric response for other 2 superlattices was measured using formula 5.3. It is obvious from dielectric response of all the superlattice films that interfacial effect is responsible for increase in polarization in superlattice films and hence result in enhanced dielectric response. It is observed that $(Ca_2Nb_3O_{10}^-/Ca_2NaNb_4O_{13}^-)_6$,

$(Ca_2Nb_3O_{10}^-/Ca_2Na_2Nb_5O_{16}^-)_6$, $(Ca_2Nb_3O_{10}^-/Ca_2Na_3Nb_6O_{19}^-)_6$ superlattices exhibited superior ε_r response of ~296, 427, 394 at 1 kHz compared to calculated dielectric response from parallel capacitor model as 254, 291, 324 based on respective constituent nanosheets, respectively. In case of $(Ca_2Nb_3O_{10}^-/Ca_2Na_2Nb_5O_{16}^-)_6$ superlattice, the dielectric value is higher than the dielectric constants for both constituent multilayer films. This significant increase in ε_r suggest the possible presence of the interfacial effect on polarization properties in the $(Ca_2Nb_3O_{10}^-/Ca_2Na_2Nb_5O_{16}^-)_6$ superlattice, where asymmetric environment due to odd number of NbO_6 in both constituent nanosheets (NbO_6 = 3 and 5) and residual dipoles at the interface are responsible for enhanced polarization.

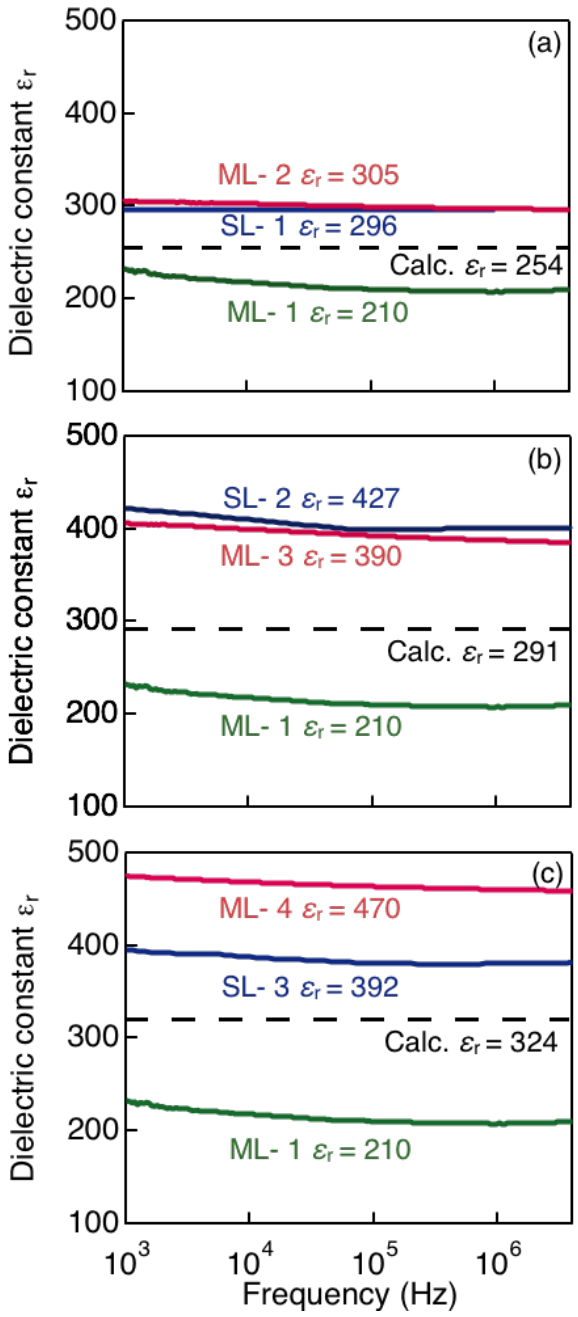

Figure 5.12. Dielectric properties of various nanosheet superlattices in comparison with their constituent multilayer films. **(a)** $(Ca_2Nb_3O_{10}^-/Ca_2NaNb_4O_{13}^-)_6$, **(b)** $(Ca_2Nb_3O_{10}^-/Ca_2Na_2Nb_5O_{16}^-)_6$, **(c)** $(Ca_2Nb_3O_{10}^-/Ca_2Na_3Nb_6O_{16}^-)_6$. In each panel, the calculated ε_r values from a parallel capacitor model are represented in dashed line.

It is assumed that interface engineering involves emergence of ferroelectricity as a direct product. In case of ($Ca_2Na_{m-3}Nb_mO_{3m+1}^-$; m = 3-6) nanosheets, the increase of NbO_6 octahedra along the thickness is responsible for higher polarizability in the homologous members with larger m. When these homologous series of perovskite are assembled via LbL on unit-cell level, the asymmetric environment provides the synergistic effect and is responsible of increased polarization. However, in case of perovskite nanosheets with odd number of NbO_6 octahedra, the asymmetric environment can cause energy lowering distortions such as tilting or rotation of NbO_6 octahedra or may induce rearrangement of central octahedral cations with respect to oxygen atoms in octahedra breaking the center of symmetry. These energy-lowering distortions can be responsible for interface-based induction of improper ferroelectricity in the artificial superlattice.

This feature is analogous to the improper ferroelectricity experienced in ferroelectric/paraelectric superlattices.[24] Our approach will offer a new direction for the fabrication of novel ferroelectric materials with enhanced high-k responses.

The position of NH^+ ions at the interface can be understood from structural mode employed (Figure 5.8 a-c, insets) to calculate structural factor and XRD intensities of the superlattices films. From XRD profiles, it was confirmed that experimental observations are in accordance with simulated results. The structural mode (Figure 5.8 a-c, insets) states that NH^+ ions are usually absent at interface between corner sharing oxygen atoms of octahedra of perovskite nanosheets. The possible presence of NH^+ ions can be at mid-line of two octahedra at interface.

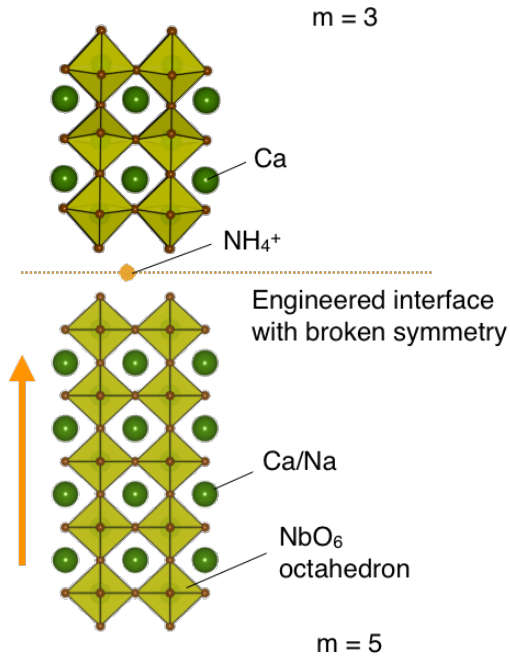

Figure 5.13. Graphical representations of the ($Ca_2Nb_3O_{10}^-/Ca_2Na_2Nb_5O_{16}^-$) interface and atomic motions associated to different energy lowering distortions.

Superlattice assembly of ultrathin homologous series of perovskite ($Ca_2Na_{m-3}Nb_mO_{3m+1}^-$; m = 3-6) nanosheets is an effective to tune the dielectric/ferroelectric properties. Through solution-based LbL assembly of homologous members its has been possible to fabricate superlattice films in which the constituents nanosheets possess larger dielectric constant differences ranging from 90 to 260. Such a high dielectric constant differences in superlattice films can lead to polar discontinuities, which result in enhancement of existing dielectric properties and development of novel ferroelectric properties. The fabrication of such superlattice with larger m perovskite members is not possible to achieve with current thin films technique hence making this solution-based LbL assembly via LB method an intriguing strategy to construct novel heterostructures.

In the homologous series, as the m is increased, the polarizability is also increased. When such homologous members are assembled in the form of superlattices, due to interfacial effect, the resulting superlattice films achieve increased polarization leading to enhanced dielectric response. Furthermore, the band gap discontinuities at the interface between different perovskite at the interface are responsible to realize Schottky type barrier at the interface and hence

lead to blockage of charge carrier transport across the interface and hence lead to highly insulating properties of the superlattices. Finally, when superlattice films are comprised of odd number of octahedra units containing perovskite nanosheets (i.e. *m*3/*m*5) then specially in case of $m = 5$ the connectivity of NbO_6 octahedra along the c-axis enables the displacement of Nb^{5+} in O^{2-}-Nb^{5+}-O^{2-} bonding leading to increase polarizability. Higher polarizability in larger *m* member such as $m = 5$, is responsible to induce ferroelectric instabilities.[19] that resulted in development of ferroelectric property in $(Ca_2Nb_3O_{10}^-/Ca_2Na_2Nb_5O_{16}^-)_6$ superlattice.

5.4. Summary

The successfully fabrication of multilayer/superlattice films of high-*k* homologous perovskite ($Ca_2Na_{m-3}Nb_mO_{3m+1}^-$; $m = 3$-6) nanosheets has been realized. The built-up process and cross-sectional observation of fabrication of multilayer/superlattice assemblies was investigated with the help of UV-visible spectra and cross-sectional HRTEM. Through LbL assembly it is possible to realize atomically sharp interface between high-*k* multilayer/superlattice films and substrates. It was observed that superlattice film consisting of odd number of perovskite nanosheets are quite specially in which asymmetric environment further increase the polarization properties and hence leads to significant increase in dielectric response and development of novel ferroelectric properties. Furthermore, superlattice films also exhibited reduced leakage current density of $< 10^{-9}$ A/cm^2 due to band gap discontinuities. In spite of paraelectric nature of constituent nanosheets, superlattice films realized interface engineering that is responsible for ferroelectricity. In this work, emergence of ferroelectricity and high-*k* properties as a direct product of the interfacial effect and can foresee the development of novel superlattice films by employing 2D nanosheets in which interface engineering will be used to tune material properties.

5.5. References

1. J. Mannhart, D. G. Schlom, *Science* **327**, 1607 (2010).
2. C. H. Ahn, K. M. Rabe, J. M. Triscone, *Science* **303**, 488 (2004).
3. B. H. Park, B. S. Kang, S. D. Bu, T. W. Noh, J. Lee, W. Jo, *Nature* **401**, 682 (1999).
4. K. S. Novoselov, A. K. Geim, S. V. Morozov, D. Jiang, Y.Zhang, S. V. Dubonos, I. V. Grigorieva, A. A. Firsov, *Science* **306**, 666 (2004).
5. V. Nicolosi, M. Chhowalla, M. G. Kanatzidis, M. S. Strano, J. N. Coleman, *Science* **340**, 12262191 (2013).
6. K. K. Kim, A. Hsu, X. Jia, S. M. Kim, Y. Shi, M. Hofmann, D. Nezich, J. R. Nieva, M. Dresselhaus, T. Palacios, J. Kong, *Nano Lett.* **12**, 161 (2012).
7. J. Zheng, H. Zhang, S. Dong, Y. Liu, N. C. Tai S. H. Suk, J. H. Young, B. Liu, L. K. Ping *Nat. Commun.* **5**, 2995 (2014).
8. T. Sasaki, M. Watanabe, H. Hashizume, H. Yamada, H. Nakazawa, *J. Am. Chem. Soc.* **118**, 8329 (1996).
9. P. Atienzar, M. de Victoria-Rodriguez, O. Juanes, J. Rodriguez-Ubis, E. Brunet, H. Garcia, *Energy Environ. Sci.* **4**, 4718 (2011).
10. H. Y. Hwang, Y. Iwasa, M. Kawasaki, B. Keimer, N. Nagaosa, Y. Tokura, *Nat. Mater.* **11**, 103 (2012).
11. A. K. Geim, I. V. Grigorieva, *Nature* **499**, 419 (2013).
12. K. S. Novoselov, A. Mishchenko, A. Carvalho, A. H. Castro Neto, *Science* **353**, 9439 (2016).
13. M. Osada, T. Sasaki, K. Ono, Y. Kotani, S. Ueda, K. Kobayashi, *ACS Nano* **5**, 6871 (2011).
14. L. Li, J. Britson, J. R. Jokisaari, Y. Zhang, C. Adamo, A. Melville, D. G. Schlom, L. Chen, X. Pan, *Adv. Mater.* **28**, 6574 (2016).
15. Y. F. Nie, P. D. C. King, C. H. Kim, M. Uchida, H. I. Wei, B. D. Faeth, J. P. Ruf, J. P. C. Ruff, L. Xie, X. Pan, C. J. Fennie, D. G. Schlom, K. M. Shen, *Phys. Rev. Lett.* **114**, 016401 (2015).
16. D. G. Schlom, *APL Mater.* **3**, 062403 (2015).
17. A. Ohtomo, H. Y. Hwang, *Nature* **427**, 423 (2004).
18. R. Ramesh, N. A. Spaldin, *Nat. Mater.* **6**, 21 (2007).

19. B. W. Li, M. Osada, Y-H Kim, Y. Ebina, K. Akatsuka, T. Sasaki, *J. Am. Chem. Soc.* **139**, 10868 (2017).
20. Y. Ebina, T. Sasaki, M. Watanabe, *Solid State Ionics* **151**, 177 (2002).
21. M. Osada, T. Sasaki, *J. Mater. Chem*. **19**, 2503 (2009).
22. Y. Ebina, K. Akatsuka, K. Fukuda, T. Sasaki, *Chem. Mater.* **24**, 4201 (2012).
23. É. D. Murray, D. Vanderbilt, *Phys. Rev. B* **79**, 100102 (2009).
24. Y. Sun, H. Cheng, S. Gao, Z. Sun, Q. Liu, Q. Liu, F. Lei, T. Yao, J. He, S. Wei, Y. Xie, *Angew. Chem.* **124**, 8857 (2012).

Chapter 6

Major Conclusion and Outlook

6.1. Major Conclusions

This thesis addresses the LbL assembly of 2D perovskite nanosheets. The focus is on DJ-type homologous series of perovskite nanosheets ($Ca_2Na_{m-3}Nb_mO_{3m+1}^-$; m = 3-6). Homologous series of perovskite nanosheets that possess molecular thickness (~ 1.4 – 3 nm) are 2D single crystals, were exfoliated from their bulk-layered material through soft-chemical exfoliation process. Facile LbL method based on LB technique is an effective way for the fabrication of nanostructures with molecular control that possess potential application as electronic material. The summary of the work is given below:

1. I set new direction for the design of microwave dielectrics by utilizing ultrathin perovskite nanosheets, $Ca_2Nb_3O_{10}^-$, films as potential material. To this end, LbL assembly is a power tool to engineer dielectric response and breakdown voltages in ultrathin perovskite nanosheets films (< 30 nm). Multilayer-stacked $Ca_2Nb_3O_{10}^-$, films exhibited robust high-k response (ε_r = 200) up to 10 GHz. I observed an enhanced breakdown voltage in 20-layered perovskite films due to barrier effect. Here, the barrier effect was provided by larger number of dielectric layers and interfaces. Ultrathin multilayer nanosheets films exhibited high capacitance density of ~20 μF/cm^2 which was stable up to 250 ^{o}C. These characteristics of perovskite nanosheets films justify their applications for high performance microwave devices.

2. I fabricated multilayer nanosheets capacitors (MNCs) by utilizing newly developed high-k ($Ca_2NaNb_4O_{13}^-$; ε_r = 300) perovskite nanosheets. LbL assembly of dielectric $Ca_2NaNb_4O_{13}^-$ and metallic $Ru_{0.95}O_2^{0.2-}$ nanosheets provides control at nanoscale level for the fabrication of ultrathin MNCs. LB method was employed for the alternate deposition of metallic and dielectric nanosheets. Cross-sectional HRTEM results confirmed the successful fabrication of MNCs in which dielectric layers were dense and gap free, interspersed between $Ru_{0.95}O_2^{0.2-}$ electrodes in smooth, nearly perfect LbL fashion. Millimeter-size, ultrathin MNCs (~ 20 nm) established high capacitance density of 52 μF/cm^2 and low leakage current down

to 10^{-6} A/cm^2 at +1V. In this study, I investigated the effect of different number of $Ca_2NaNb_4O_{13}^-$ and $Ru_{0.95}O_2^{0.2-}$ layers on the dielectric response and leakage current density. I concluded that MNCs with 2-layered $Ca_2NaNb_4O_{13}^-$ nanosheets films and two-layered $Ru_{0.95}O_2^{0.2-}$ nanosheets layers exhibited excellent dielectric properties and reduced leakage current density.

3. Perovskite nanosheet, $Ca_2Nb_3O_{10}^-$, is unique class of materials that demonstrate high-*k* properties of $\varepsilon_r > 210$ even in ultrathin region (< 10 nm). In this work, I investigated the high temperature dielectric properties of nanosheets-based capacitors. Ultrathin nanosheets-based capacitors are fabricated in the form of metal-insulator-metal structures. Alternate assembly of dielectric $Ca_2Nb_3O_{10}^-$ and $Ru_{0.95}O_2^{0.2-}$ nanosheets was realized through LB and sequential adsorption procedures. Such nanosheets-based capacitor exhibited high-*k* properties (> 155) and insulating response (< 1 x 10^{-5} A/cm^2) at elevated temperature up to 200 ^{o}C. I also investigated the capacitance response of $Ca_2NaNb_4O_{13}^-$ based nanosheets capacitor fabricated in Chapter 3 as a function of both high temperature and voltage. MNCs realized stable capacitance response over a wide temperature range of -50 ~ 250 ^{o}C with small capacitance deviation of -5.5%.

4. Here I present a new strategy for the LbL assembly of homologous members of perovskites nanosheets to engineer dielectric/ferroelectric responses at the molecular level. DJ-type homologous series of perovskite nanosheets ($Ca_2Na_{m-3}Nb_mO_{3m+1}^-$; m = 3-6) has been studied because of their unique high-*k* properties. Due to higher polarizability in larger m perovskite nanosheets, the superlattice films realized enhanced dielectric response with rise of novel ferroelectric property. Homologous members demonstrate variable thickness along the block normal due to presence of different number of NbO_6 octahedron units (i.e. integer m) and have virtually infinite perovskite blocks in the 2D planes. Through cross-sectional HRTEM, I observed highly organized superlattice films in which constituent nanosheets layers were assembled in a lamellar structure thanks to solution-based LbL assembly process for providing molecular control on assembly process. Such artificial superlattice exhibited high-*k* properties of ~427 even at

ultrathin thickness (< 30 nm) and reduced leakage current density of < 10^{-9} A/cm^2 along with the development of novel ferroelectric property.

This thesis set a new direction for the LbL assembly of perovskite nanosheets to realize nanostructures that possess potential application for electronic materials such as multilayered perovskite films as new microwave dielectrics, multilayer nanosheets capacitors (MNCs) for high-density capacitor, nanosheets-based multilayer films for high-temperature applications, and last but not least artificial superlattice films of perovskite nanosheets to realize novel ferroelectric properties with enhanced high-*k* response. All of these characteristics have been realized at ultrathin thickness (< 30 nm) that is not possible to observe in current perovskite materials.

6.2. Outlook for Future Work

Several prospective studies related with this work are given below;

1. ***Layer-by-layer engineering of perovskite nanosheets***

In this work, I demonstrated new set for high-*k* perovskite nanosheets as microwave dielectrics. Multilayered films of $Ca_2Nb_3O_{10}^-$ realized high-*k* dielectric response (> 200) up to 10 GHz. 20-layered $Ca_2Nb_3O_{10}^-$ films exhibited enhanced breakdown voltage of ~ 6MV/cm due to barrier effect. A prospective study of this work may utilize high-*k* perovskite nanosheets such as $Ca_2NaNb_4O_{13}^-$ ε_r = 300. As $Ca_2NaNb_4O_{13}^-$ demonstrate large lateral size > 10 μm, which can result in decrease leakage paths in contrast to $Ca_2Nb_3O_{10}^-$ nanosheets-based films. As a result, multilayer films of $Ca_2NaNb_4O_{13}^-$ nanosheets can demonstrate superior high-*k* response and even higher breakdown voltages at ultrathin thickness (< 30 nm).

2. ***Solution-based assembly of ultrathin 2D nanosheets capacitors***

In this study, I have realized multilayer nanosheets capacitors (MNCs) by utilizing newly developed high-k nanosheets ($Ca_2NaNb_4O_{13}^-$; ε_r = 300). Though solution based LbL assembly it has been possible to fabricate ultrathin MNCs with thickness of ~ 20 nm that realized excellent capacitance density of 52 μF/cm^2 and

low leakage current down to 10^{-6} A/cm^2 at +1V. As dielectric constant in homologous members of perovskite nanosheets increase with larger number of NbO_6 octahedra along the thickness. A prospective study for this work can utilize higher *m* = 5, 6 perovskite nanosheets as dielectric layers to observe enhanced capacitance in the multilayer nanosheets capacitors.

3. ***High-temperature dielectric responses of ultrathin nanosheets***

In this work, I studied the high-temperature dielectric response in $Ca_2Nb_3O_{10}^-$ and $Ca_2NaNb_4O_{13}^-$ based nanosheets capacitors. Metallic $Ru_{0.95}O_2^{0.2-}$ and dielectric $Ca_2Nb_3O_{10}^-$ nanosheets have been deposited at alternate fashion via LB technique and sequential adsorption procedure. The resulting nanosheets-based capacitors exhibited high-*k* properties (> 155) and insulating response (< 1x 10^{-5}A/cm^2). The slight decrease in dielectric constant and enhanced leakage can be overcome by decreasing the surface roughness of $Ru_{0.95}O_2^{0.2-}$ electrode. A prospective work of this study can utilize the assembly of $Ru_{0.95}O_2^{0.2-}$ nanosheets electrode through LB technique to realized atomically uniform electrode layers that will allow the deposition of densely packed $Ca_2Nb_3O_{10}^-$ nanosheets layers as dielectric films and will result in enhanced dielectric constant and reduced leakage current density.

4. ***Superlattice assembly of 2D perovskites for tailored ferroelectri***c

In this work, I utilize homologous members of perovskites nanosheets ($Ca_2Na_{m-3}Nb_mO_{3m+1}^-$; *m* = 3-6) to engineer dielectric/ferroelectric properties of superlattice films at nanoscale. The artificial superlattices realized high-*k* properties of ~427 even at ultrathin thickness (< 30 nm) and reduced leakage current density of < 10^{-9} A/cm^2 along with the development of novel ferroelectric property. This strategy offers new direction for the fabrication of novel superlattices utilizing different oxides nanosheets to realize novel properties. As oxides nanosheets are rich in structural and electronic diversity, superlattice assembly of different oxides nanosheets can be accomplished through solution-based LbL method to engineer the novel properties at interface.

List of Publications

1. Article

1. M. S. Khan, H-J. Kim, T. Taniguchi, Y. Ebina, T. Sasaki, and M. Osada: "Layer-by-Layer Engineering of Two-Dimensional Perovskite Nanosheets for Tailored Microwave Dielectrics", *Appl. Phys. Exp.*, Vol. 10, 091501 (2017).

2. M. S. Khan, M. Osada, H-J. Kim, Y. Ebina, W. Sugimoto, and T. Sasaki: "High-Temperature Dielectric Responses in All-nanosheet Capacitors", *Jpn. J. Appl. Phys.,* Vol. 56, 06GH09 (2017).

3. M. S. Khan, M. Osada, H-J. Kim, Y. Ebina, W. Sugimoto, and T. Sasaki: "Scalable Solution Assembly of 2D Nanosheets for High-Performance Multilayer Capacitors", *Adv. Mater*. (under review).

4. M. S. Khan, M. Osada, L. Dong, Y-H. Kim, X. Liu, Y. Ebina, and T. Sasaki: "Atomically Precise Interfaces of 2D Perovskites for Tailored Ferroelectrics", *Adv. Funct. Mater*. (submitted).

2. Conferences

1. M. S. Khan, M. Osada, Y. Ebina, W. Sugimoto, and T. Sasaki: "High-Temperature Dielectric Responses in Nanosheet-Based Capacitors", IMAPS/ACerS 13th International Conference and Exhibition on Ceramic Interconnect and Ceramic Microsystems Technologies, April 19-21, 2017, Nara, Japan.

2. M. S. Khan M. Osada, Y. Ebina, and T. Sasaki: “Tuning Interlayer Coupling in Nanosheet Architectures for Artificial Multiferroics”, MANA International Symposium 2017, Nano Revolution for the Future, February 28 - March 03, 2017, Tsukuba, Japan.

3. M. S. Khan, M. Osada, Y. Ebina, and T. Sasaki: “Highly Organized Layer-by-Layer Assembly of Perovskite Ferroelectric Superlattices”, 29th International Microprocesses and Nanotechnology Conference (MNC 2016), November 8 - 11, 2016, Kyoto, Japan.

4. M. S. Khan, M. Osada, Y. Ebina, and T. Sasaki: “Engineering of Dielectric and Ferroelectric responses in 2D perovskites”, 29th International Microprocesses and Nanotechnology Conference (MNC 2016), November 8 - 11, 2016, Kyoto, Japan.

5. M. S. Khan, M. Osada, Y. Ebina, and T. Sasaki: “Artificial Design for Perovskite Ferroelectrics using Nanosheet Architectonics", MANA International Symposium 2016, Nano Revolution for the Future, March 9-11, 2016, Tsukuba, Japan.

6. M. S. Khan, M. Osada, Y. Ebina, and T. Sasaki: “Artificial Design for Perovskite Ferroelectrics using Nanosheet Architectonics", 25th Annual Meeting of MRS-J, December 8-10, 2015, Yokohama, Japan.

7. M. S. Khan, M. Osada, Y. Ebina, and T. Sasaki: “Artificial Design for Perovskite Ferroelectrics using Nanosheet Architectonics", 6th NIMS/MANA-Waseda University International Symposium, July 29, 2015, Waseda University, Tokyo, Japan.

Acknowledgements

I would like to express my special appreciation and thanks to my supervisor, Prof. Minoru Osada, for taking me into his research group and constantly supporting me throughout my PhD study. He has been a tremendous mentor for me and I am extremely grateful for his guidance, advices, and encouragement during my PhD study. I highly appreciate his utmost knowledge and great vision for research. I learned many skills from him such as preparation of conference talks and writing articles. I am deeply thankful for his guidance during the course of my thesis writing. I am highly thankful to him for his support on each aspect during my PhD.

I would like to sincerely thank my committee members, Prof. Yoshiyuki Sugahara, Prof. Kiyoshi Shimamura, Prof. Tohru Suzuki for serving as my committee members. I also want to thank you for letting my defense as a learning moment with your brilliant comments and suggestions, thanks to you.

I would like to specially thank to Prof. Toyohiro Chikyow for his valuable guidance at the start of my PhD and his valuable and thought provoking questions and comments during student seminars.

I would like to express my deep thank to Prof. Takayoshi Sasaki for providing me opportunity to be the part of his collaborative team. I am highly thankful for his valuable questions and comments at weekly meetings in beginning of my PhD. I am also highly indebted to him for his permission to access his laboratory facilities.

I would like to thank Dr. Yasuo Ebina for providing high quality nanosheets suspensions, which set a base for preparation of high quality samples.

I would like to thank Dr. Takaaki Taniguchi, Dr. Renzhi Ma, Dr. Hyung-Jun Kim, Dr. Yoon-Hyun Kim, Dr. Cai Xingke, Dr. Wei Ma and Dr. Shisheng Li for their kind and continuous support in my research work.

I would like to thank Ms. Tomoko Tsuda, Ms. Yokota Eiko, and Ms. Yoshie Ohashi for their support on official matters.

I would like to thank Ms. Yeji Song, Mr. Leanddas Nurdiwijayanto, Mr. Kei Kamanaka, Mr. Tatsumasa Hoshide for teaching me experimental skills.

I would like to thank Ms. Yumiko Sawabe and staff at Nimiki fondary for teaching me experimental skills.

Last but not least, special thanks go to my parents, wife and siblings for almost unbelievable support. Words cannot express how grateful I am for their prayers for me that sustained me thus far. They are the most important people in my life and I dedicate this thesis to them.